QUANTITATIVE FTIR IMAGING FOR CONTACT DYNAMICS ANALYSIS

A Dissertation

Presented to

The Graduate Faculty of The University of Akron

In Partial Fulfillment

of the Requirements for the Degree of

Doctor of Philosophy

MENGYUE SUN

December 2022

QUANTITATIVE FTIR IMAGING FOR CONTACT DYNAMICS ANALYSIS

MENGYUE SUN

Dissertation

Approved:

_____
Advisor
Dr. Hunter King

_____
Committee Member
Dr. Ali Dhinojwala

_____
Committee Member
Dr. Mesfin Tsige

_____
Committee Member
Dr. Chunming Liu

_____
Committee Member
Dr. Kwek-Tze Tan

Accepted:

_____
Interim Director of SPSPE
Dr. Mark Soucek

_____
Dean of the College
Dr. Craig Menzemer

_____
Dean of the Graduate School
Dr. Suzanne Bausch

_____
Date

ABSTRACT

When a beam of light goes from a denser medium to a less dense medium, illuminates the interface of two mediums at an incident angle greater than the critical angle $\theta_C = \sin^{-1}\left(\frac{n_2}{n_1}\right)$, light is totally internally reflected to the denser medium. At this moment, an evanescent field is formed, and it propagates along the surface of the denser medium, attenuating exponentially away from the surface. When a 3rd dense medium is brought into the vicinity, a portion of light passes into it, attenuating the reflected intensity. This phenomenon, called frustrated total internal reflection (FTIR), has been utilized in visualizing contact dynamics. It also provides a means to understand adhesion and friction between surfaces because they are known to depend sensitively on actual contact area as well as magnitude and spatial distribution of gaps of near contact down to the nanoscale. However, quantitative conversion of the reflected signal to gap thickness has only recently been achieved by proper analysis of the Fresnel equation with consideration of multiple reflections, transmissions, and polarization of light.

This thesis presents a study of applications of frustrated total internal reflection (FTIR). First, we present a quantitative optical method to characterize dynamics of contact formation between two mediums based on theory of FTIR. The method is first validated by measuring height profile of convex lens in contact with flat prism surface and comparing with Hertzian theory. The method is then used to track the evolution of

contact between a soft hemisphere brought into contact with a hard surface under water, as function of hemisphere stiffness, and surface wettability. We find an exponential rate of water evacuation from hydrophobic–hydrophobic (adhesive) surfaces that is 3 orders of magnitude smaller than that from hydrophobic–hydrophilic (non-adhesive) contact. This counterintuitive result comes from adhesive surfaces to more tightly sealing puddles of trapped water. Similar observation for a human thumb touching alternatively hydrophobic/hydrophilic glass surfaces, demonstrates generality of the mechanism and points to practical consequences.

Second, we investigate the potential of FTIR to measure the thicknesses and deformations of thin Polydimethylsiloxane (PDMS) films. With tunable elastic modulus, deformations of thin films can be converted into pressure values, thus FTIR can be utilized as sensitive pressure sensor to measure bio-adhesion such as pressure distribution under gecko feet and mussel feet.

ACKNOWLEDGEMENT

There are too many people to thank during my Ph.D. study in the past few years.

I would like to express my sincere appreciation to my committee members: Dr. Ali Dhinojwala, Dr. K.T. Tan, Dr. Mesfin Tsige and Dr. Chunming Liu for attending my defense and sharing their valuable insights.

Input from Dr. Nityanshu Kumar and Dr. Ali Dhinojwala has given much form and direction to the main project in this thesis. Without their theoretical support, this work would be trivia. I should give special thanks to Dr. Nityanshu Kumar, I have received crucial help with experimental and theoretical techniques from him.

Most importantly, I want to share my sincere gratitude to Dr. Hunter King, for his patience, motivation, encouragement, and tremendous knowledge. His valuable suggestions and guidance helped me throughout the research and study. Best wishes to his new career at Rutgers University.

In a broader sense, I thank my father and my mother for their support. Special thanks to my wife Dr. Yiheng Pan for giving me confidence and tolerance.

TABLE OF CONTENTS

Page

LIST OF FIGURES ix

LIST OF TABLES xii

CHAPTER

I. INTRODUCTION 1

II. INTRODUCTION OF TOTAL INTERNAL REFLECTION 2

2.1 Polarization of light 2

2.2 Reflection and refraction of light 5

2.3 Total internal reflection and evanescent wave 7

2.4 Frustrated total internal reflection 10

III. INTRODUCTION OF CONTACT MECHANICS 13

3.1 Definition of interfaces 13

3.2 Surface energy and surface tension 14

3.3 Contact angle and surface wettability 16

3.4 Dynamic contact angle 22

3.5 Hertzian contact theory 27

3.6 Johnson-Kendall-Roberts (JKR) contact theory 32

3.7 Derjaguin-Muller-Toporove (DMT) model 34

IV. QUANTITATIVE FRUSTRATED TOTAL INTERNAL REFLECTION (FTIR) FOR THIN FILM CHARACTERIZATION 36

4.1 Introduction 37

4.2 Theoretical design of ftir 43

4.3 Experimental setup and data acquisition 47

4.4 Setup calibration with hertzian contact 52

4.5 Polymer thin film measurement 56

V. ATTRACTIVE FORCES SLOW CONTACT FORMATION BETWEEN DEFORMABLE DOIDES UNDERWATER 63

5.1 Materials and methods 66

5.1.1 Synthesis of smooth elastic polydimethsiloxnae lenses 66

5.1.2 Fabrication of varing wettability glass prism 68

5.1.3 JKR contact experiment 69

5.1.4 FTIR setup and experiment 71

5.2 Principles of experiment 73

5.3 Dynamics of water evacuation 78

5.4 Effect of pdms moduli and substrate wettability on rate constant 80

5.5 Initial contact formation and modes of evacuation 82

5.6 Human thumb contacts 87

5.7 Transition in evacuation dynamics 91

5.8 Contact formation and subsequent evacuation 93

5.9 Water puddle breaks down before contact 95

5.10 How is water escaping from sealed adhesive entrapment 96

5.11 Conclusion 97

VI. CONCLUSION AND FUTURE WORK 100

6.1 Issues with camera sensor 103

6.2 Effect of background light 103

6.3 Effect of polarization change 104

6.4 Effect of surface contamination and roughness.....104
6.5 Conclusion.....105
REFERENCES 106

LIST OF FIGURES

Figure Page

2-1 Electromagnetic wave of wavelength λ.. 2

2-2 Circular polarization of light.. 4

2-3 Unpolarized light passing through polarizer become polarized light. 4

2-4 Reflection and refraction of incident ray with polarization. 5

2-5 Refractive angle increases with increasing of incident angle. 7

2-6 Intensities of refractive ray at both polarizations sharply reach to zero as critical angle is reached. 8

2-7 Total internal reflection happens at glass – water interface with evanescent wave shown on the right image [16]. 10

2-8 Frustrated total internal reflection happens when third medium with higher refractive index is brought extremely close the interface. 11

3-1 Liquid molecules in "happy" and "unhappy" states. 15

3-2 Schematic of a liquid drop sitting on solid surface, showing the quantities in Young's equation 17

3-3 Contact angles: non-wetting, partially wetting, perfect wetting.. 19

3-4 Zisman plot for both homologous and non-homologous liquid. 20

3-5 Advancing and receding contact angle measurement. Image from Weistron Co. 22

3-6 Wenzel model of droplet sits on rough surface, the droplet completely wet grooves of surface.. 24

3-7 Cassie-Baxter model of droplet sits on rough surface with air pockets entrapped in grooves. 26

3-8 Wetting transition from Cassie-Baxter state to Wenzel state. 27

3-9 Wetting transition from Cassie-Baxter to Wenzel state. Beginning from the edge of droplet to center of droplet [47]. 27

3-10 Hertzian contact for two spheres contact with each other. 28

3-11 Hertzian contact for a sphere contact with elastic half-space. 30

3-12 Hertzian contact. 31

3-13 JKR contact model with effect of adhesion accounted 33

4-1 (1) Contact formation between finger and hard, smooth surface. (2) contact formation between finger and soft rubbery surface [50]. 38

4-2 (a) FTIR setup. (b)Total internal reflection is achieved by placing LEDs under the corner. (c)-(f) Images obtained via cameras [51]. 39

4-3 FTIR setup with tactile sensing array for stress distribution and contact area measurement [51]. 40

4-4 FTIR Setup composed of laser, fast camera, and prism. 41

4-5 (a) FTIR image of droplet impact on glass surface. (b) and (c) distance analysis of each frame [53]. 43

4-6 Three mediums system to show geometry at interface with multiple refraction and reflection [53]. 46

4-7 Stokes relations. If there is no absorption, (1) and (2) should be reversible. 46

4-8 At fixed system, Kolinski's method is underestimating gap thickness [53]. 47

4-9 Experimental setup. A circular shape water droplet is placed on prism surface to determine the incident angle. 48

4-10 Distorted image of water drop in contact with prism surface. 49

4-11 Ellipse fit for Eq.4.9. 50

4-12 Aspect ratio vs incident angle, the table could be directly used to match incident angle with known aspect ratio. 51

4-13 Look-up table for given system of glass-air-water at $\theta i = 45°$. 51

4-14 Convex lens is placed on prism surface to be used for calibration. 52

4-15 Look-up table for given system of glass-air-glass at $\theta i = 45°$. 53

4-16 Raw data processing for convex lens contact with prism surface. 54

4-17 Height profile of convex lens LA1608 with 20 grams of applied load, the measured height matched with Hertzian theory very well. 55

4-18 Elastic deformations of convex lens with external applied loads. 56

4-19 Look up table for glass-PDMS-Cinnamaldehyde system at incident angle $\theta i = 75°$ 58

4-20 Experiment system of glass-PDMS-Cinnamaldehyde and their structures. 59

4-21 Thickness of PDMS film measured by FTIR. (1) Surface topography of thin PDMS film. (2) Thickness of PDMS verse time. 60

5-1: Schematic of experimental setup for in-situ force and contact area measurements.. 69

5-2 Schematic Contact radius of PDMS lens with OTS substrate,. 70

5-3 Schematic (not to scale) of (A) the frustrated total internal reflection imaging setup 74

5-4 Normalized reflectance as a function of gap thickness.° 77

5-5 Measured air film thickness for a glass lens/glass prism (hollow red square). 78

5-6 Effect of material moduli and chemistry. 79

5-7 Log(K) versus cosine of substrate water contact angle for three moduli of PDMS lens showing similar transition at $Cos^{-1}(0.78)$ ($\theta \approx 38°$). 81

5-8 Effect of velocity on water entrapment. 81

5-9 Spatiotemporal height maps and corresponding gray-scale images 83

5-10 2D line heightmaps along x and y direction for PDMS/glass 85

5-11 Spatiotemporal height maps and corresponding gray-scale images. 88

5-12 Spatiotemporal height maps for water in a localized region (marked by black solid box) for a human thumb in contact with glass (top panel) and. 90

6-1 Look up table changes with changing of second medium. 103

6-2 Offset change verse refractive indices. Offset increases increase with increasing of refractive index. 105

LIST OF TABLES

Table Page

2-1 Surface tensions of few common liquids. 16

4-1 Elastomer modulus (G) and work of adhesion numbers calculated 71

CHAPTER I

INTRODUCTION

Polymers have been widely used and researched, from our daily basis such as tires [21], coatings [22-32] and glues [33] to advanced biomimicry technologies in fields of haptics, soft robotics [34] and bio-adhesion due to their characteristic properties such as accessibility, and low cost.

To better explore applications of polymers in these fields, it is crucial to understand the contact mechanics involve surfaces and interfaces between polymers and substrates, as contact mechanics is directly related to interfacial properties, such as wetting [35], adhesion [36-38], and especially frictions [39].

Surfaces and interfaces in contact mechanisms can be studied quantitatively via their surface energy/tension. Surface energy and interfacial interactions could lead to adhesion phenomena including electrostatic forces, the van der Waals force, and hydrophobic interactions in underwater conditions. However, the adhesion is sensitively dependent on the distance between two surfaces, as it diminishes dramatically during separation of two surfaces. Knowing where is in actual contact, where is in near contact region down to nanoscale, and where is in far contact between surfaces is essential for us to explore applications of polymers.

Furthermore, when two surfaces are brought in contact underwater, the underwater contact mechanics could be more complicated. Because some water could get entrapped in the interface which may lead to huge differences in adhesion behaviors than that of dry contact. It's necessary for us to understand the adhesion behaviors in wet conditions, as in practically speaking, the applications of polymers in coatings, tires, and haptics may confront different conditions than the ideal dry case. Understanding wet contact mechanics between surfaces also help reveal nature mysteries such as how could tree frog stick to flooded surfaces? As water entrapment could reduce the real contact area between two surfaces thus eliminating the adhesion and friction significantly. How does tree frog avoid this issue or how does it squeeze the water out? The answer becomes extremely important and could contribute to applications of wet tire traction, polymer coatings like sealing and high-end biotechnology such as bio-tissues adhesion.

As surface interactions are sensitively dependent on the distance between two surfaces in nanoscale, thus an accurate measurement of gap thickness is required. In recent years, frustrated total internal reflection (FTIR) has been widely used to study the contact dynamics of two objects, due to its distinct advantages of measuring nanoscopic films accurately and visualizing interfaces directly. However, in many cases which assume the simple exponential decay function of FTIR without considering multiple reflections and transmissions are underestimating the gap thickness.

This thesis presents a study of applications of frustrated total internal reflection (FTIR). First, we present a quantitative optical method to characterize dynamics of contact formation between two mediums based on theory of FTIR. The method is first validated by measuring height profile of convex lens in contact with flat prism surface

and comparing with Hertzian theory. The method is then used to track the evolution of contact between a soft hemisphere brought into contact with a hard surface under water, as function of hemisphere stiffness, and surface wettability. We find an exponential rate of water evacuation from hydrophobic–hydrophobic (adhesive) surfaces that is 3 orders of magnitude smaller than that from hydrophobic–hydrophilic (non-adhesive) contact. This counterintuitive result comes from adhesive surfaces to more tightly sealing puddles of trapped water. Similar observation for a human thumb touching alternatively hydrophobic/hydrophilic glass surfaces, demonstrates generality of the mechanism and points to practical consequences.

In chapter 2, I provided fundamental knowledge of theory of polarization dependent frustrated total internal reflection that counts multiple reflections and transmissions.

In chapter 3, I provided essential information to help understand contact mechanics, such as quantitative studies of surface energy and surface tension. Further, classic Hertz contact theory without considering effect of adhesion has been introduced to be compared with JKR and DMT contact theory which considered effect of adhesion. Moreover, surface wettability has also been discussed to help understand the underwater contact mechanics.

In chapter 4, a detailed frustrated total internal reflection apparatus and step by step data acquisition showed and explained. Calibration of this apparatus was performed by measuring gap thickness/height profile of convex glass lens in contact with glass prism and compared with Hertz contact theory of elastic sphere in contact with half-space

and obtained excellent agreement. Further application of FTIR to measure thin polymer films has also been evaluated in this chapter.

In chapter 5, I have discussed the synthesis and characterization of soft elastomeric PDMS lenses and sheets and showed a schematic for the JKR setup to be used for adhesion measurement between PDMS lens and substrates. Furthermore, I studied the underwater contact formation and evolution between soft/hard surfaces of varying wettability via FTIR. The experiments of thumb in contact with hard smooth surfaces have also been performed to reveal underwater contact mechanisms of nature cases, patterns and textures on the surfaces can help evacuate water out but can't prevent happening of adhesive sealing.

In chapter 6, I have discussed limitations of FTIR, and investigated the rise of unknown offset in distance measurements that reported by other researchers. Possible causes of offset such as background light, camera sensor issue, surface contaminations and scattering has been evaluated.

In conclusion, FTIR is a robust tool that can help researchers to directly measure and visualize the interface between two contact objects. The works presented in this thesis could help researchers in contact mechanics, adhesion, underwater adhesion fields.

CHAPTER II

INTRODUCTION OF TOTAL INTERNAL REFLECTION

Light is electromagnetic wave consists of coupled oscillating magnetic and electric fields which are always perpendicular to each other [1].

2.1 POLARIZATION OF LIGHT

In classical physics, light can be thought of as a wave of electric and magnetic fields that perpendicular to each other, and perpendicular to the direction of propagation of waves, as shown in Figure 2-1.

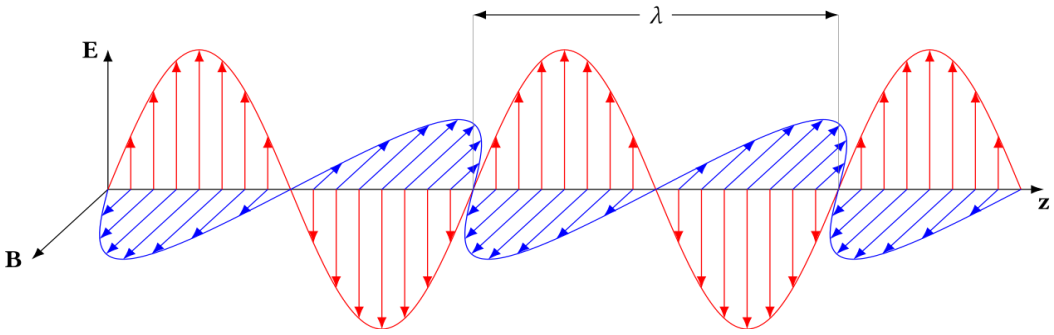

Figure 2-1: Electromagnetic wave of wavelength λ. Electric field vector E (red), and magnetic field B (blue). Both waves are perpendicular to the direction of propagation.

Polarization of light, in Physics, is defined as a phenomenon applying to electromagnetic waves that represent the geometrical orientation of the oscillations [2-6]. By convention, the polarization of electromagnetic waves refers to the direction of electric field.

If a light wave is composed of electromagnetic waves that are oriented in all different directions is called unpolarized light, for instances, sunlight or light emitted by a lamp.

On the other hand, if a light wave consists of electromagnetic waves that are all aligned in the same direction, or by same means, the electric field of light is only vibrating in single plane along the direction of propagation, then the light is called linear polarization.

If the electric wave of light has a constant amplitude and is orienting at a constant rate in a plane perpendicular to the direction of propagation, or by same means, the electric field can be split into two electric field have equal amplitude that are perpendicular to each other, but the phase difference is $\pi/2$, then this light is circularly polarized as shown in Figure 2-2. If amplitude is not equal or phase difference is not $\pi/2$, then light is elliptically polarized. Both circular and linear polarization are special cases of elliptical polarization.

The polarization of light can be simply adjusted by applying a polarizer in front of the light source, as shown in Figure 2-3.

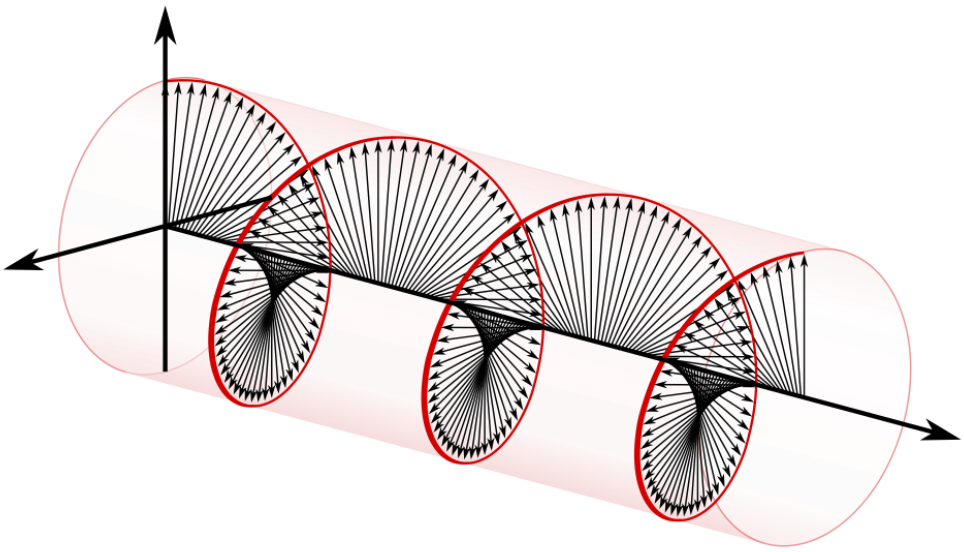

Figure 2-2 Circular polarization of light. Image from Wikipedia.

If only a specific polarization of light waves that contains mixed polarization can pass through an optical filter while all other polarizations of light waves are blocked off, then this filter is called polarizer [7-10]. The filtered light beam with well-defined polarization is called polarized light.

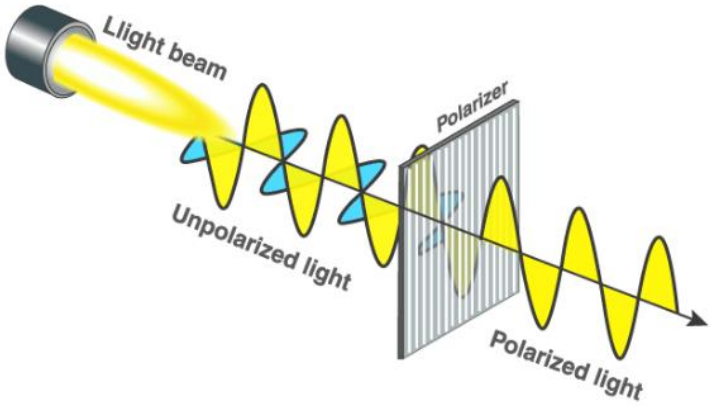

Figure 2-3 Unpolarized light passing through polarizer become polarized light.

2.2 REFLECTION AND REFRACTION OF LIGHT

When a light wave travels from one medium with given refractive index (n_1) into a medium with different refractive index (n_2), at this moment, reflection and refraction will happen. In the most general case, at the interface of two mediums, a certain portion of the light is reflected to the first medium and remained portion of light is refraction into the second medium.

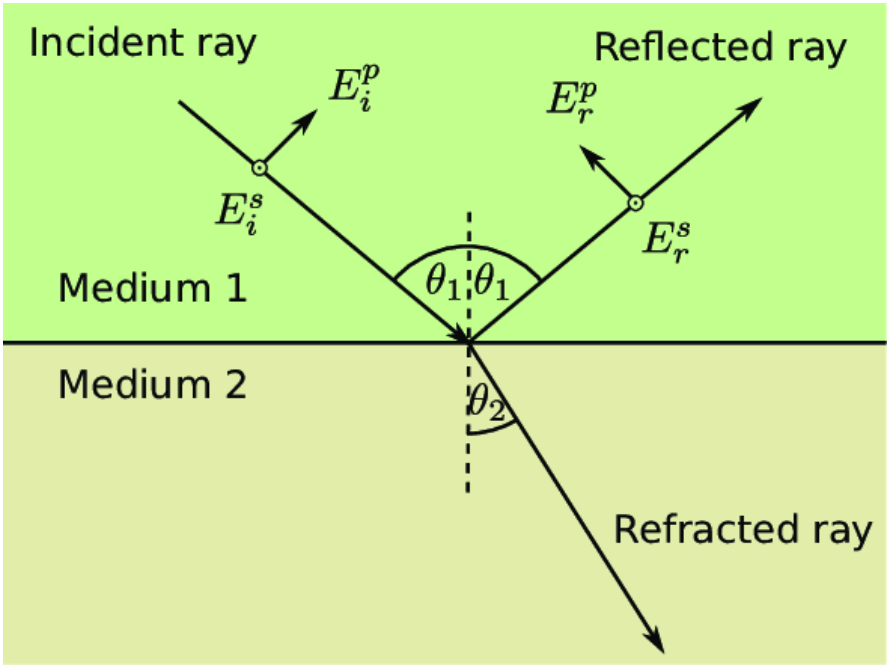

Figure 2-4 Reflection and refraction of incident ray with polarization.

The reflective angle $\theta_1$and refractive angle θ_2 should follow Snell's law as shown below:

$$\frac{sin\,\theta_1}{sin\,\theta_2} = \frac{n_2}{n_1} \qquad (2.1)$$

In this equation, if n_2 is greater than n_1, then second medium is denser than the first medium, otherwise n_1 is the denser medium.

Snell's equation also demonstrated that refractive angle $\theta_2$increases with increasing of incident angle θ_1.

Solving Maxwell's equation for light wave hitting interface between two mediums allows the derivation of the Fresnel equations for S-Polarization and P-Polarization respectively shown below, which describes how much of the light reflected to the first medium and how much of the light refracted into the second medium.

$$t_P = \frac{2n_1 \cos\theta_i}{n_2 \cos\theta_i + n_1 \cos\theta_t} \quad (2.2)$$

$$t_S = \frac{2n_1 \cos\theta_i}{n_1 \cos\theta_i + n_2 \cos\theta_t} \quad (2.3)$$

$$r_P = \frac{n_2 \cos\theta_i - n_1 \cos\theta_t}{n_2 \cos\theta_i + n_1 \cos\theta_t} \quad (2.4)$$

$$r_s = \frac{n_1 \cos\theta_i - n_2 \cos\theta_t}{n_1 \cos\theta_i + n_2 \cos\theta_t} \quad (2.5)$$

Fresnel equation demonstrates that refractive ray has same phase as incident ray while the phase difference between reflective ray and incident ray is dependent on incident angle θ_i and refractive angle θ_t. In case of $n_2 > n_1$, if $\theta_t < \theta_i$, then the phase difference is π.

2.3 TOTAL INTERNAL REFLECTION AND EVANESCENT WAVE

From Snell's law we can see that refractive angle θ_t increase with increasing of incident angle θ_i, as shown in Figure 2-5. Till refractive angle θ_t reaches to 90°. At this point the corresponding angle of incident is called critical angle can be written as:

$$sin\,\theta_C = \frac{n_2}{n_1} \qquad (2.6)$$

As incident angle increases, the refractive angle is also increasing but the intensity of refracted ray is becoming dimmer while intensity of reflected ray is getting brighter, till at incident angle exceeds critical angle, the angle of refracted ray approaches 90° all incident rays will be reflected. This is called total internal reflection that can only happen when the first medium is denser than the second medium ($n_1 > n_2$). As shown in Figure 2-7, the intensity of refracted ray sharply goes to zero as the critical angle is approached, which means that all energy from the incident ray is reflected.

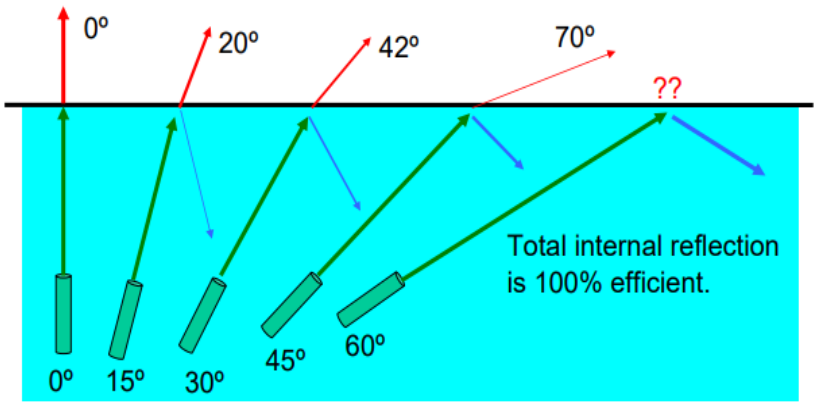

Figure 2-5 Refractive angle increases with increasing of incident angle.

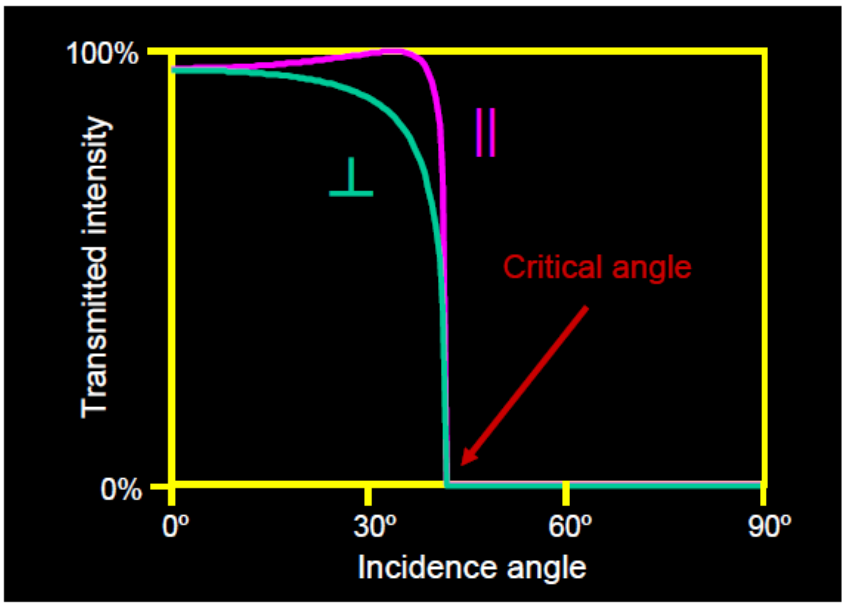

Figure 2-6 Intensities of refractive ray at both polarizations sharply reach to zero as critical angle is reached.

Even all power from incident ray is carried by reflected ray when incident angle is greater than critical angle. The transmitted (refractive) wave in the second medium is still existing but it just does not carry any power in this case. Under the total internal reflection condition, the transmitted wave is called evanescent wave that can be characterized mathematically.

Let's first assume for the plane of incidence as the xy plane at z=0, the plane of interface of the two mediums as the xz plane at y=0, then the vector of the refracted (transmitted) wave can be written as below [12]:

$$K_t = k_y\hat{y} + k_x\hat{x} \qquad (2.7)$$

Where $k_x = k_t \sin\theta_t$ and $k_y = k_t \cos\theta_t$ where k_t is the wavenumber of the transmitted wave vector, $\hat{x}$ and $\hat{y}$ are unit vector along x axis direction and y axis direction respectively.

From the Snell's law $\frac{\sin\theta_i}{\sin\theta_t} = \frac{n_t}{n_i}$, we know that $\sin\theta_t = \sin\theta_i \frac{n_i}{n_t}$ then

$$k_y = k_t \sqrt{1 - \frac{Sin^2\theta_i n_i^2}{n_t^2}} \qquad (2.8)$$

In case of total internal reflection, $n_i > n_t$, k_y is a pure imaginary quantity, let's call it $j\beta$. We know that transmitted wave can be described by following equation:

$$\vec{E} = \vec{E}_0 e^{iK_t - i\omega t} \qquad (2.9)$$

By substituting K_t into Eq.2.9 we get:

$$\vec{E} = \vec{E}_0 e^{-\beta y + ik_t \sin\theta_t x - i\omega t} \qquad (2.10)$$

So evanescent wave is transmitted wave that propagating along the interface between two mediums and attenuates exponentially away from the interface, but this wave does not carry any power [13-15].

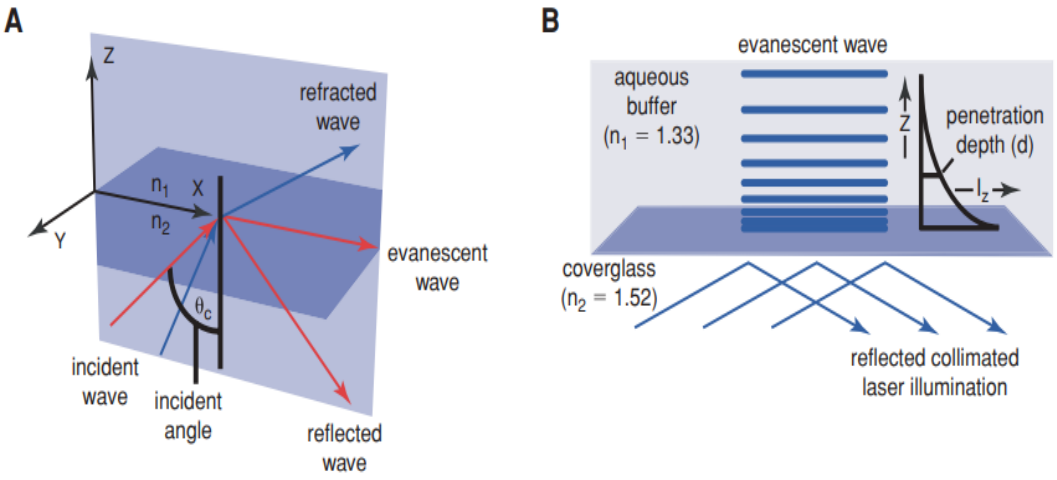

Figure 2-7 Total internal reflection happens at glass – water interface with evanescent wave shown on the right image [16].

2.4 FRUSTRATED TOTAL INTERNAL REFLECTION

As we mentioned in last chapter, when light goes from a denser medium into second medium at an incident angle which is greater than the critical angle of two mediums, all power of incident light will be totally internally reflected to the first medium. At this moment transmitted wave is not disappearing, it still exists but doesn't carry any power, it becomes an evanescent wave that propagates along the interface but attenuates exponentially away from interface.

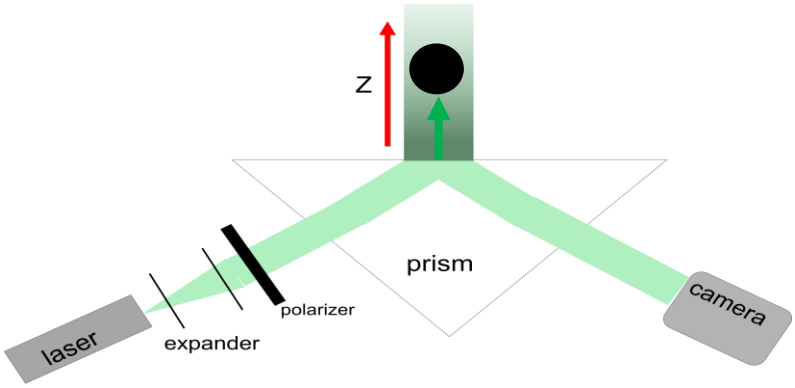

Figure 2-8 Frustrated total internal reflection happens when third medium with higher refractive index is brought extremely close the interface.

The frustrated total internal reflection occurs when a third medium which has higher refractive index than that of the second medium is brought extremely close (within couple of wavelengths of light source) to the interface of the first and second medium. The evanescent wave starts to carry power and transmits into the third medium. At this point, total internal reflection at the boundary of the first and second medium is no longer existing because some energy is carried into third medium, thus not all intensities are reflected. We called this phenomenon frustrated total internal reflection as shown in Figure 2-8.

The frustrated total internal reflection and evanescent wave have been widely explored into different applications. For example, in biotechnology field, it was developed as Total Internal Reflection Fluorescence (TIRF) Microscopy which utilizes evanescent wave to illuminate and excite selected fluorophores instantly adjacent to

interfaces. TIRF makes it possible to visualize fluorescently labeled cells or cell cultures [16-19].

In this thesis we built a simple optical apparatus based on theory of frustrated total internal reflection and verified its ability to measure nanoscale distance between two mediums in near contact region with Hertzian contact theory. Furthermore, we investigated its capabilities of measuring thickness of thin polymer films and deformations of thin films under pressure. Finally, this apparatus was used to visualize and quantify time evolution of contact dynamic between soft semispherical Polydimethylsiloxane lens and smooth glass surface in under water condition.

CHAPTER III

INTRODUCTION OF CONTACT MECHANICS

Polymers have been widely used and researched, from our daily basis such as tires [21], coatings [22-32] and glues [33] to advanced biomimicry technologies in fields of haptics, soft robotics [34] and bio-adhesion due to their characteristic properties such as accessibility, and low cost.

To better explore applications of polymers in these fields, it is crucial to understand the contact mechanics between polymers and substrates, as contact mechanics is directly related to interfacial properties, such as wetting [35], adhesion [36-38], and especially frictions [39].

In this chapter, a broad overview of contact mechanics, interfaces are summarized to serve as a key to understanding contact dynamics.

3.1 DEFINITION OF INTERFACES

Interface, in the physical sciences, is defined as the boundary between two spatial regions occupied by different materials [40], specifically, when one of the phases is air or vacuum, the interface is called surface. For instances, the surface of desk, is called surface because it’s facing air. When water is spreading on desk, the boundary between the water and desk is called interface. Macroscopically, the interface is a boundary

between two phases of distinct matters while in microscopic viewpoint, interface is defined as the region where depletion in density is observed. The surfaces and interfaces of polymer materials have attracted great attention across many research topics. Surfaces and interfaces properties of polymer materials such as adhesion, friction, adsorption, wetting and dewetting are crucial from both the industrial and scientific viewpoints.

Surfaces and interfaces of materials can be studied quantitatively via their surface tensions/energies which give rise to the pervasive phenomenon: adhesion between two surfaces. Adhesion including week van der Waals force and electrostatic force can play significant role in macroscopic scale. In principle, a 1 cm^2 solid block of metal with only the van der Waals force at interface can hang a car's weight. However, these scenarios are never observed in nature, due to adhesion is sensitively depending on actual contact area between two surfaces. Knowing where is in real contact where is in nearly contact at nanoscale between two surfaces become crucial two understand surface/interface properties such as adhesion and friction.

3.2 SURFACE ENERGY AND SURFACE TENSION

The surface energy is the quantification of the work required to disrupt the intramolecular bonds when a solid surface is created. Similarly surface tension is referring to energy required to created liquid surface.

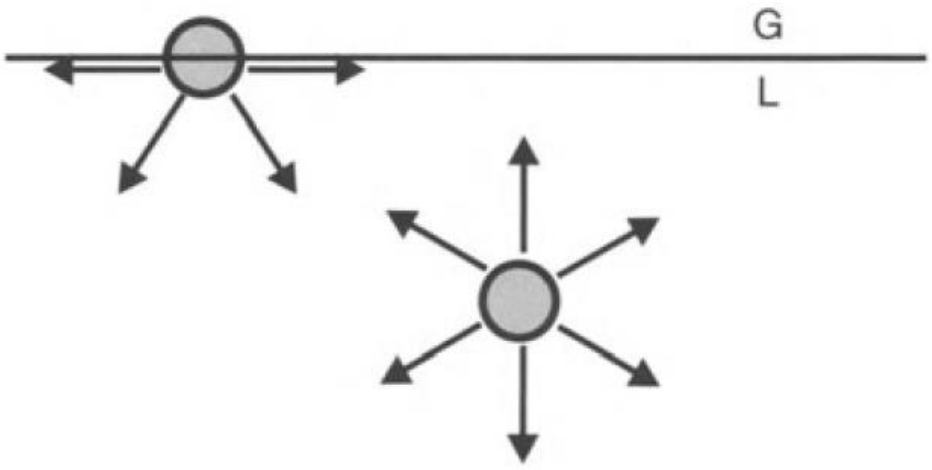

Figure 3-1: Liquid molecules in “happy” and “unhappy” states.

A liquid molecule in the middle of liquid is surrounding by same molecules, interacts and benefits with all its neighbors find itself in a “happy” state. Meanwhile another liquid molecule that stays at surface of liquid and faces the air loses half its cohesion and becomes “unhappy”. This is the main reason that liquid droplet adjusts its shape into spherical to minimize its surface area face to air.

If the cohesion energy of a molecule inside the liquid is *U*, then the molecule sitting at the surface is short of approximately *U/2*. The surface tension can be defined as the direct measurement of shortage of cohesion energy per unit surface area. Assuming a is the size of molecule, then a^2 is the area that exposed to air, the surface tension is of order $\gamma \approx U / 2a^2$, for most of oils, the interactions are of the van der Waals force, then we have $U = kT$, which is the thermal energy.

Table 3-1: Surface tensions of few common liquids.

Liquid	Helium(4K)	Ethanol	Acetone	Cyclohexane	Glycerol
γ(mN/m)	0.1	23	24	25	63
Liquid	Water	Water(100°C)	Molten Glass	Mercury	Water/oil
γ (mN/m)	73	58	~300	485	~50

For water, the interactions between water molecules involves hydrogen bonds, thus the surface tension of water is larger than other liquids ($\gamma = 72mJ\ /\ m^2$). While for solids, they usually have higher surface energy, for example, the interactions between metal molecules are mainly metallic bonds, which is way stronger than hydrogen bonds thus metal has way higher surface energy. Surface tensions of few common liquids are shown in Table 2-1.

3.3 CONTACT ANGLE AND SURFACE WETTABILITY

After knowing the definition of interface and how to quantitatively study the surface using surface energy. The challenge is how can we measure the surface energy/tension

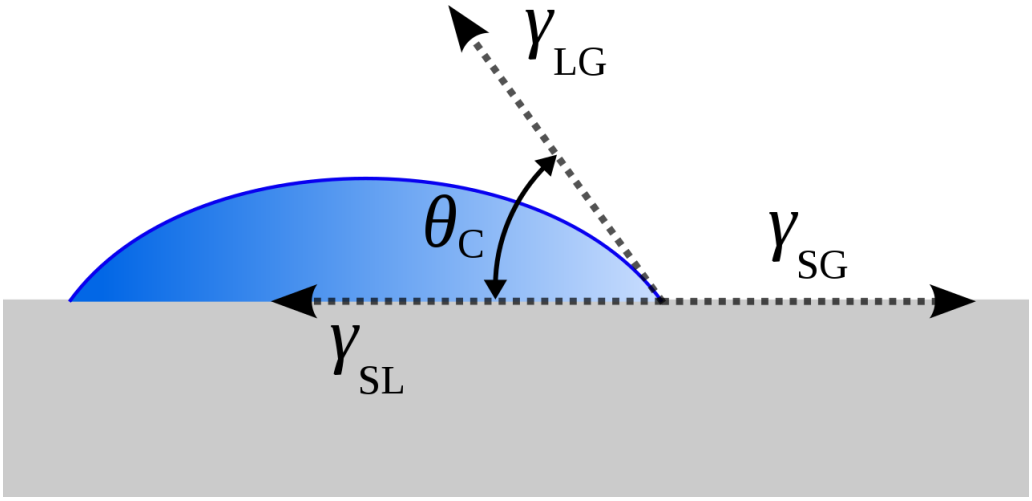

Figure 3-2: Schematic of a liquid drop sitting on solid surface, showing the quantities in Young's equation.

The easiest way to measure the surface energy is contact angle measurements as shown in Figure 3-2. Contact angle, is the shape of the liquid-vapor interface meets a solid surface, which can be used to quantitatively described by Young's equation:

$$\gamma_{SG} = \gamma_{SL} + \gamma_{LG}\cos(\theta_C) \qquad (3.1)$$

In Eq.3.1, γ_{LG} is the surface tension of liquid, γ_{SG} is the surface energy of solid, and γ_{SL} is the interfacial energy of solid and liquid, and θ_C is the equilibrium contact angle of given system. Based on Young equation, a well-defined system of liquid, vapor(gas), and solid at a given state (certain temperature, pressure etc..) has an exclusive equilibrium contact angle. In practice, the equilibrium contact angle is within range of dynamic contact angle from minimum value receding contact angle to maximum value

advanced contact angle [41], and can be calculated from these values, which we will talk about later. Overall, the Young's equation can be used to calculate the surface tension of liquid, surface energy of solid, or even interfacial energy between solid and liquid. The equilibrium contact angle θ_C is the parameter that can indicate the relative strength of the molecular interactions of given system.

Combining the Young equation (Eq.3.1) with Dupré equation (Eq.3.2) can relate the contact angle with the work of adhesion thus leading to Young–Dupré equation as shown in Eq.3.3 [35].

$$W_{SL} = \gamma_{SG} + \gamma_{LG} - \gamma_{SG} \qquad (3.2)$$

$$\gamma_{LG}(1 + \cos(\theta_{SL})) = W_{SL} \qquad (3.3)$$

With Young–Dupré equation, the measurement of work of adhesion could be simplified. For example, by measuring the contact angle of water drop sitting on glass slides, using Eq.3.3 you can calculate work of adhesion between water drop and glass slide.

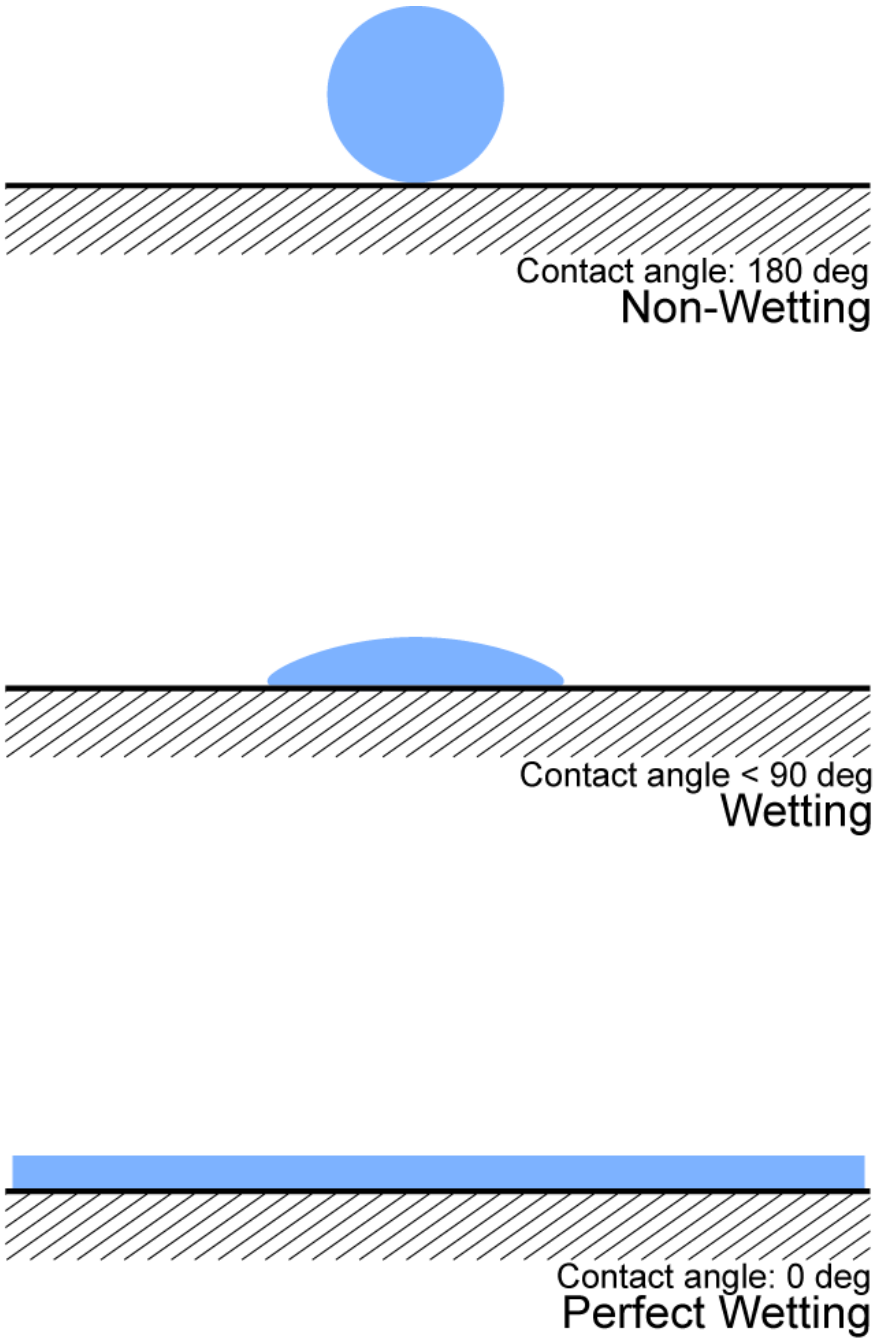

Figure 3-3: Contact angles: non-wetting, partially wetting, perfect wetting. Image from Wikipedia, By Arsteven.

In 1964, Zisman published an method by applying different liquids with known surface tensions of liquids on top of solid surface with unknown surface energy, with cosine of measured contact angle of liquids and graphing them against the surface tensions of liquids yield the critical surface tension of solid surface [42], this method is called “Zisman Plot” as shown in Figure 3-4, a very quick and easy method to measure critical surface tension which is the liquid with highest surface tension that can completely wet the given solid surface. Note that critical surface tension is not same as surface energy of solid but generally smaller than surface energy. The surface energy of solid surface could be measured and calculated by Fowkes’ theory which takes dispersion force, polar force, hydrogen bonding force, induction force (Debye), acid/base force, etc... into consideration [44].

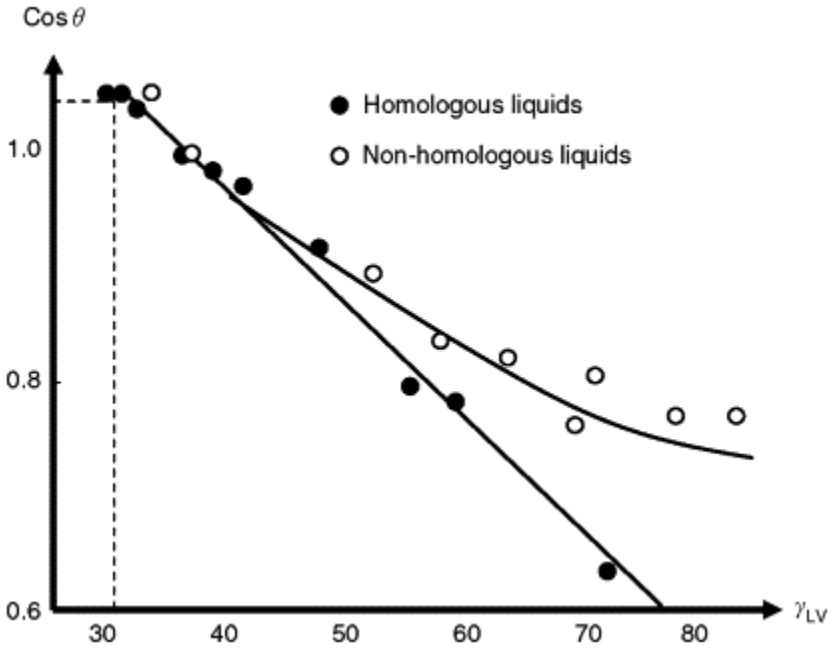

Figure 3-4: Zisman plot for both homologous and non-homologous liquid.

Even though the "Zisman Plot" can't directly measure surface energy of given solid surface, but it's still a very useful way to estimate wettability of solid surface. As shown in Figure 3-3, if contact angle is small, then the surface has good wettability, in contrast, if contact angle is large, then surface has bad wettability. Similarly, if a droplet of water is applied on a given solid surface, the contact angle of water drop can be used indicate the surface wettability of water.

If contact angle $\theta = 0°$, then we say the liquid is completely wets the substrate, if $0° < \theta < 90°$, then this surface has good wettability, generally these types of surfaces are called hydrophilic surfaces. Reversely, if $\theta = 180°$, then water doesn't wet the surface at all, in same way, if $90° < \theta < 180°$, surface doesn't have good wettability of water, these types of surfaces are called hydrophobic surfaces.

As surface energy is one of the most significant parameters that play in wetting phenomena, it can also be utilized to represent surface wettability mathematically, the spreading parameter:

$$S = \gamma_{SV} - \gamma_{LV} - \gamma_{SL} \qquad (3.4)$$

As shown in Eq.3.4, the spreading parameter can be determined mathematically by using γ_{LV} the surface tension of liquid, γ_{SV} the surface energy of solid, and γ_{SL} the interfacial energy between liquid and solid. When $S < 0$, the liquid is partially wetting the solid surface, otherwise the liquid is completely wetting the substrate.

3.4 DYNAMIC CONTACT ANGLE

In practice, a given system of solid-liquid-vapor could yield a continuous range of contact angle due to surface inhomogeneity and surface roughness, this phenomenon is called contact angle hysteresis. The largest value of dynamic contact angle is called advancing contact angle θ_A while the smallest value is referred to receding contact angle θ_R. Both advancing and receding contact angle could be measured via dynamic experiments where droplets or liquid bridges are moving as shown in Figure 3-5 [41].

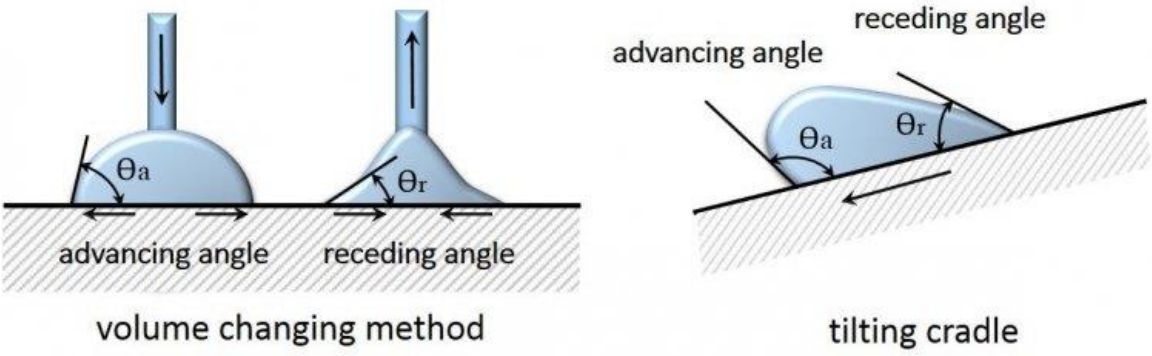

Figure 3-5: Advancing and receding contact angle measurement. Image from Weistron Co.

The Young–Dupré equation assumes that solid surface is homogeneous and frictionless. However, a real surface should take roughness and contamination into account which will result in contact angle hysteresis, the equilibrium contact angle θ_c can be calculated from advancing and receding contact angle as shown:

$$\theta_C = arccos\left(\frac{r_A \cos\theta_A + r_R \cos\theta_R}{r_A + r_R}\right) \qquad (3.5)$$

where

$$r_A = \sqrt[3]{\left(\frac{sin^3\theta_A}{2-3\cos\theta_A + cos^3\theta_A}\right)} \qquad (3.6)$$

$$r_R = \sqrt[3]{\left(\frac{sin^3\theta_R}{2-3\cos\theta_R + cos^3\theta_R}\right)} \qquad (3.7)$$

In most cases, for a chemically homogeneous surface, the contact angle hysteresis is caused by surface roughness, which has strong effect on wettability of surface. The effect of surface roughness depends on the real contact area between liquid and surface, for example, if liquid wets the grooves of surface, then the real contact area is large, otherwise some air bubbles could be trapped to reduce the actual contact area. When the liquid completely wet the grooves of surfaces, it is called Wenzel state. Wenzel was the first to evaluate the equilibrium contact angle of a rough surface based on roughness ratio, which is defined as the ratio between the actual contact area and projected contact area, $r_{true} = A_{true}/A_{pro}$, and the Wenzel equation can be written as Eq.3.8:

$$\cos\theta^* = r_{true}\cos\theta \qquad (3.8)$$

In Eq.3.8, θ^* is the measured contact angle, θ is the Young's contact angle when surface is homogeneous and smooth. For a rough surface, the roughness ratio is always greater than 1. Wenzel equation is applicable when the size of droplet is larger than the

roughness scale by two to three orders of magnitude and becomes more accurate as drop size becomes larger compared to the scale of roughness [45].

In case of droplet sitting on hydrophilic surface Eq.3.8 indicates that roughness will enhance the surface wettability. In contrast, when droplet sits on a hydrophobic surface, the roughness will increase the surface hydrophobicity. This can be explained from theoretical side, for $\theta > 90°$,and $r_{true} \gg 1$, the measured contact angle could reach to $\theta^* \sim 180°$, thus surface becomes superhydrophobic due to effect of roughness. However, in practice, this phenomenon can barely happen. Because for hydrophobic surface, the droplet can't completely wet the grooves.

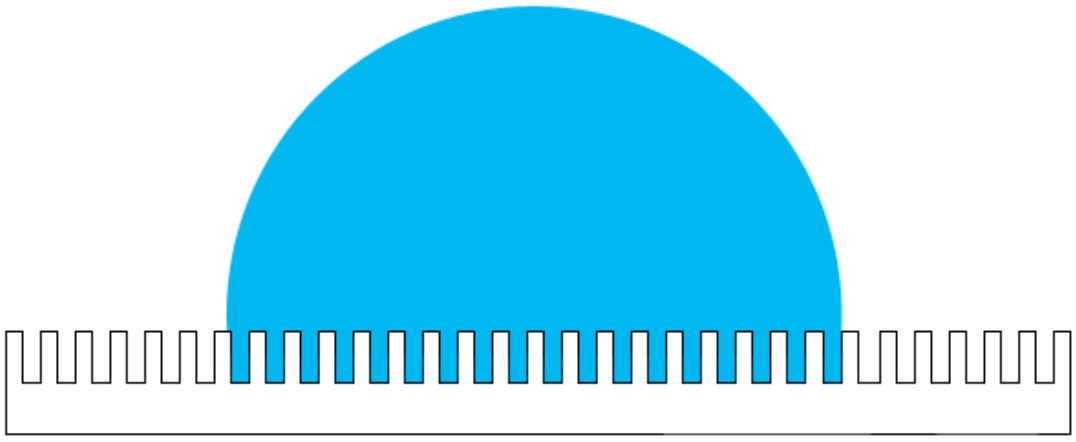

Figure 3-6: Wenzel model of droplet sits on rough surface, the droplet completely wet grooves of surface. Image from Wikipedia.

When surface is hydrophobic or heterogeneous, the situation is complex. The droplet can't completely wet the grooves, leaving air pockets within grooves instead, which causes less wetting as shown in Figure 3-7. This phenomenon can be described by Cassie-Baxter model in Eq.3.9 as written:

$$\cos\theta^* = \phi_{wet} r_{true} \cos\theta + \phi_{wet} - 1 \qquad (3.9)$$

In Eq.3.9, r_{true} is the roughness ratio as we mentioned before, ϕ_{wet} is the fraction of wetted surface area. When $\phi_{wet} = 1$, Eq.3.9 is same as Eq.3.8, so Wenzel is a special case of Cassie-Baxter model [46].

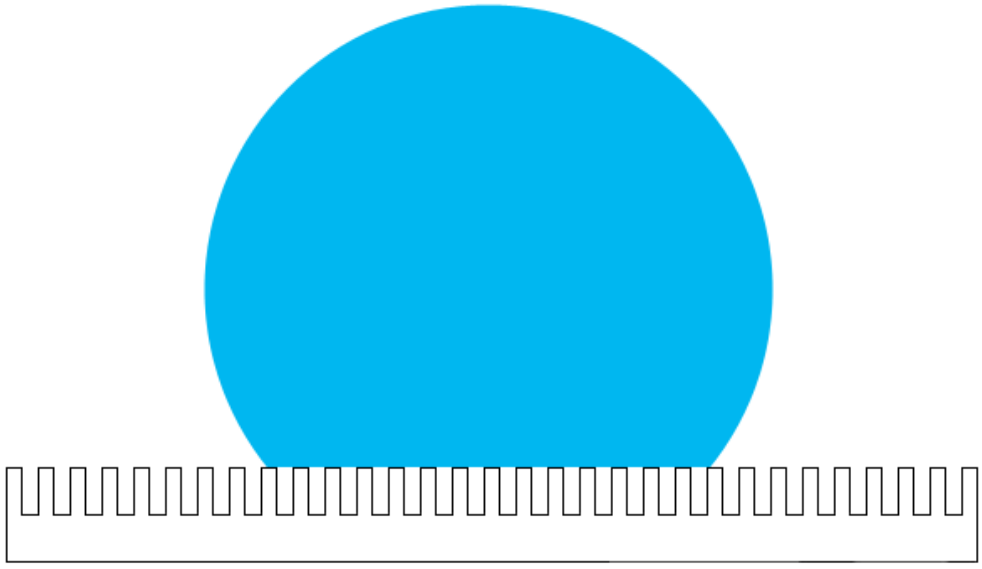

Figure 3-7: Cassie-Baxter model of droplet sits on rough surface with air pockets entrapped in grooves. Image from Wikipedia.

The wetting transition from one state to another state has been researched widely in recent years, especially one-way transition from less stable (metastable) Cassie-Baxter state to more stable Wenzel case. During this process, liquid begins to nucleate from the middle and propagates to the edge of droplet as shown in Figure 3-8. Other people have reported the propagation could happen from the edge droplet to middle of droplet as shown in Figure 3-9.

The root cause of wetting transition was dominated by the competition between the external forces and energy barrier. External forces such as vibration, mechanical impact, compress and particularly Laplace pressure can overwhelm the energy barrier to trigger the wetting transition.

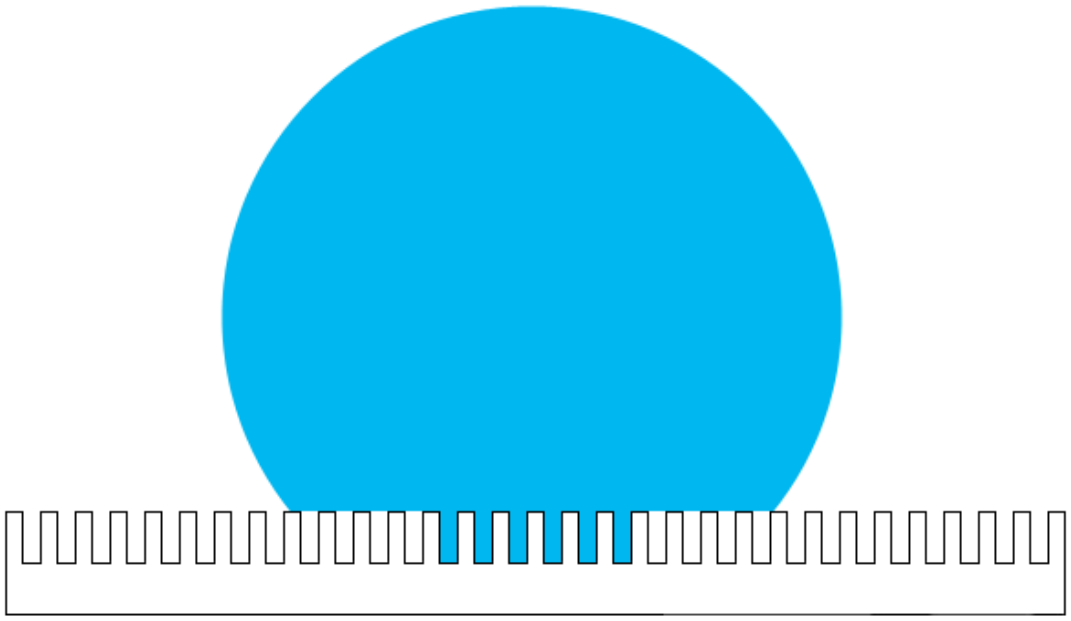

Figure 3-8: Wetting transition from Cassie-Baxter state to Wenzel state. Image from Wikipedia.

In fact, the wetting transition can be reversible if both states are thermodynamically stabilized by changing thermodynamic variables such as pressure and temperature or by applying external forces [47].

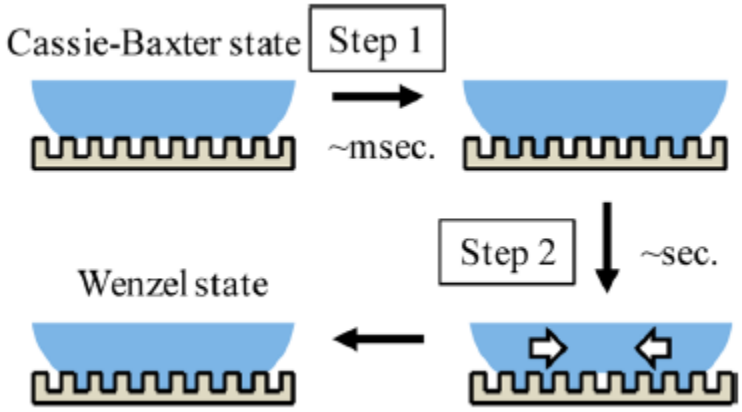

Figure 3-9: Wetting transition from Cassie-Baxter to Wenzel state. Beginning from the edge of droplet to center of droplet [47].

3.5 HERTZIAN CONTACT THEORY

The deformation of two solids is depended on contact mechanics when they are brought into contact. Directions of stresses along the contact interface could be either perpendicular to the interface or parallel to the interface, which is determined by the

direction of applied external load. In this thesis, we will discuss frictionless contact mechanics with only perpendicular load applied.

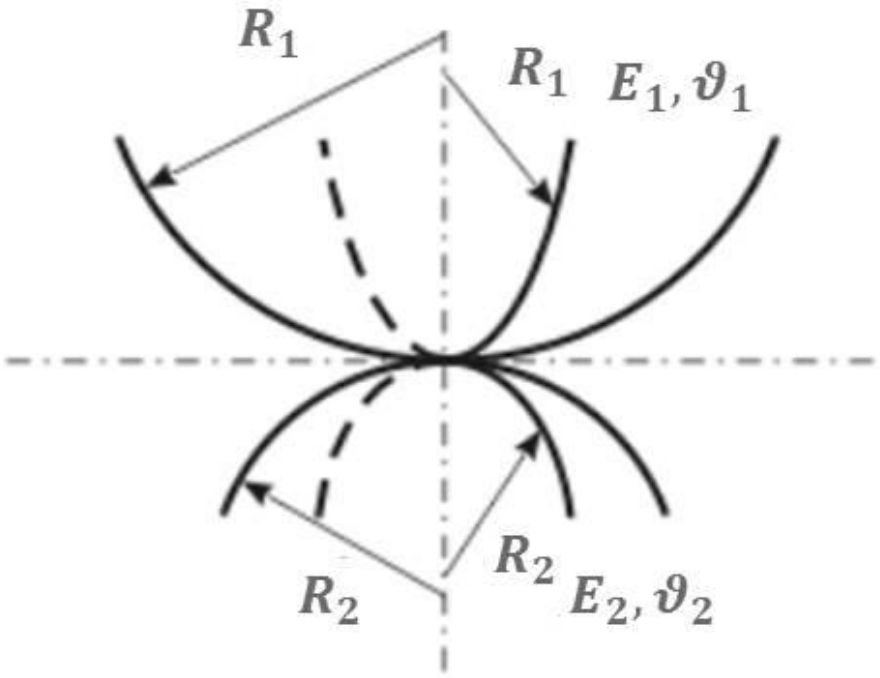

Figure 3-10: Hertzian contact for two spheres contact with each other.

In 1882, Heinrich Hertz first studied contact mechanics between two elastic objects with smooth surfaces in contact with each other [48]. For special cases of Hertz contact which is contact between two elastic spheres with modulus E_1 and E_2, radii R_1 and R_2 respectively, squeezed against each other under external load that perpendicular to the contact interface as shown in Figure 3-10, or the contact between a sphere and the surface of a half space as shown in Figure 3-11. For the case of two spheres in contact

with each other, the radius of contact was calculated based on minimizing the stored elastic energy due to deformation caused by external forces and is written as Eq.3.10:

$$a = \left(\frac{R_1 R_2}{R_1 + R_2}\right)^{1/3} \left(\frac{3F(1-\upsilon^2)}{4E^*}\right)^{1/3} \qquad (3.10)$$

where

$$\frac{(1-\upsilon^2)}{E^*} = \frac{(1-\upsilon_1^2)}{E^1} + \frac{(1-\upsilon_2^2)}{E^2} \qquad (3.11)$$

where ν_1 and ν_2 are the Poisson ratios of the two solids. The deformation distance that perpendicular to the interface of contact is given by Eq.3.1:

$$h = \left(\frac{R_1 + R_2}{R_1 R_2}\right)^{1/3} \left(\frac{3F(1-\upsilon^2)}{4E^*}\right)^{2/3} \qquad (3.12)$$

where h is also called total indentation.

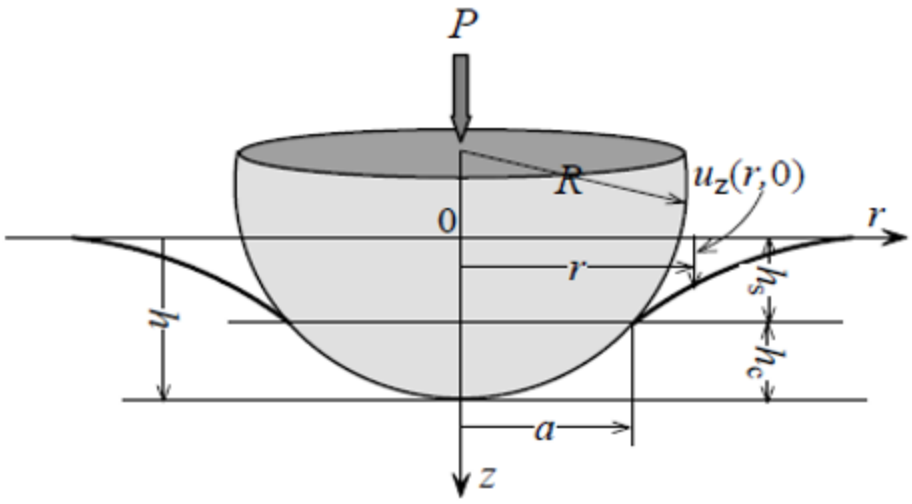

Figure 3-11: Hertzian contact for a sphere contact with elastic half-space.

For case of a sphere in contact with flat surface, one can think is the radius of curvature for a flat surface is infinity, which means $R_2 = \infty$. As shown in Figure 3-11. Under external load P , the radius of contact presented in Eq.3.10 can be simplified as:

$$a = \left(\frac{3PR}{4E^*}\right)^{1/3} \tag{3.13}$$

Where E^* is same as the one in Eq.3.11. Then the total indentation or the deformation distance can be written as:

$$h = \frac{a^2}{R} \tag{3.14}$$

Outside the contact region ($r > a$) gap distance between two bodies is:

$$d = \frac{r^2}{2R} + u_z - h \tag{3.15}$$

Where u_z is the combined elastic deformation of two bodies, or the displacement of points on the flat surface outside the contact area, which can be written as:

$$u_z = \frac{a^2}{\pi R r^2}((2a^2 - r^2)sin^{-1}\left(\frac{a}{r}\right) + ar(1 - \left(\frac{a^2}{r^2}\right))^{\frac{1}{2}} \qquad (3.16)$$

For other cases such as contact between two cylinders with parallel axes, contact between a rigid conical indenter and half-space, contact between two crossed cylinders, and contact between rigid cylindrical indenter and half-space as shown in Figure 3-12 can also be derived.

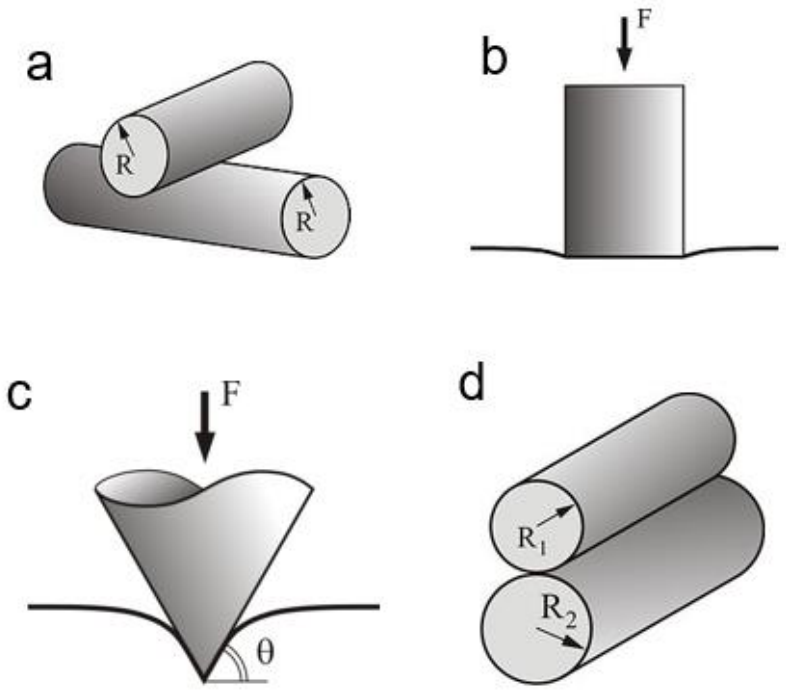

Figure 3-12: Hertzian contact. (a) contact between two crossed cylinders. (b) contact between a rigid cylindrical indenter and half-space. (c) contact between a rigid conical indenter and half-space. (d) contact between two cylinders with parallel axes.

3.6 JOHNSON-KENDALL-ROBERTS (JKR) CONTACT THEORY

Hertzian contact theory assumes the contact between two objects is non-adhesive contact which means there is no surface interaction, or the surface interaction compared with applied load is too weak to be considered. Let's assume externally applied load is relatively weak and contact area is small, thus the adhesive force/adhesion due to van der Waals force, capillary, liquid-bridges forces, or electric static forces are becoming dominated. In this case, the original Hertzian theory which doesn't account effect of adhesion may not be applicable.

In 1971, Johnson, Kendall and Roberts further developed Hertzian contact theory. Upon their observation, when two solid surfaces are brought into close contact at low loads, the attractive adhesion (van der Waals forces, surface attraction, capillary, liquid-bridges forces) are playing crucial role that cause the contact area is larger than that predicted by Hertzian contact theory as shown in Figure 3-13, moreover, after removing the low external loads, the area of contact has a non-zero value.

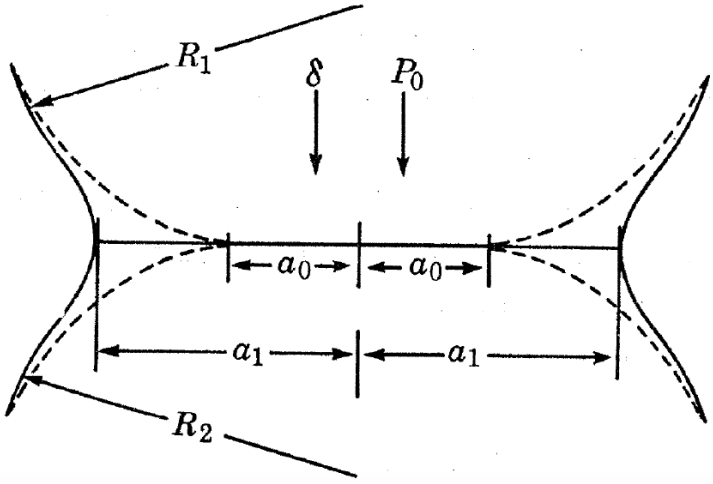

Figure 3-13: JKR contact model with effect of adhesion accounted. a_0 is the radius of contact predicted by Hertz, a_1 is the radius of contact predicted by JKR model. Apparently $a_1 > a_0$.

JKR contact model is originated from Hertz contact model but incorporating the effect of adhesion within the area of contact by balancing stored elastic energy and the loss in surface energy. The apparent load or total load (P_1) between adhesive contact bodies including effect of adhesion is higher than the external applied load (P_0) can be expressed in Eq.3.17 as shown:

$$P_1 = P_0 + 3\pi RW + \sqrt{6\pi RWP_0 + (3\pi RW)^2]} \qquad (3.17)$$

With known apparent load, the radius of contact originated from Hertzian theory but incorporated with work of adhesion can be generated as:

$$a^3 = \frac{3R}{4E^*}\left[P + 3\pi RW + \sqrt{6\pi RWP + (3\pi RW)^2}\right] \qquad (3.18)$$

Note that is we assume there is no work of adhesion ($W = 0$) then the Eq.3.18 is same as Eq.3.13 indicates that JKR model is originated from Hertzian theory. On the other hand, if we assume there is no applied load ($P_0 = P = 0$), the radius of contact will become a non-zero value:

$$a^3 = \frac{3R(6\pi RW)}{4E^*} \qquad (3.19)$$

Which matches the observation mentioned above, after removing the external load, the contact area is a non-zero value. During removing the externally applied load P_0, the apparent load P_1 decrease with decreasing of applied load P_0, after completely remove the applied load ($P_0 = 0$), additional force is required to sperate two surfaces and can be written as:

$$P_{pull-off} = -\frac{3}{2}\pi RW \qquad (3.20)$$

Note that this pull-off force is independent of moduli of two objects.

3.7 DERJAGUIN-MULLER-TOPOROVE (DMT) MODEL

JRK model is considering effect of adhesion within contact area, while alternatively DMT model assumes that contact dynamic within contact area is same as that of Hertzian contact theory, but additional attractive interactions (adhesion) is acting outside the contact area.

Based on this theory, the radius of contact between two elastic spheres is given by:

$$a^3 = \frac{3R}{4E^*}(P + 4\pi RW) \qquad (3.21)$$

The pull-off force to achieve zero contact area or to sperate two surfaces is:

$$P_{pull-off} = -2\pi RW \tag{3.22}$$

In 1977, Tabor parametrized the contradiction between the JRK and DMT models by a single parameter called Tabor parameter (μ) given by:

$$\mu = \left[\frac{RW^2}{E^{*2}{z_0}^3}\right]^{\frac{1}{3}} \tag{3.23}$$

Where z_0 is the equilibrium distance between two elastic spheres in contact. It turns out JRK model is applicable to large, compliant spheres in contact with larger μ, while DMT model is applicable for small and rigid spheres in contact with smaller value of μ.

CHAPTER IV

QUANTITATIVE FRUSTRATED TOTAL INTERNAL REFLECTION (FTIR) FOR THIN FILM CHARACTERIZATION

The adhesion and friction strategies are known to sensitively depends on the interactions between two contact mediums, knowing where is in far contact, where in actual contact, and where is in near contact down to nanoscale is crucial to better understand adhesion and friction. A precise and accurate measurement of nanoscopic gap thickness is necessary to quantitatively study the contact dynamics of between two mediums. In recent years, frustrated total internal reflection (FTIR) has been prompted as a robust tool to directly image and quantitatively resolve the contact formation between two surfaces. However, many studies utilized the simple intensity exponential decay function of evanescent field which didn't account multiple reflections and refractions at the interface were potentially underestimated the actual distance in near contact region. Here in this chapter, we utilized the Fresnel equations to total up multiple reflections and refractions to accurately render measured intensity of frustrated total internal reflection. Furthermore, quantitative validation of FTIR were performed by placing a convex lens with known radius of curvature on flat glass prism surface, comparing measured height profile with Hertzian contact theory and obtained great agreement. Moreover, the

potential of FTIR technique to measuring thin polymer film were evaluated and compared with Ellipsometer results.

4.1 INTRODUCTION

As we mentioned earlier in the thesis, total internal reflection happens at when light goes from a denser (higher refractive index) medium into a less dense (lower refractive index) hit the interface at an incident angle which is greater than the critical angle of two mediums. At this circumstance, all intensities of incident light are internally reflected, not energy can transmit into second medium. However, the transmitted light (refraction) isn't disappearing, it becomes an evanescent field that propagates along the interface and attenuates exponentially away from the interface. When a third medium with higher refractive index than that of the second medium is brought very close to the interface, total internal reflection is frustrated, energy from reflected light starts to transmit into third medium via evanescent wave. By analyzing the intensity change of the reflected light, distance between the third medium and the interface can be obtained.
In recent years, frustrated total internal reflection has been widely used in researching field of contact dynamics. In 2017, Brygida utilized this technique to directly visualize contact formation between human fingers and glass surfaces, further quantifying the growth of contact area verse time [50]. Observation shows when human fingers in contact with hard, smooth surface, the area of contact grows relative slow and follows a first-order kinetics relationship.

The process of human fingers giving rise to contacts with soft objects such as soft rubber is intuitively faster than that of contacts with hard surfaces as shown in Figure 4-1.

This experiment perfectly revealed and explained why pen has rubbery grips. With soft rubbery grips, the contact area between fingers and grips can grow very fast so adhesion and friction will be strong enough for human to hold pens tightly.

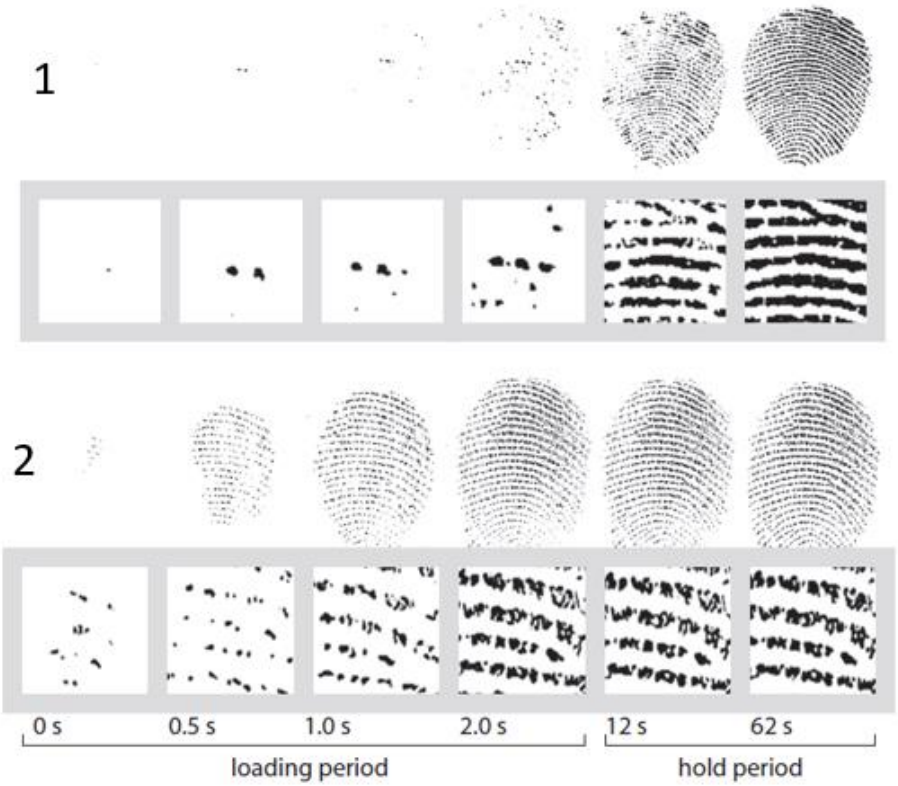

Figure 4-1: (1) Contact formation between finger and hard, smooth surface. (2) contact formation between finger and soft rubbery surface [50].

In 2016, Needham used this technique to directly image real contact area of footwear as shown in Figure 4-2. In his setup, couple of LEDs are placed under the corners of glass waveguide to achieve total internal reflection inside it, cameras are placed underneath the waveguide to capture the intensity change [51]. Further analysis could convert the intensity profile into pressure profile based on strength of intensity.

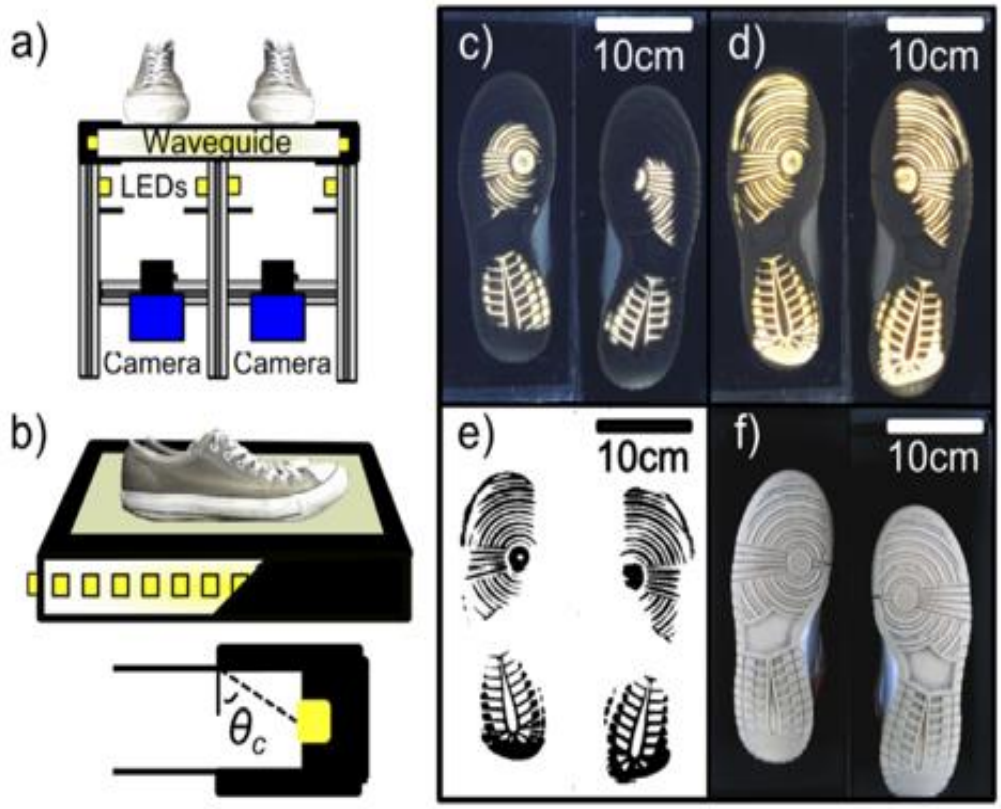

Figure 4-2: (a) FTIR setup. (b)Total internal reflection is achieved by placing LEDs under the corner. (c)-(f) Images obtained via cameras [51].

Furthermore, Eason utilized same setup as shown in Figure 4-3 to directly measure stress distribution and contact area under gecko foot via high-resolution tactile sensing array which is made from polydimethylsiloxane (PDMS). When external compressive force is applied on sensing array the small bumps will be deformed which frustrates total internal reflection leads intensity of reflection changes.

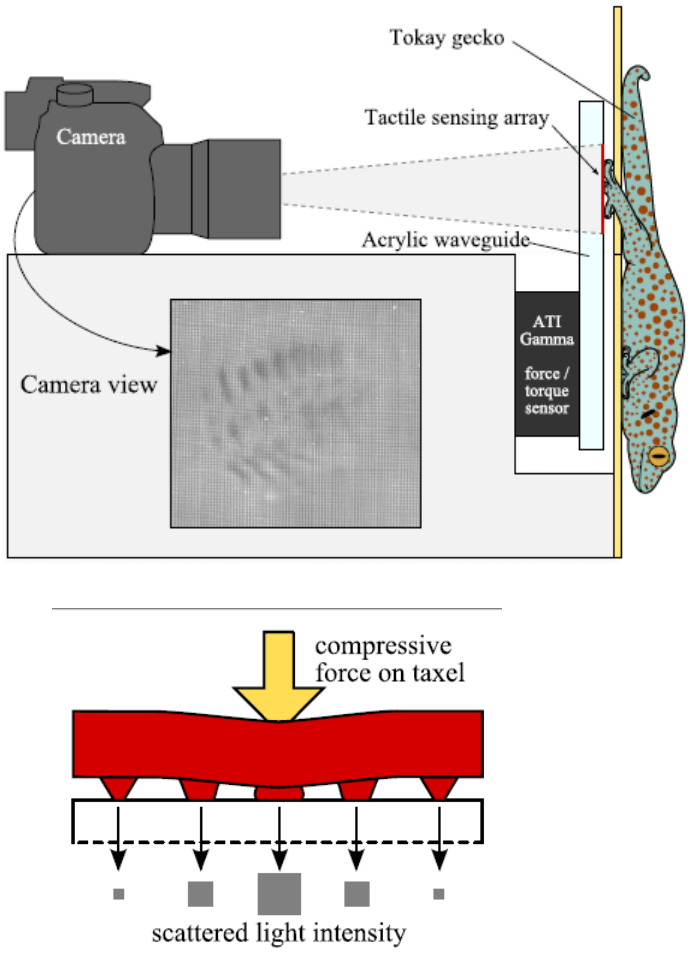

Figure 4-3: FTIR setup with tactile sensing array for stress distribution and contact area measurement [51].

In 2014, Kolinski used simpler version of FITR that composed of glass prism, laser, and fast camera to visualize dynamic of water droplet impacts on glass surface as shown in Figure 4-4 [52]. In his experiment, total internal reflection is achieved at glass-air interface, when water droplet is approaching very closely to the interface but not actually in contact with interface, the total internal reflection is frustrated, energy of incident light is transmitted into water droplet, a dark ring is observed at this moment. As

the distance from water droplet to interface gets shorter, more energy starts to transmit into droplet thus the ring is getting expanded and darker. Eventually when droplet is touching the interface, the interface of glass-air is replaced by glass-water interface, at this point, most of energy transmitted into water, completely dark area shows up. It is interesting that when droplet is very close to the interface, a hollow ring rather than solid circular area is observed. The reason is resistance from air can deform water droplet into concave shape when it's moving, so there is air entrapped.

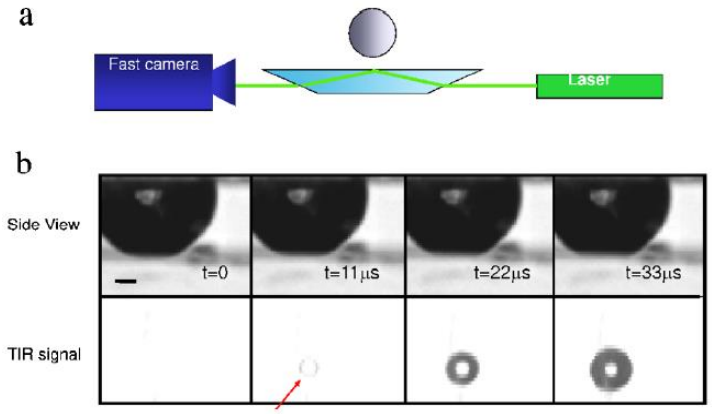

Figure 4-4: (a) FTIR Setup composed of laser, fast camera, and prism. (b) dynamic of water drop impact prism surface, upper is sideview, lower is image from fast camera [52].

Kolinski then used evanescent wave exponentially decay function in Eq.4.1 to directly calculate distance between droplet and prism surface at each frame as shown in Figure 4-5.

$$I = I_0 e^{-z/k} \qquad (4.1)$$

Where I is intensity of evanescent wave, z is distance between droplet and interface. k is penetration depth given by Eq.4.2 as shown:

$$\frac{1}{k} = \frac{4\pi}{\lambda}\sqrt{n_1^2(sin\,\theta_1)^2 - n_2^2} \qquad (4.2)$$

Where λ is the wavelength of the light source.

However, the most recent work from Chao indicated that Kolinski's method assumes energy transmits into droplet are absorbed which neglects multiple reflection and refraction happen at the interface is underestimating the distance between droplet and prism surface [53]. The underestimation could lead to significant impact on understanding adhesion and friction behaviors as they are known to depends sensitively on interactions happening in near contact region down to nanoscale.

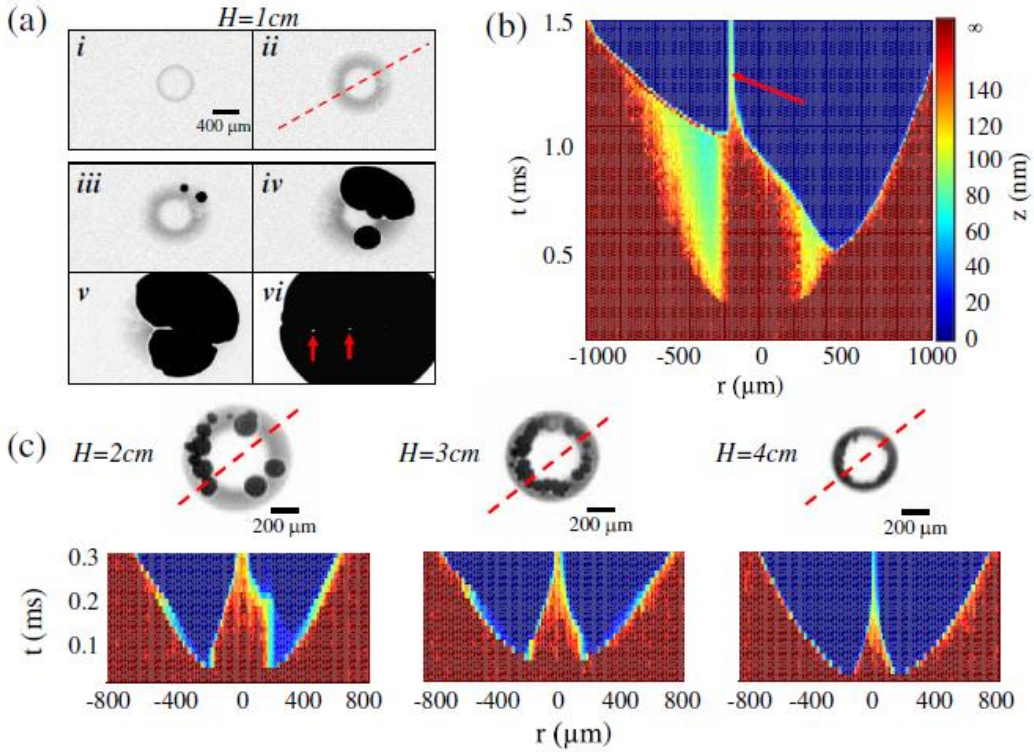

Figure 4-5: (a) FTIR image of droplet impact on glass surface. (b) and (c) distance analysis of each frame [53].

In next section, we will go through the theoretical design of quantification of FTIR and explain why Kolinski's method is underestimating the gap thickness.

4.2 THEORETICAL DESIGN OF FTIR

Let's consider the similar system as Kolinski's experiment the glass-air-water three mediums system as shown in Figure 4-6. Light goes from glass into air and third medium water is very close to glass-air interface. The refractive index of glass n_1, refractive index of air n_2 and refractive index of water n_3 should follow $n_1 > n_3 > n_2$.

Let's first consider condition of incident angle is less than critical angle ($\theta_i < \theta_c$). Under this condition, as shown in Figure 4-6, light goes from glass into air, at the interface, partial energy of light reflects to glass and rest energy of light transmits through the interface and hit the interface of air-water then same reflection and refraction happen again causes multiple reflections and transmissions at both glass-air and air-water interfaces.

If the distance between the water phase and the glass phase is d, which is the thickness of air phase. The optical path difference or equivalently, the phase difference of the successive reflected light can be expressed by Eq.4.3 as given by:

$$\delta = \frac{4\pi d}{\lambda}\sqrt{n_2^2 - n_1^2\, sin^2\, \theta_i} \qquad (4.3)$$

Then amplitude of reflected wave can be calculated by multiplying the $e^{j\delta}$, where j is the imaginary unit. To total up all the reflected light, it is necessary to understand how to connect the refraction and reflection coefficients of Fresnel equation as we mentioned in Eq.2.2 – Eq.2.5.

As shown in Figure 4-7, when light goes from one medium to another medium, partial of light energy is reflected and rest is refracted. If there is no energy absorbed by mediums, then this system is reversible. In 3rd picture of Figure 4-7 light ray x should have same amplitude as incident beam while light ray y should have zero amplitude. Stokes relation can be deducted as given by Eq.4.4 and Eq.4.5:

$$t'tE + r^2E = E \qquad (4.4)$$

$$r'tE + tr\,E = 0 \qquad (4.5)$$

Where t and r are refractive and reflective coefficients provided by Fresnel equations in Eq.2.2 to Eq.2.5.

The amplitudes of each reflected light beam can be expressed using the amplitude of incident light E, starts from the first reflected light beam they are: $r_{12}E$, $t_{12}t_{21}r_{23}Ee^{j\delta}$, $t_{12}t_{21}r_{21}r_{23}^2Ee^{2j\delta}$ …, By adding them up we can get the total reflectance as written in Eq.4.6:

$$r = \frac{r_{12}+r_{23}e^{j\delta}}{1+r_{12}r_{23}e^{j\delta}} \qquad (4.6)$$

As we mentioned above r is provided by Fresnel equations which is polarization dependent. By substituting Eq.2.4 we get total reflectance for P-polarization as shown below:

$$\hat{r} = \frac{\left(\frac{n_2\cos\,\theta_1 - n_1\cos\,\theta_2}{n_2\cos\,\theta_1 + n_1\cos\,\theta_2}\right) + \left(\frac{n_3\cos\,\theta_2 - n_2\cos\,\theta_3}{n_2\cos\,\theta_3 + n_3\cos\,\theta_2}\right)\exp\left(j\left(\frac{4\pi d}{\lambda}\sqrt{n_2^2 - n_1^2\sin^2\,\theta_1}\right)\right)}{1 + \left(\frac{n_2\cos\,\theta_1 - n_1\cos\,\theta_2}{n_2\cos\,\theta_1 + n_1\cos\,\theta_2}\right)\left(\frac{n_3\cos\,\theta_2 - n_2\cos\,\theta_3}{n_2\cos\,\theta_3 + n_3\cos\,\theta_2}\right)\exp\left(j\left(\frac{4\pi d}{\lambda}\sqrt{n_2^2 - n_1^2\sin^2\,\theta_1}\right)\right)} \qquad (4.7)$$

From Eq.4.7 if we know the incident angle θ_1, wavelength of light source λ, with measured total reflectance, then the distance between first medium and second medium can be calculated.

Let' now consider the situation where incident angle is greater than critical angle ($\theta_i > \theta_c$). As we talked earlier in Section 1.3, Eq.4.3 becomes an imaginary number, while $e^{j\delta}$ becomes a real number $e^{-\delta'}$ where $\delta' = \frac{4\pi d}{\lambda}\sqrt{-n_2^2 + n_1^2\,sin^2\,\theta_i}$, then $e^{-\delta'}$ is an exponential decay function which is evanescent wave that attenuate away from the interface. In contrary, the refractive angle is becoming imaginary number. Therefore, the reflective coefficients become complex number a as well, the absolute values of reflective coefficients equal to 1 which describe the condition of total internal reflection. Overall, the total reflectance Eq.4.7 is still eligible to calculate the total reflectance regardless of relation between incident angle θ_i and critical angle θ_c.

If we plot the gap thickness d verse total reflectance r. Kolinski's method of using simple exponential decay function which neglects the multiple refraction and reflection of light is underestimating the gap thickness as shown in Figure 4-8.

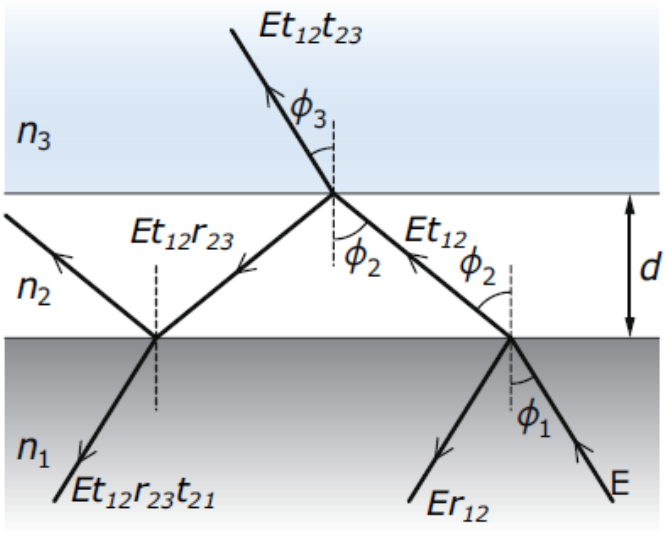

Figure 4-6: Three mediums system to show geometry at interface with multiple refraction and reflection [53].

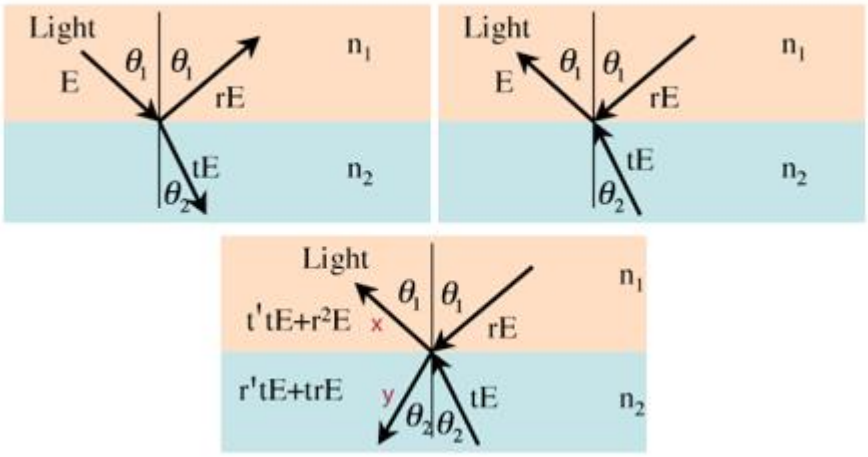

Figure 4-7: Stokes relations. If there is no absorption, (1) and (2) should be reversible.

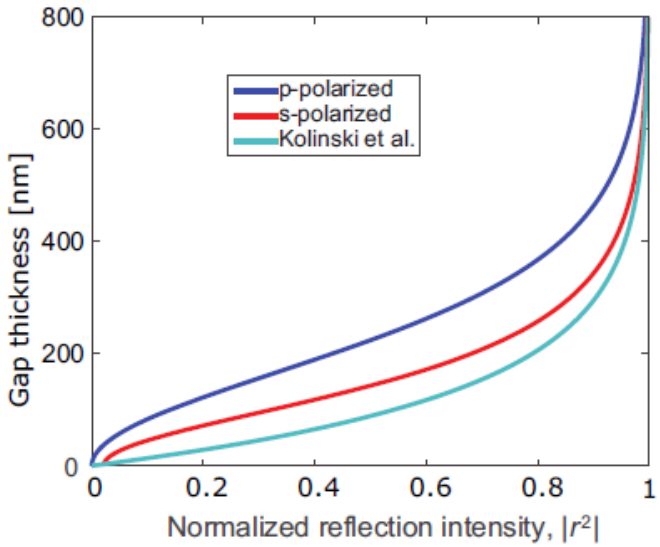

Figure 4-8: At fixed system, Kolinski's method is underestimating gap thickness [53].

4.3 EXPERIMENTAL SETUP AND DATA ACQUISITION

A schematic of frustrated total internal reflection (FTIR) setup is shown in Figure 4-9. Light beam comes from red LED (M660L4, $\lambda{\sim}665nm$, from Thorlabs) passes through linear polarizer to be polarized into P-polarization then reflected by two mirrors to illuminate the top surface of the NBK-7 glass dove prism with refractive index $n_1 = 1.52$, at an incident angle which is greater than the critical angle of glass-air interface ($\theta = 41°$), but less than critical angle of glass-water interface ($\theta = 61°$) to achieve total internal reflection at glass-air interface. A circular shape water droplet is then placed on top of prism surface to help accurately determine incident angle θ_i.

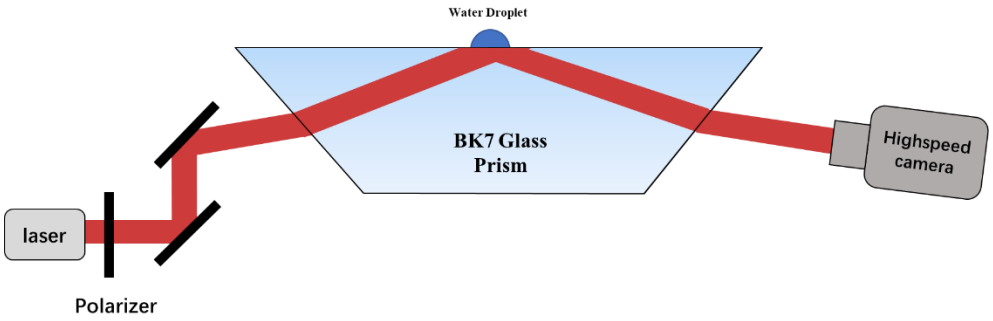

Figure 4-9: Experimental setup. A circular shape water droplet is placed on prism surface to determine the incident angle.

Light is totally internally reflected at the interface of glass-air, when a spherical waterdrop is place on glass surface that partially the surface with high contact angle, then FTIR happens. Energy starts to transmit into water phase through evanescent wave, a high-speed camera (VEO410 purchased from Phantom) with max resolution of 1280x800 pixels[2] at frame rate 100fps is placed on the other side of the dove prism to collect reflected signal. Due to FTIR, the contact between droplet and glass prism shows dark area in camera signal. However, the circular contact area between droplet and glass is captured as elliptical shape rather than circular shape due to distortion caused by refraction during the optical light path as shown in Figure 4-10. The distortion (D), according to geometrical optics calculations, is a function of incident angle θ_i as written below:

$$D = cos\,\theta_i \left(sin^{-1} \left(\frac{n_2}{n_1} sin \left(\theta_i - \frac{\pi}{4} \right) \right) \right) \qquad (4.8)$$

If we can obtain the distortion, then accurate incident angle θ_i can be calculated consequently.

As shown in Figure 4-10, a dark elliptical contact area is shown, by fitting the edge of dark area into ellipse, the ratio of short axis to long axis which is the distortion D can be obtained. The polar coordinates function of ellipse is shown below:

$$\rho^2 = \frac{a^2 b^2}{b^2 \cos^2\theta + a^2 \sin^2\theta} \qquad (4.9)$$

Where ρ is the distance of edge between origin, a is the long axis and b is the short axis. The aspect ratio of distortion $D = b/a$. With known aspect ratio, the directly method of using Eq.4.8 to calculate incident angle θ_i which is hard, the easiest way to do is doing a look-up table by inputting different θ_i to generate corresponding D as shown in Figure 4-12. Then with known D, the incident angle θ_i can be directly matched.

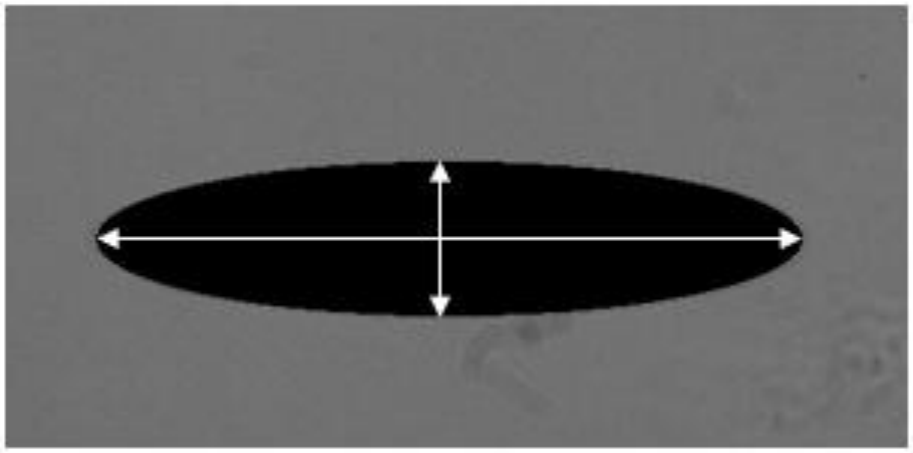

Figure 4-10: Distorted image of water drop in contact with prism surface.

After obtaining the incident angle θ_i, with a given system such as glass-air-water, then we know all the parameters required from Eq.4.7 to calculate distance between the

first and the third medium which is the thickness of the second medium. But due to the nature of the Eq.4.7, it is impossible to calculate gap thickness d from total reflectance r. The best way to obtain d from r is doing look-up table again by inputting gap thickness d to generate r thus we can use known r that captured by camera to find gap thickness d in look-up table. The look up table of given system of glass-air-water mediums for both S and P polarization is shown in Figure 4-13.

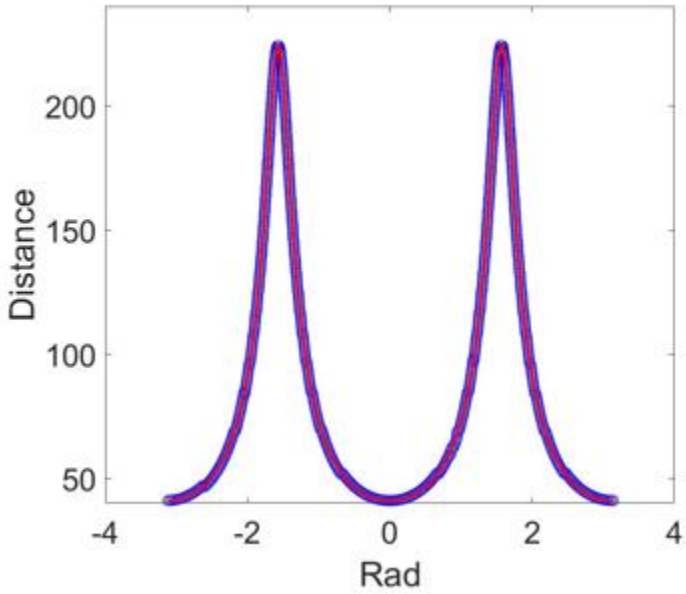

Figure 4-11: Ellipse fit for Eq.4.9.

The scale bar of Figure 4-10 can be obtained by measure the radius of water drop on prism surface and divide it by the long axis of elliptical dark area obtained by ellipse fit. The scale bar here, is also the lateral resolution of our apparatus.

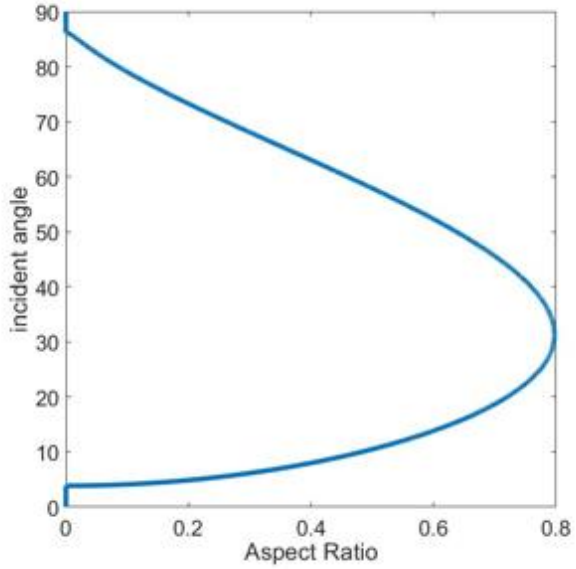

Figure 4-12: Aspect ratio vs incident angle, the table could be directly used to match incident angle with known aspect ratio.

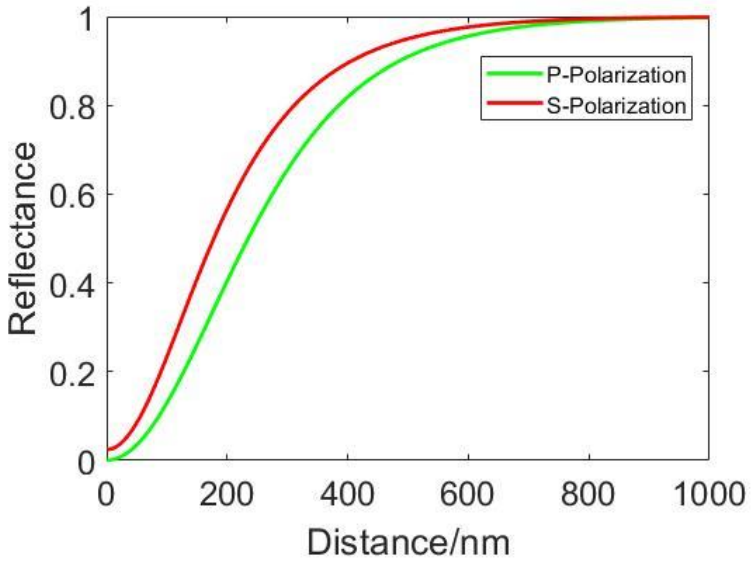

Figure 4-13: Look-up table for given system of glass-air-water at $\theta_i = 45°$.

4.4 SETUP CALIBRATION WITH HERTZIAN CONTACT

After explaining the data acquisition including fixing distortion D, obtaining incident angle θ_i, and converting total reflectance into gap thickness d. Now we are going to verify our theoretical design with well-established Hertzian contact theory. As we discussed earlier in this thesis, for an elastic sphere in contact with a smooth flat surface, the contact area can be described by Eq.3.13, and the gap thickness between two objects along the radial distance can be expressed by Eq.3.15. To achieve Hertzian contact, a glass convex lens (LA1608, radius of curvature $R = 386\ mm$) is placed on the prism surface as shown in Figure 4-14, this makes three mediums of FTIR become glass-air-glass that satisfy $n_1 = n_3 > n_2$. Hence this system is qualified to measure the thickness air medium between convex lens and prism surface to compare with Eq.3.15 of Hertzian contact theory.

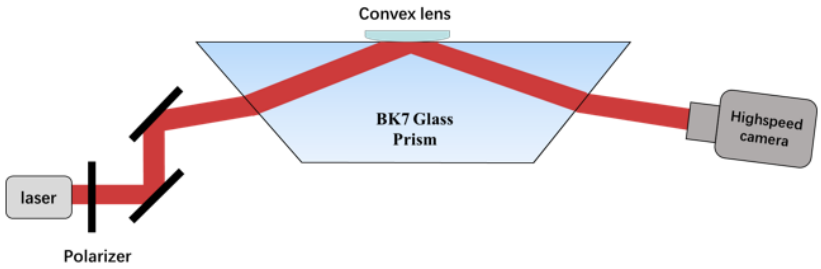

Figure 4-14: Convex lens is placed on prism surface to be used for calibration.

Since a new system is built, accompanied look-up table for both P and S polarization is generated for glass-air glass system is shown in Figure 4-15.

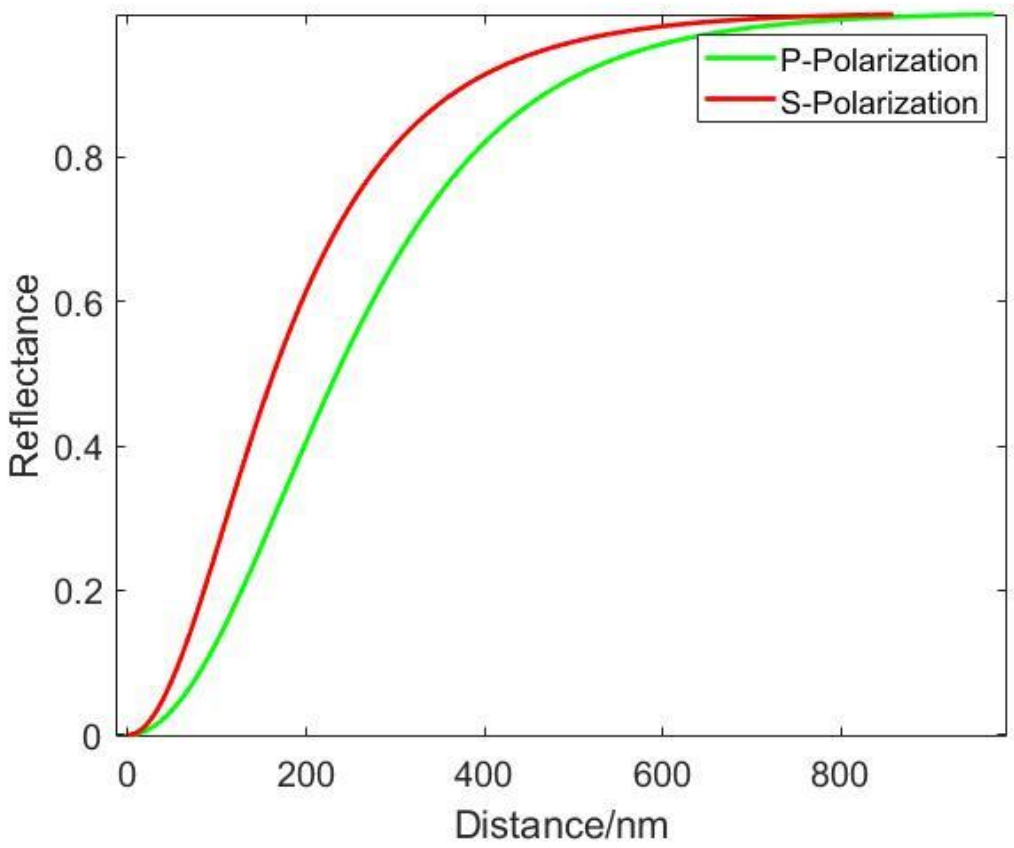

Figure 4-15: Look-up table for given system of glass-air-glass at $\theta_i = 45°$.

Experimental data obtained from high-speed camera after dividing background image is shown in Figure 4-16.2, after fixing the distortion obtained from water droplet experiment, a circular contact area is observed as shown in Figure 4-16.4. And the center of contact can be obtained via ImageJ or 3D quadratic surface fit as shown in Figure 4-16.3. As we can see from the image, center of contact is dark, but the color is fading away from the center of contact, which means the gap thickness is getting larger, till the

color is completely white representing the surface of convex lens is too far to frustrate the total internal reflection at the interface.

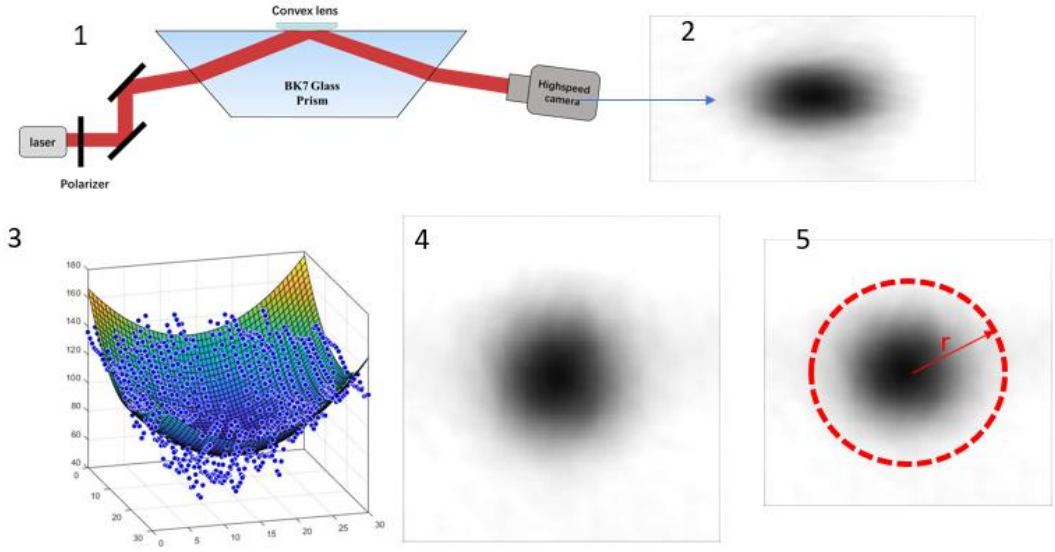

Figure 4-16: Raw data processing for convex lens contact with prism surface. (1) Experiment setup. (2) Normalized image before fixing distortion. (3) 3D quadratic fit to find contact center. (4) Normalized image after fixing distortion. (5) Step of averaging reflectance along the radial distance away from center of contact.

The next step of data processing is average reflectance along the radial distance from the center of contact as shown in Figure 4-16.5. Then use look-up table showed in Figure 4-15 to convert reflectance into gap thickness and plot gap thickness d verse radial distance x. The shape of plot matched with Hertzian contact theory excellent as shown in Figure 4-17.

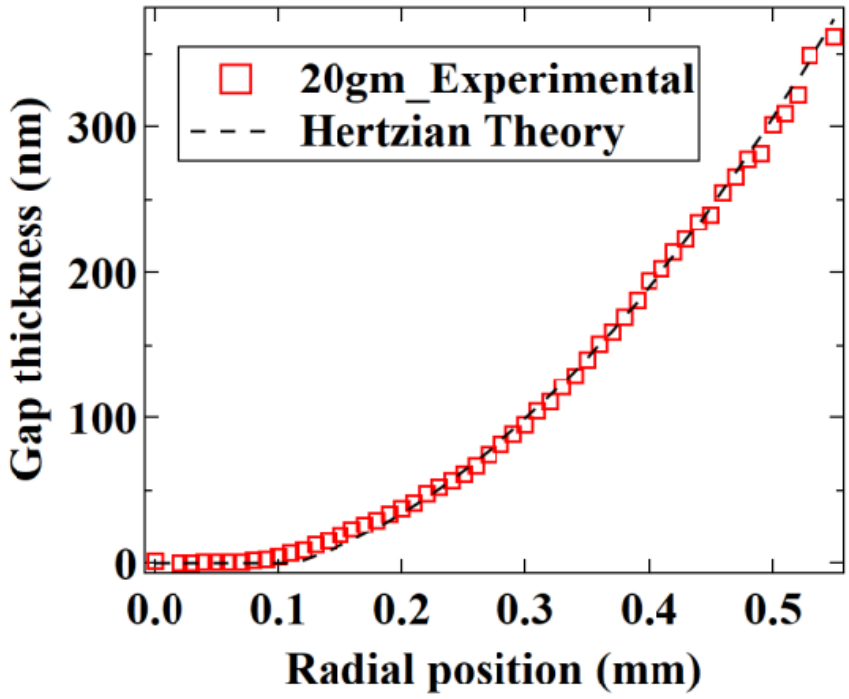

Figure 4-17: Height profile of convex lens LA1608 with 20 grams of applied load, the measured height matched with Hertzian theory very well.

Furthermore, we applied different weights on convex lens to increase contact area and measured the height profiles (gap thickness between lens and flat surface) to compare with Hertzian contact theory with changing of applied load.

As shown in Figure 4-18, different loads were applied on the top of convex to achieve Hertzian contact, measured height profiles agreed with Hertzian contact theory very well, which means our technique is a reliable technique for measuring thickness of nanoscopic thin gap between two contact objects with very high lateral resolution (pixel to pixel distance is around 3 μm depends on camera sensor) and very accurate of vertical resolution (around $10nm$).

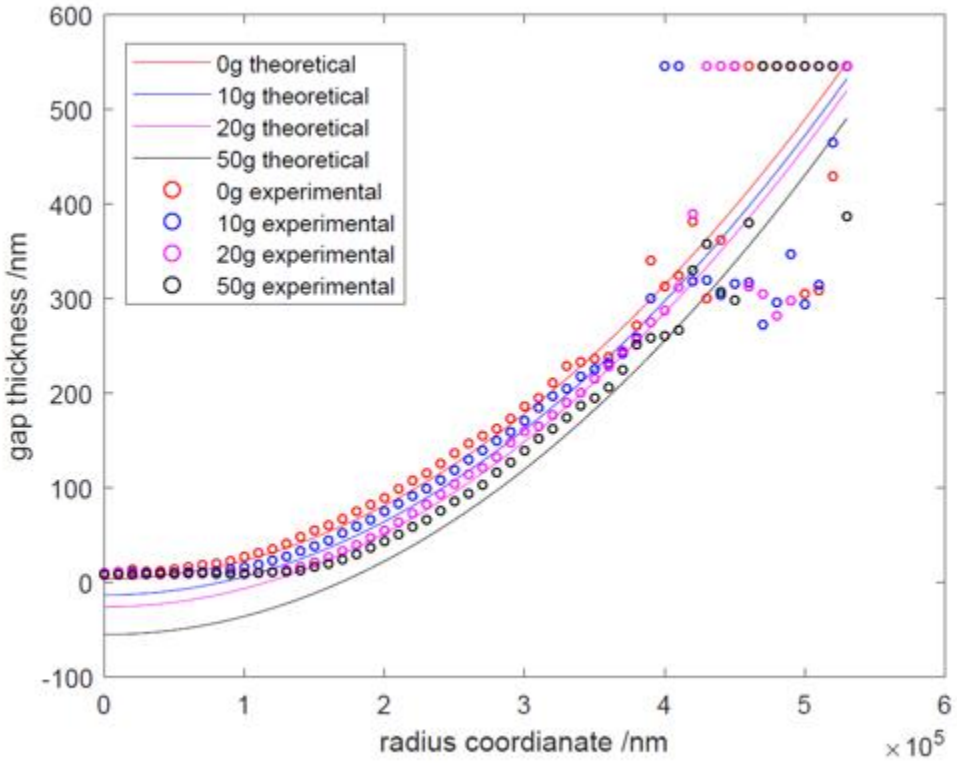

Figure 4-18: Elastic deformations of convex lens with external applied loads. Circular points represent measured heights, solid lines represent Hertzian predictions.

4.5 POLYMER THIN FILM MEASUREMENT

After verifying our technique is capable of measuring gap thickness between convex lens and flat smooth prism surface. As we discussed earlier in Figure 4-6, if a given system composed of three mediums with refractive indices satisfies $n_1 > n_3 > n_2$. Then the thickness of the second medium n_2 can be measured. Based on requirement, we

investigated our apparatus to measure the thickness of thin Polydimethylsiloxane (PDMS) films.

In this system, first medium is glass with refractive index $n_1 = 1.52$, the second medium is PDMS with refractive index $n_2 = 1.43$, for third medium we need choose a liquid that can make intimate contact with PDMS surface but can not diffuse into PDMS, the Cinnamaldehyde with refractive index $n_1 = 1.62$ is chosen. Consequently, the incident angle should be greater than the critical angle of glass-PDMS interface $\theta_C = 70.2$, the corresponding reflectance to gap thickness look up table is shown in Figure 4-19.

The PDMS base (Sylgard 184 Silicone Elastomer Kit from Dow) was mixed with crosslinker at a fixed ratio 10:1 and dissolved into Chloroform ($CHCl_3$) to achieve different concentrations (1%~5%). PDMS solutions were then applied on $25 \times 25\ mm^2$ glass slide that attached to spin coater, and span at 2000 rpm for 30 seconds. After spin coating, all glass slides with coated PDMS films were sealed into glass petri dish and put into oven curing for 3 days at 60°.

After curing, glass slide with film is placed on prism surface gently with index match oil (Immersion Oil Type N, Nikon) trapped in between to make glass slide and prism become same phase. A layer of Cinnamaldehyde is then applied on top of PDMS film as shown in Figure 4-20.

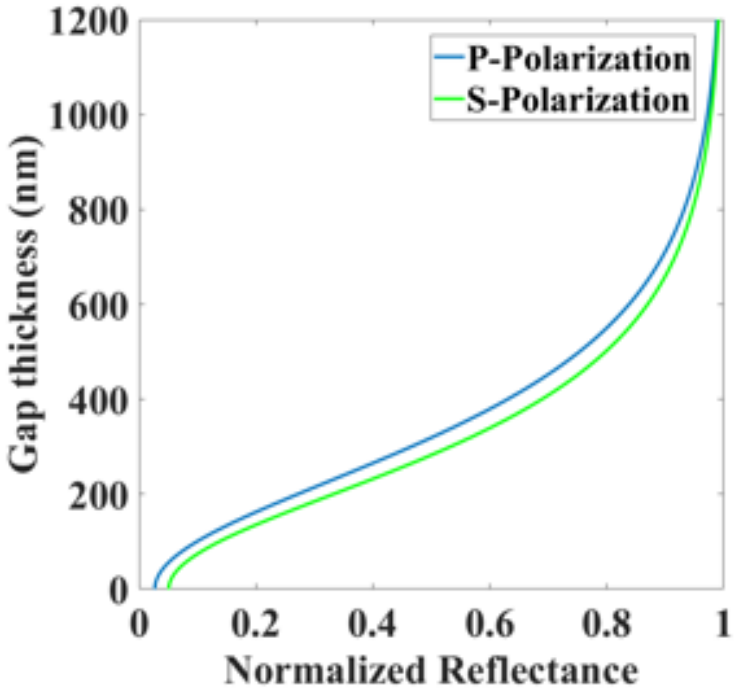

Figure 4-19: Look up table for glass-PDMS-Cinnamaldehyde system at incident angle $\theta_i = 75°$.

The incident angle calculation and data processing are same as we discussed in earlier section. Normalization setup was performed via dividing the images obtained from high-speed camera by a background image. Normalized images were then converted into height profile which is the thickness of thin film.

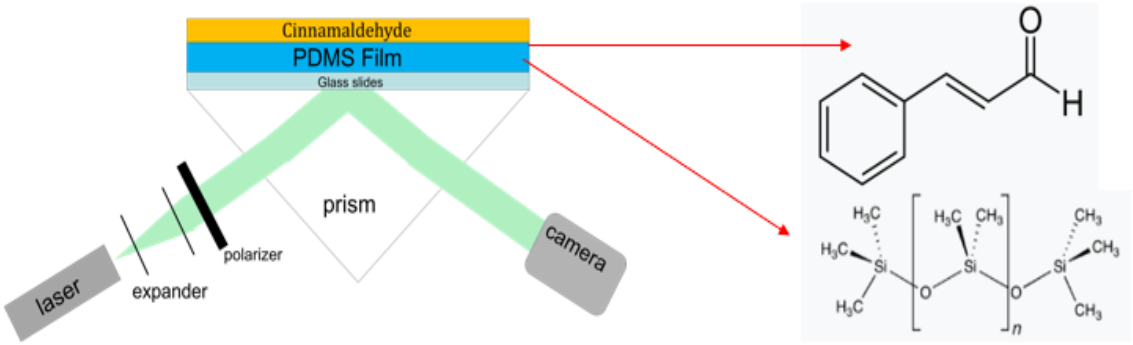

Figure 4-20: Experiment system of glass-PDMS-Cinnamaldehyde and their structures.

As shown in Figure 4-21.2, the thickness of PDMS film isn't changing as time goes, which means the Cinnamaldehyde oil wouldn't penetrate into PDMS film. Furthermore, this method could also be used to visualize the large-scale surface topography as shown in Figure 4-21.1, small bumps are directly visualized. Note that those bumps are caused by multiple reasons such as large-scale roughness on the surface and thermal fluctuations of camera sensor. Detailed analysis could by performed by involving techniques such as AFM, ellipsometer and profilometer. It is impossible to use FTIR to investigate nanoscale roughness of surface due to limitations of lateral resolution of camera sensor and wavelength of light source.

The theory of FTIR to measure thickness of thin film is very close to the theory of ellipsometry. Both are using same Eq.4.7 to calculate thickness but in our FTIR apparatus, we are directly measuring change of intensity, while ellipsometry is measuring change of polarization of light. This main difference makes FTIR less sensitive than ellipsometry in terms of thickness measurement, but FTIR can measure large area of thin film and can visualize large-scale topography films.

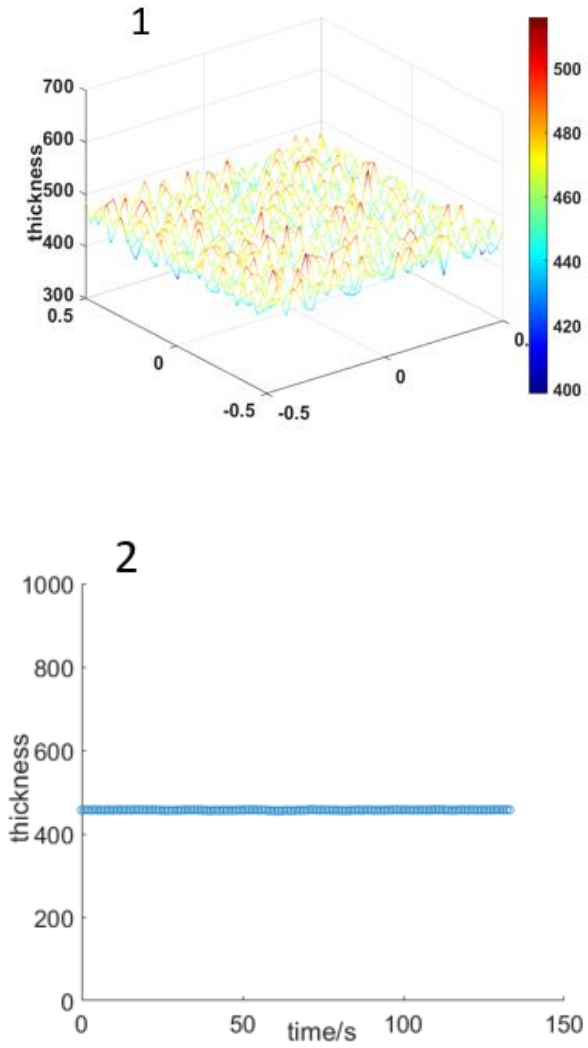

Figure 4-21: Thickness of PDMS film measured by FTIR. (1) Surface topography of thin PDMS film. (2) Thickness of PDMS verse time.

In this chapter, we have discussed theory of frustrated total internal reflection in depth and. showed step by step procedure of incident angle calculation, image processing to convert reflectance to gap thickness. And validated our apparatus via Hertzian contact

theory. Furthermore, we have explored FTIR to thin polymer film characterization such as surface topography and thickness measurement. Moreover, we discussed the difference between FTIR and Ellipsometry, and their own advantages

Overall, FTIR is a robust technique that can be used to measure thickness of thin polymer films and gap between two contact objects.

CHAPTER V

ATTRACTIVE FORCES SLOW CONTACT FORMATION BETWEEN DEFORMABLE DOIDES UNDERWATER

From wet tire traction to underwater adhesion, the evacuation of a thin layer of water between two surfaces is essential for contact formation and subsequent interactions [54-45]. Elegant examples in nature use many different strategies to adhere and grip strongly. For example, biological adhesive systems such as mussel foot protein have demonstrated the need to displace interfacial water and the role of hydrophobicity in achieving high underwater adhesion [57-59].

On the other hand, spider silk uses hygroscopic compounds in aggregate glues to get rid of interfacial water and hence hunt in wet habitats [60]. Apart from solely chemistry-based solutions, nature has also employed surface patterning to remove interfacial water and, hence, achieve high underwater adhesion and friction, for example in the case of tree-frogs and geckos [61-64]. They rely on weaker van der Waals interactions and water evacuation to create a dry adhesive contact. Additionally for tree-frogs, one finds features such as patterned toepads that have channels designed to collect the water during the attachment cycle and keep the contact interface dry [65], reminiscent of tire tread patterns that help drain the water during rolling on wet surfaces.\ Despite its ubiquity in biological and everyday phenomena, a practical understanding of the

dynamics of evacuating fluid between a soft elastomer and a solid surface during and after collision remains elusive due to the complex interplay between adhesion lubrication forces, solvation forces, roughness and material mechanics [66-68]. Initial steps toward the problem were undertaken eight decades ago by Eirich and Tabor [69]. Their simple hydrodynamic calculations show that the pressure mediated by a viscous liquid, between metal surfaces brought into contact can be large enough to cause first elastic, and then plastic deformation. Subsequent work demonstrated that elastohydrodynamic forces also cause an increase in the liquid's viscosity [70]. For contacting pairs where one of the surfaces is soft, the large film pressures are not observed, and the liquids entrapped can be considered isoviscous. This case was first studied by Roberts and Tabor in which an optically smooth rubber surface approaching a glass substrate was found to deform elastically before contact and entrap the liquid, resulting in a bell-shaped elastic deformation. The evacuation process of the entrapped liquid was studied using optical interferometry and a liquid of sufficiently high viscosity was chosen to slow down the evacuation rates so that it could be captured as a function of time. The equilibrium film thicknesses (~ 20 nm) for water were influenced by double-layer forces and a function of electrolyte solution. The evacuation dynamics were then analyzed to estimate the viscosities of the solutions using the squeeze-film equation by Reynolds [71]. For the case of distilled water entrapment, Roberts and Tabor highlighted that the Reynolds equation was not applicable due to collapse of thin film and entrapping of water pockets. Later, Davis et al. elegantly integrated the lubrication forces and linear elasticity to formulate the collision theory for soft elastic spheres in a fluid [72].

Several studies have extended the elastohydrodynamic theory to systems in which the soft surface is an elastic film supported by a hard substrate [73-75]. There, a significant amount of stress is transferred to the underlying substrate resulting in a higher effective elastic modulus and this reduces the elastohydrodynamic response in comparison to that observed for the elastic-half space made of the same material. Frechette et al. measured the deformation and hydrodynamic forces simultaneously to explain the role of elastic forces on hydrodynamic interactions and hence provided insights into the dynamics of contact formation due to the release of stored elastic energy [76]. They also disentangled the contribution of elastic compliance and surface roughness to elastohydrodynamic deformation by comparing the measured film thicknesses with those predicted from lubrication theory [77]. The advancement in elastohydrodynamic theory has provided a central understanding about the initial state (before any contact) of systems critical to soft coatings for tribology, adhesives and biomaterials. However, desired end properties such as underwater adhesion or friction between soft-hard contacting pairs require the evacuation of trapped water for intimate solid-solid contact, and this condition is still difficult to comment upon without a detailed understanding of the processes following the initial deformation, especially when long-range, adhesive interactions are not negligible.

In this chapter, I report the evolution of underwater contact between a soft elastomeric lens and hard surface of variable surface energy by visualizing the initial contact formation and measuring the evolution of the entrapped liquid film over time. I determine the dependence of fluid evacuation on the surface wettability and elastomer modulus in the underwater collision as it is essential to any observed transient and final

adhesion and friction state. Our results have implications for problems in which the timescale of wet contact is relevant: from tire traction on wet roads to design of underwater adhesives and lubricants to understanding biological solutions for wet traction and adhesion.

5.1 MATERIALS AND METHODS

5.1.1 SYNTHESIS OF SMOOTH ELASTIC POLYDIMETHSILOXNAE LENSES

Soft and smooth elastomeric lenses of varying modulus were synthesized by cross-linking PDMS. A desired range of moduli was achieved by changing the cross-link molecular weight (M_c) of the monomers in accordance with the network theory, which states that the elastic modulus of a perfectly cross-linked system is inversely proportional to M_c and can be estimated using the relation, $E \cong \rho RT/M_c$. where ρ is the density of the polymer, R is the gas constant, T is absolute temperature, and M_c is the cross-link molecular weight. Vinyl-terminated PDMS of three different molecular weights (M_w) (DMS V-05 [Mw = 800 g/mol], V-31 [Mw = 28,000 g/mol] and V-41 [Mw=62,700 g/mol]) as monomers, tetrakis-dimethylsiloxysilane as tetra-functional cross-linker and platinum carbonyl cyclo-vinyl methyl siloxane as catalyst were procured from Gelest Inc. Monomer and cross-linker were first mixed in a molar ratio of 4.4 in an aluminum pan, then the catalyst was added as 0.1 wt% of the total mixture and finally the batch was transferred to a syringe with a needle for casting. Before casting the lenses, the syringe was place in a vacuum chamber for 5 mins to remove all the air bubbles entrapped while physical mixing. As the process of mixing and vacuum application for

air bubble removal is prone to cross-linker evaporation, the initial ratio of monomer:cross-linker was set higher than the required stoichiometric ratio for reaction. Previously, this methodology has proved to avoid the cross-linker evaporation below stoichiometric ratio and, hence, minimize the adhesion hysteresis due to viscose-dissipation of the unreacted groups in the network [81-82].

Lenses for JKR measurements and FTIR experiments were casted on fluorinated glass petri-dishes. Fluorinated dishes were used as it has surface energy lower than PDMS, hence, the PDMS mixture drop maintains a hemispherical shape. The dishes were sealed with glass lid and were cured at 60° C for 3 d. Further, the lenses were transferred to cellulose extraction thimble for Soxhlet extraction where toluene refluxes at 130° C for 48 h. PDMS lenses were again transferred to a fluorinated dish and dried in air for 12 h.

Finally, the lenses were vacuum dried at 120° C for 16 h and then used for experiments. The radius of curvature was measured by fitting a 3-point circle to the image obtained using an optical microscope (Olympus). Lenses with curvatures below the capillary length of PDMS were selected for experiments (1.25 ± 0.05 mm for modulus and adhesion measurements through JKR framework and 1.50 ± 0.05 mm for FTIR measurements) to ensure perfect hemispherical shape. Larger lens size was used for FTIR experiments to have large contact area for visualization. The PDMS lenses of 0.7, 0.9, 1.48, 9.2 and 9.7 MPa elastic moduli were obtained (in section 3.4) in the process. The clean base-bath treated borosilicate glass petri dishes were immersed in a 0.1 wt% solution (nitrogen purged throughout) of heptadecafluoro 1,1,2,2 tetrahydrodecatrichloro silane (procured from Gelest Inc.) (in toluene) for 8 h to deposit the fluorinated

monolayer. After solution treatment, the petri dishes were thoroughly rinsed with toluene, ethanol and deionized water and then dried in oven.

5.1.2 FABRICATION OF VARING WETTABILITY GLASS PRISM

Uncoated glass dove prisms (N-BK7) for FTIR experiments were procured from Edmund Optics. The received prisms were sonicated in toluene, acetone, ethanol and then deionized water for 1 h each. Prisms were blown dry with nitrogen and then plasma sterilized for 5 min to remove any sort of contaminants. One of these prisms was kept as control glass. Another cleaned prism was dipped into a 0.1 wt% OTS (procured from Gelest Inc.) (in toluene) solution for 8 h and the nitrogen was purged into the solution. The OTS-*t*-glass prism was then rinsed with copious amount of toluene to get rid of any untethered residues of OTS. The OTS-*t*-glass prism was then annealed at 120° C for 6 h to enhance ordering of hydrophobic monolayer and minimize the contact angle hysteresis. Three measurements at different spots yielded a static contact angle of $108^{\circ} \pm 3^{\circ}$ on the OTS-*t*-glass prism. To obtain prism surfaces with different wettability, the OTS-*t*-glass prism was air plasma treated for 1, 2, 3, 4 and 10 s. The contact angles obtained on those surfaces were $87.7^{\circ} \pm 0.3^{\circ}$, $51.2^{\circ} \pm 1.8^{\circ}$, $35.9^{\circ} \pm 1.0^{\circ}$, $25.4^{\circ} \pm 0.8^{\circ}$, $0^{\circ} \pm 0^{\circ}$. The long time (10 s) plasma treated prism ($0^{\circ} \pm 0^{\circ}$) and the control glass prism showed the same results for evacuation dynamics experiments. The OTS monolayer was also prepared on the silicon wafers (procured from Silicon Inc.) following the procedure reported in the literature

5.1.3 JKR CONTACT EXPERIMENT

JKR contact mechanics experiments between PDMS lenses and OTS treated surface have been performed to test viscoelastic hysteresis in the PDMS network and help determine the moduli of PDMS lenses.

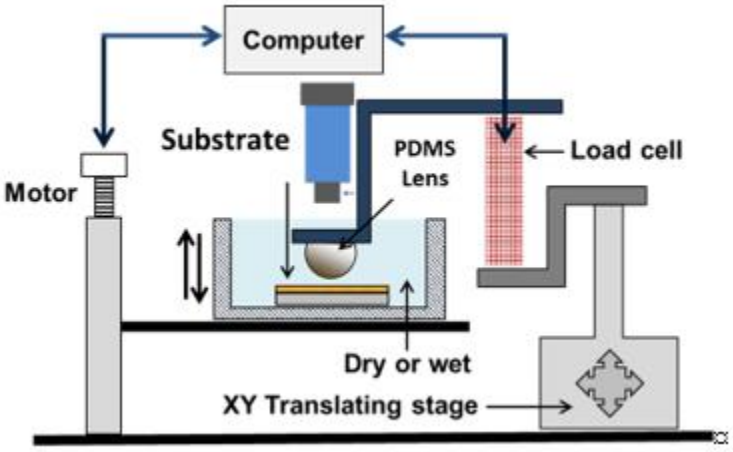

Figure 5-1: Schematic of experimental setup for in-situ force and contact area measurements. A microscope camera is used on the top of transparent glass arm holding PDMS for capturing contact area. The substrate can be kept in dry or underwater conditions. The substrate is moved up or down using a stepper motor with a pulse size of 20 nm [81].

JKR contact mechanics experiments were to extract the moduli of the synthesized PDMS lenses. The OTS silanized silicon wafer was loaded with a PDMS lens up to a maximum force of ~ 1mN and then retracted. During the process in-situ measurements of the contact radius (a) and normal force (N) was done. The experimental setup for these experiments has been shown in Figure 5-1. Data has been plotted as a^3 versus N in Figure 5-2 and fitted to Eq.3.18 (JKR model) in order to extract E^* (effective modulus)

and W (energy of adhesion). E^* depends upon the elastic modulus of the two materials and their Poisson ratio as $(1/E^* = \left(1 - \nu^2_{\text{sphere}}\right)/E_{\text{sphere}} + (1 - \nu^2_{\text{substrate}})/E_{\text{substrate}})$. As the OTS silanized silicon wafer and glass prism (for FTIR experiments) substrates are hard, the quantity $E_{\text{substrate}}$ tends to ∞. Using the Poisson's ratio for PDMS equals to 0.5 (for perfect elastic systems), elastic modulus for PDMS can be extracted. Table 4-1 show the moduli and hysteresis of the PDMS lenses used in our experiments.

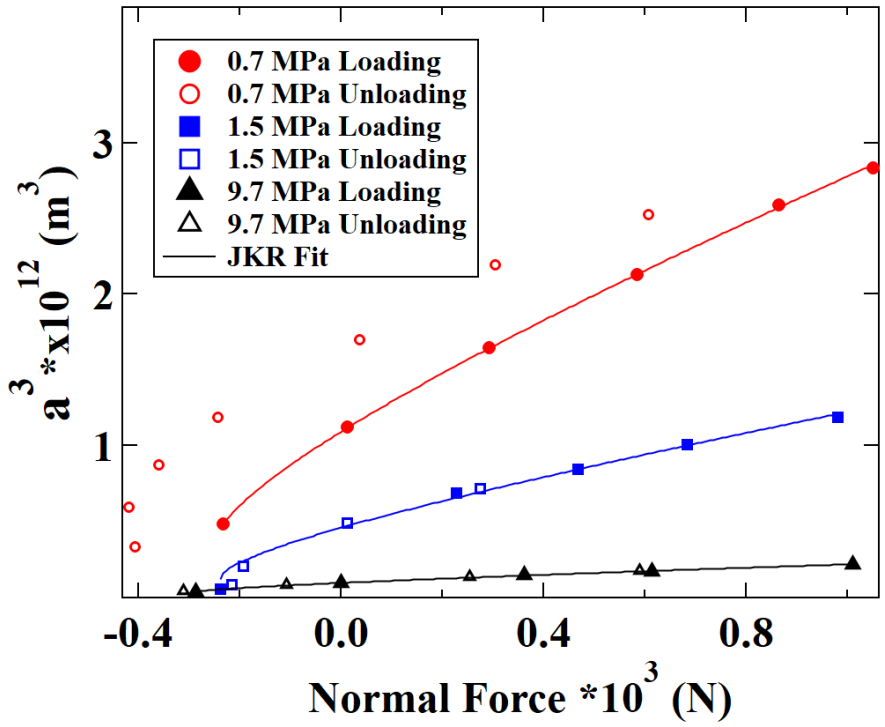

Figure 5-2: Schematic Contact radius of PDMS lens with OTS substrate, and applied normal force was measured simultaneously in loading (filled symbols) as well as unloading (hollow symbols) cycle for three moduli of lenses 0.7 (red circles), 1.5 (blue squares) and 9.7 (black triangle) MPa. The normal load versus a3 data is fitted (solid

lines) to Eq. 2.18 (JKR equation) to obtain the work of adhesion (reported in Table 4-1) and the modulus presented in the graph legend [20].

Table 5-1 Elastomer modulus (G) and work of adhesion numbers calculated using Eq.3.18 for PDMS approaching OTS coated substrate.

M_c (gm/mol)	$(W_{OTS-PDMS})_{Air}$ (approach) (mJ/m^2)	Elastic Modulus (MPa)	$(W_{OTS-PDMS})_{Air}$ (retraction) (mJ/m^2)
800	50.4 ± 1.2	9.7 ± 0.0	55.4 ± 0.6
6000	42.2 ± 2.3	1.5 ± 0.0	42.4 ± 3.0
62700	44.2 ± 1.0	0.7 ± 0.01	69.2 ± 0.6

5.1.4 FTIR SETUP AND EXPERIMENT

A Schematic of the FTIR setup is shown in Figure 5-3.1A The top surface of the dove prism is illuminated by a polarized mounted LED (M660L4, $\lambda \sim 665$ nm, bandwidth 20 nm, obtained from Thorlabs). The dove prism glass material is transparent to the light wavelength and the prism surface is optically flat. Incident angle ($\theta_1 = 64.4^\circ \pm 0.1^\circ$) with respect to glass surface normal of the p-polarized light ($\lambda = 665$ nm) has been selected between the critical angle for glass/water and glass/PDMS interface. At FTIR condition, an evanescent wave propagates along the interface with its intensity decaying as an exponential function along the Z direction in the second medium. When a third medium

comes into the evanescent wave, a portion of the energy is refracted into the third medium. This energy loss carries the information of film thickness of the second medium. As we discussed in last chapter multiple transmissions and reflections, and also the light polarization plays a crucial role in accurate predictions of film thickness. Thus, a polarizer was used in the light path to set the p-polarization of the incident light. When a PDMS lens approaches the glass prism underwater, the FTIR phenomenon starts to occur at a separation comparable to the wavelength of light. The Z-stage is connected to the PDMS lens through a load cell to control the vertical displacement of the lens to achieve an initial load of (7 ± 0.2) g after which the motor is stopped.

The reflected intensity profiles from the dove prism were collected using a high-speed camera (VEO410 procured from Phantom) with a video resolution of 128´128 pixels^2 at 24 and 1000 fps. The fast frame rate (1000 fps) was good enough to visualize the initial contact formation whereas the slow frame rate (24 fps) allowed us to capture long time videos for studying water evacuation dynamics from the hydrophobic-hydrophobic entrapment. Figure 5-3B (left image) shows a raw grayscale frame of a video which shows both, the region of dry contact or dark pixels, i.e. PDMS in contact with the hard substrate, as well as the bright pixels which corresponds to the case of a thin water film in between the PDMS and substrate. Before performing the experiments, a water droplet is put on the top of a dry hydrophobic prism which gives a perfectly circular boundary line for the droplet and the image is captured. The captured image is elliptical and used for calculating the aspect ratio for back transformation of the acquired data and the incident angle. A transformed frame of a video was then divided by the background image (frame with total internal reflection of the light at every pixel or t = 0

image) of that video. The normalized intensity at each pixel (reflectance) was then converted into corresponding water film thicknesses (h) using a Look-Up Table for p-polarization presented in Figure. 4-4 to render a 3D height map. The Look-Up was created using the relationship between normalized reflection intensity (reflectance, $|\hat{r}|^2$) and the film thickness. This reflectance equation (Eq. 3.7) accounts for multiple reflections and transmission summed (geometric series) using Stokes' relations and for light polarization through Fresnel equation and has been reported in detail earlier. The lateral resolution of the camera is ~ 15 μm/pixel. To verify the FTIR technique and our analysis protocol, I measure (Figure 5-5) the air film thickness between a convex glass lens (radius of curvature: 386 mm, obtained from Thorlabs) and glass prisms (pristine and OTS coated) under a 20g load. The measured gap thicknesses showed an excellent agreement with the Hertzian contact theory.

The total reflected amplitude ($\hat{r}$) is related to indices of refraction of glass (n_1), water (n_2) and PDMS (n_3). θ_1, θ_2, and θ_3 denotes the incident angles for glass/water, water/PDMS and PDMS/water interface. j is an imaginary number and h is the gap or water film thickness between prism and PDMS lens.

5.2 PRINCIPLES OF EXPERIMENT

3D imaging of the contact made between a soft elastomer and hard substrate underwater was achieved using the principle of frustrated total internal reflection (FTIR). Figure 5-3A shows a sketch of the experimental setup where a BK7 glass (refractive index $n_1 = 1.52$) prism has the top surface enclosed in a polytetrafluoroethylene chamber filled with water ($n_2 = 1.33$). The polydimethylsiloxane (PDMS, $n_3 = 1.43$)

was selected as an elastomer because of several reasons. The PDMS has a negligible swelling ratio in water, which ensures constant material properties and reduces the possibility of absorption of any water throughout the observed process [78]. The PDMS elastomeric network is fully crosslinked and does not contain any nanoparticles for reinforcement.

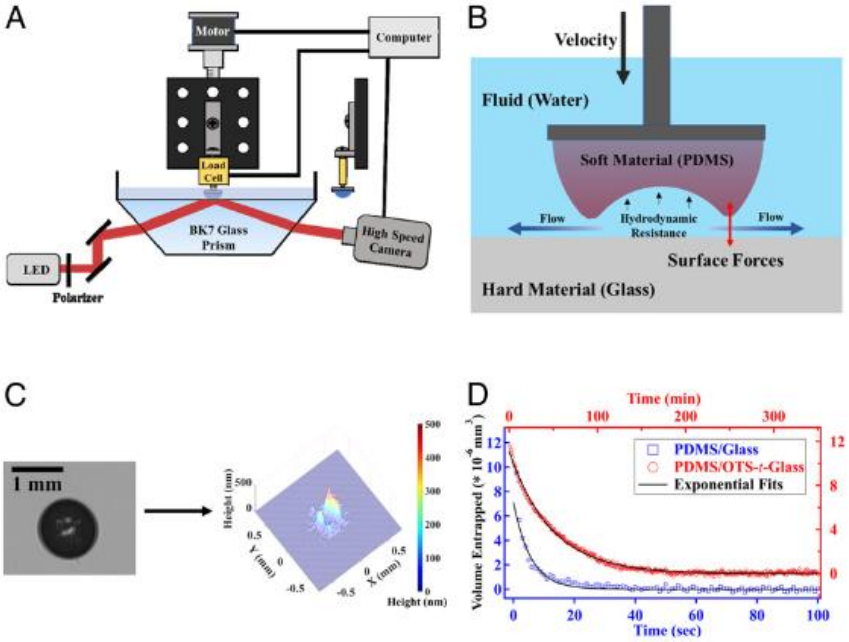

Figure 5-3: Schematic (not to scale) of (A) the frustrated total internal reflection imaging setup and (B) the out-of-contact elastohydrodynamic deformation with labeled relevant phenomena. (C) Backward transformed (using the ellipse's aspect ratio) FTIR image (left image) for a PDMS elastomer/hard substrate (51° water contact angle) contact underwater. Right image shows the height map (side view) calculated by normalizing the gray-scale image (left image) with background and conversion to corresponding heights using reflectance equation (chapter 3). (D) Volume entrapped versus time data for

PDMS/glass (empty blue squares) and PDMS/OTS-t-Glass contact (empty red circles) and the corresponding exponential fits (solid black lines) to extract the decay constant. Volumes are calculated by integrating the height maps at every time step [20].

Additionally, the PDMS lenses (blue hemisphere in Figure. 4-3A) used were all Soxhlet extracted for three days before use to ensure the removal of uncross-linked chains which can potentially change the viscosity and wetting of entrapped water, hence the evacuation dynamics. The PDMS lens is brought into contact with the glass substrate with a translational Z-stage connected to a stepper motor, at a constant approach velocity sufficient to cause elastohydrodynamic deformation of the elastomer (0.9 mm/sec). Images are captured by a high-speed camera at different frame rates based on the time span of the process studied. Fig. 4-3B shows the schematic of phenomena at the contact interface before the contact between an elastomer and a hard surface. The hydrodynamic resistance causes the elastic deformation to the elastomer and surface forces might play a role in evacuation of liquid when the two surfaces are in close proximities. We explored the parameter space encompassing three moduli (0.7, 1.5 and 9.7 MPa) for soft PDMS lenses and six substrates with water contact angles in air ranging from 0° to 108°. The PDMS lenses of variable elastic modulus were synthesized by employing network theory [79]. Evolution of contact area of the lenses while pressed against a low surface energy (~ 24 mJ/m2) monolayer (octadecyltrichlorosilane (OTS) treated silicon wafer) was analyzed to extract the modulus using the JKR model. To prepare substrates with varying contact angles, an OTS monolayer was solution deposited on a glass prism following the procedure described in the literature [80]. The static water contact angle on OTS-t-glass

prism is measured as 108° ± 3° (3 repeats at different spots). Lower contact angles (87.7°± 0.3°, 51.2°± 1.8°, 35.9°± 1.0°, 25.4° ± 0.8°, 0° ± 0°) were achieved by plasma treating the OTS-t-glass prism for different exposure times. The methodology for surface preparation and resulting surface chemistry (evaluated by X-ray photoelectron spectroscopy and attenuated total internal infrared spectroscopy) has been described in great details elsewhere.

Figure 5-3C shows the transformed FTIR image (at t = 1.5 sec) for PDMS/intermediate wettability glass (with water contact angle of 51° ± 1.8°) contact under water. The dark region represents the pixels for which the evanescent wave is totally frustrated due to contact of PDMS with the substrate, resulting in refraction of incident light into PDMS, whereas the white region represents pixels where the wave is partially frustrated due to presence of entrapped water. The captured image is elliptical due to optical light path and back transformed using aspect ratio of ellipse to perform analysis. A look-up table (Figure 5-4) between the modulus of total reflectivity squared (reflectance) versus film thickness was prepared using the Stokes' relations and Fresnel equations for p-polarization, which was then used to convert the reflectance of every pixel to the height of water entrapped. Any pixel with water film thickness less than 3 nm is considered as contact due to the limit in resolution for this technique. Further, Figure 5-3C shows the side view of the heightmap corresponding to the gray-scale image. The obtained spatiotemporal (height maps at each time step) data is used for calculating the volume of entrapped water by integrating the height maps at each timestep, represented in Figure 5-3D.

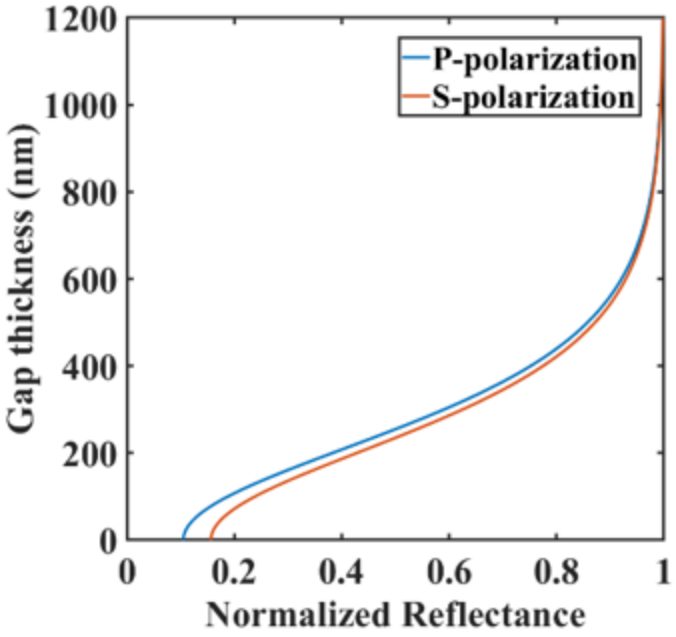

Figure 5-4: Normalized reflectance as a function of gap thickness, also called Look-Up Table, used for conversion of reflectance to water film thickness. The parameters for Fresnel factors are, $n_1 = 1.52$ (glass), $n_2 = 1.33$ (water), $n_3 = 1.43$ (PDMS) and angle of incidence is $64.4^{\circ} \pm 0.1.^{\circ}$

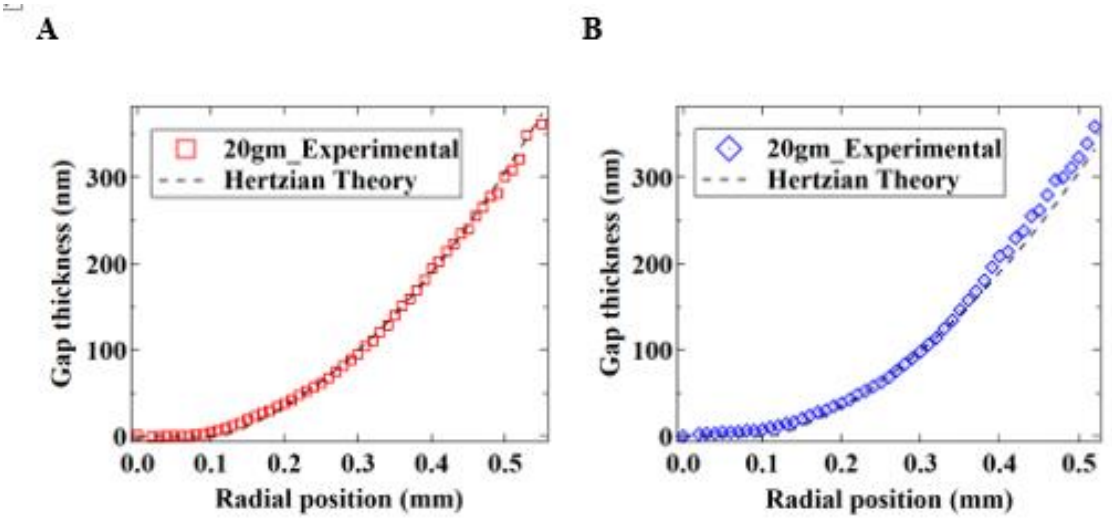

Figure 5-5: Measured air film thickness for a glass lens/glass prism (hollow red square) (A) and glass lens/OTS-t-glass prism (hollow blue diamond) (B) contact for an external applied load of 20 gm. The corresponding predictions by Hertzian theory are represented by the dashed black line in each graph. The radius of curvature for the glass lens is 386 mm [20].

5.3 DYNAMICS OF WATER EVACUATION

Figure 5-3D shows the water evacuation profiles for two extreme cases of wettability, i.e., PDMS/glass and PDMS/OTS-*t*-glass contact underwater. The volume of entrapped water was observed to decrease exponentially with time after initial contact irrespective of the substrate chemistry and the PDMS elastic modulus (G). The decay constants (K) for different cases were obtained by fitting the volume versus time data to the equation, $V(t) = V_0 e^{-Kt}$, and the results are shown in Figure 5-6. In Figure 5-3D, it can be noted that the time required to evacuate water from a hydrophobic-hydrophobic entrapment is ~ 3 orders of magnitude higher than that required for the hydrophilic-hydrophobic entrapment. The results are surprising as we expected that the water evacuation would be faster from two hydrophobic surfaces entrapment due to their thermodynamic inclination to be in contact. We expect the contact between two hydrophobic surfaces underwater to be dry based on earlier measurements using surface-sensitive sum-frequency generation spectroscopy (SFG) and the measured work of adhesion (~ 80 mJ/m^2 same as thermodynamic prediction) between PDMS/OTS-*t*-glass under water. In comparison, we expect the glass-hydrophobic contact should always contain a thin layer of water, which has also been verified by SFG [54].

A B

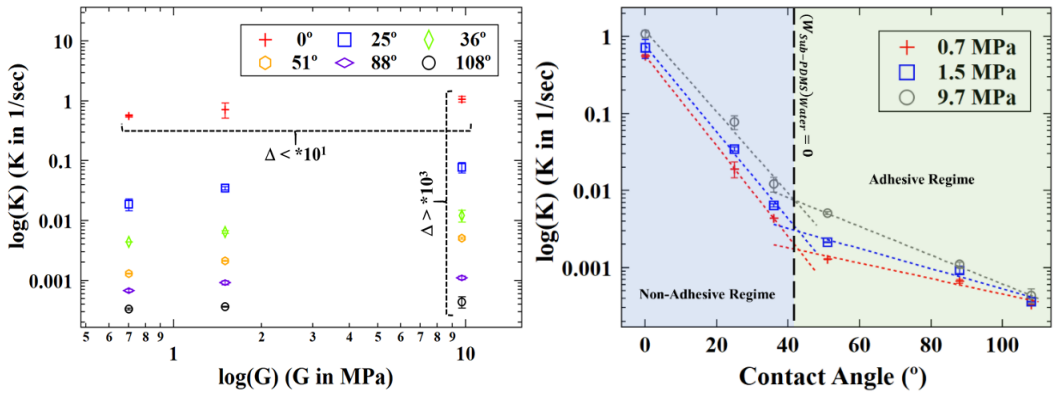

Figure 5-6: Effect of material moduli and chemistry. (A) Dependence of water evacuation rate constant on elastomer modulus (G) for different substrate wettability represented by the log-log plot. The vertical and horizontal dashed black line segments demarcate the role of substrate chemistry and modulus by comparing the change in order of magnitude in K values. (B) Log(K) versus contact angle plots for three moduli of PDMS. The plots clearly point towards a transition in evacuation dynamics as the slope of data changes about ~42°, i.e. the point at which underwater thermodynamic work of adhesion is zero (dashed vertical black line). The dashed vertical black line separates the adhesive and non-adhesive regimes. Dashed colored lines are exponential fits to K versus contact angle data for two segments about the transition point for three moduli of lenses. All the rate constants are calculated from the volume entrapped versus time data as shown in Figure 5-3D.

5.4 EFFECT OF PDMS MODULI AND SUBSTRATE WETTABILITY ON RATE CONSTANT

In Figure 5-6A, we plot the decay rates (K) for water evacuation as a function of bulk modulus (G) of PDMS for substrates with different wettability represented by water contact angles. The positive slope for all the trends represents faster evacuation for higher G. Further, the value of K increases with a decrease in substrate contact angle. It is evident from the graph that the effect of modulus (less than 1 order) is very small compared to that of surface wettability (more than 3 orders) for the parameter range explored here. Figure 5-6B shows a plot of log(K) versus contact angles for PDMS lenses with different modulus. There is a notable, apparent change in slope around ~42° contact angle (intersection of the two linear fits) for all the cases of G, indicating a transition in the mode of evacuation dynamics. The transition is also clearly visible in a log(K) versus cosine of contact angle plot (Figure 5-7). We were unable to increase the modulus of PDMS any further due to limitations in synthesis and the use of other stiffer polymers will reduce the elastohydrodynamic deformation (by 2-3 orders of magnitude for glassy polymers) and would make it difficult to monitor using FTIR [83]. For one hydrophobic surface, we explored the effect of loading velocity on initial volume entrapped (after the complete approach) and on the rate constant for a particular surface chemistry. While initial volume increases with loading velocity, this leads to no observable change in K (Figure 5-7).

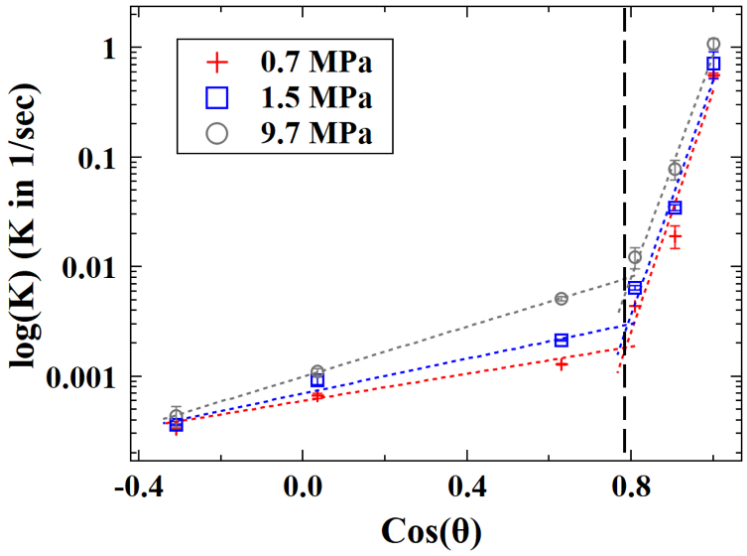

Figure 5-7: Log(K) versus cosine of substrate water contact angle for three moduli of PDMS lens showing similar transition at $Cos^{-1}(0.78)$ ($\theta \approx 38°$) as observed in Figure 5-6.

A B

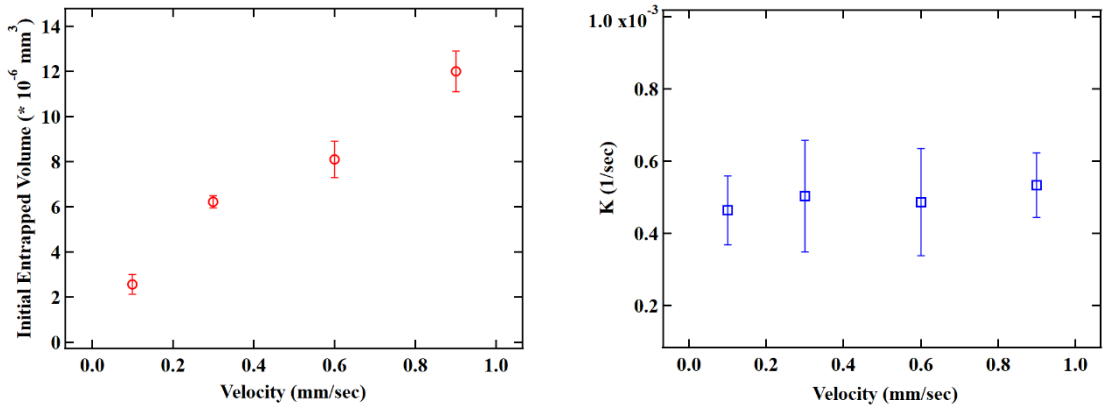

Figure 5-8: Effect of velocity on water entrapment. (A) Initial volume of water entrapped for PDMS (1.5 MPa)/hydrophobic-glass contact (water contact angle on glass ~ 100˚) as a function of approach velocity. (B) Water evacuation rate constant (K) as a function of approach velocity.

5.5 INITIAL CONTACT FORMATION AND MODES OF EVACUATION

To shed lighter on the changes in the evacuation rates Figure 5-9 shows the spatiotemporal heightmaps for initial contact formation and the following water evacuation for interfaces between PDMS lens (0.7 MPa) and three different substrates (glass (0°), intermediate glass (*i*-glass) contact angle (35.9° ± 1.0), OTS-*t*-glass (108° ± 3°)). Corresponding gray-scale images are shown under each heightmap. t = 0 is chosen arbitrarily from initial frames of each of the three cases where the elastohydrodynamic deformation can be noticed clearly.

A

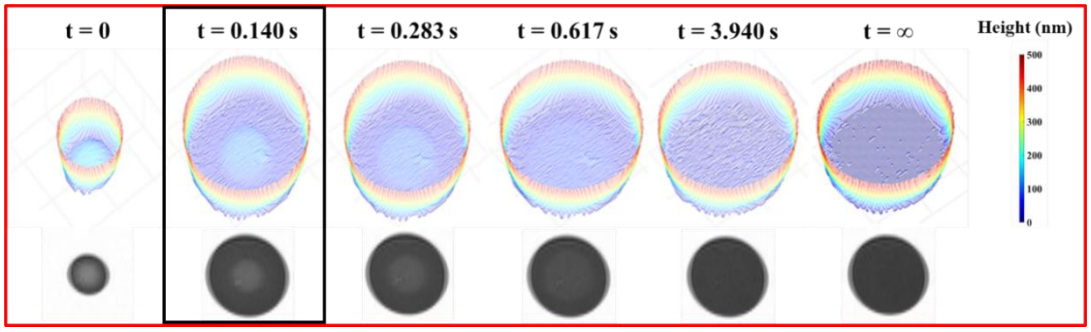

B

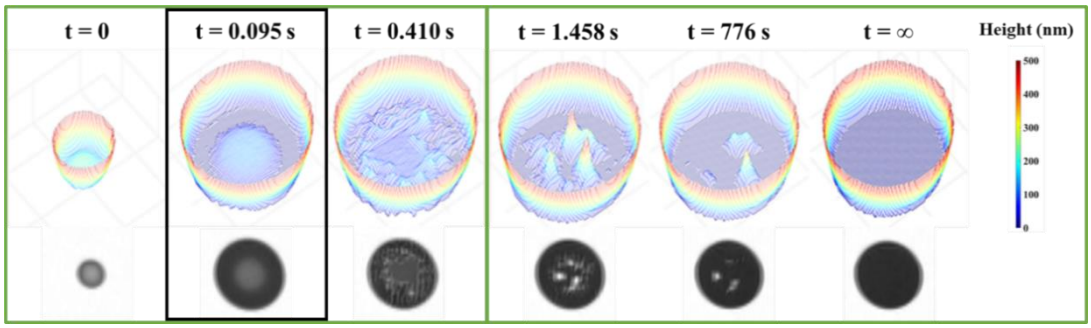

C

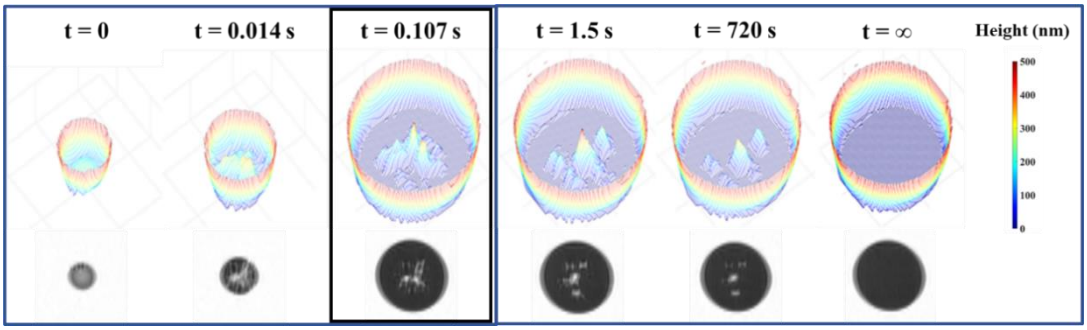

Figure 5-9: Spatiotemporal height maps and corresponding gray-scale images for PDMS/glass (red panel) (A), PDMS/intermediate contact angle (35.9°± 1.0) glass (green panel) (B) and PDMS/OTS-*t*-glass (blue panel) (C) interface. For all the cases, black outline enclosed box represents the frame where motor stopped. The left and right panel for the case (B) and (C) represent frames of two separate repeats performed at 1000 frames/sec and 24 frames/sec to capture the initial short-time deformation and contact formation and long-time water evacuation from the entrapments. For (A), all the frames belong to a single experiment performed at 24 frames/sec. The data presented is for the case with PDMS lens of 0.7 MPa (G) and the observed trends are independent to G.

Figure 5-9A shows the entrapment of water in bell shape (t = 0) and the subsequent growth of area (t = 0.14 s) outside the bell as the normal displacement progressed to reach the final normal load for the PDMS lens/glass contact underwater. A continuous thin film of water is observed throughout the apparent contact area with the additional symmetric puddle (water bell) in central position (Figure 5-9A and Figure 5-

10A). The puddle height decreases with an increase in puddle radius (t = 0.140 s to t = 3.490 s). Additionally, the 2D line heightmaps (Figure 5-10A) for the contact formation shows the gradual height decrease of thin film and the puddle without any contact between the PDMS and glass suggesting that the water evacuates axisymmetrically without any barrier in flow path. Even though the final state (t = ∞) of the contact interface seems to be completely dry, certainty of intimate atomic contact cannot be guaranteed due to limitation in the film thickness resolution (~ 3 nm) of the FTIR technique. Previously, the SFG [54] results have shown that the contact interface between hydrophobic PDMS and hydrophilic sapphire surfaces are not dry. Molecular dynamics simulations have also shown that a hydrophobic surface (contact angle > 90°) is fully hydrated even if the second contacting surface is not highly polar (contact angle < 60°). Similarly, the PDMS (hydrophobic) and glass (highly polar) contact is hindered due to the presence of a stable continuous nanometer thick film of water in between [84]. Figure 5-9C left-hand panel shows the initial (t = 0) water entrapment for the PDMS lens approaching OTS-*t*-glass underwater. Suddenly after the small puddle formation, the puddle gets asymmetrically deformed (as evident in t = 0.014 s). In fact, it is apparent from 2D cross-sections of Fig. 3C (line heightmaps, Figure 5-10B) that the symmetry of the deformed lens is broken (instability) when the peripheral gap thickness is still ~100 nm (for the case with softest lens) and, immediately after, a part of the peripheral bell appears to snap into contact. This leads to enhanced asymmetry (Figure 5-10B) and breakdown of the puddle into multiple smaller puddles (t = 0.107 s). Further, it is evident from the 2D line heightmaps (Figure 5-10B) that majority of the apparent area is true contact (in FTIR limit) between the PDMS and OTS-*t*-glass at the motor stop time.

Figure 5-9C right-hand panel illustrates the water evacuation from the small puddles entrapped between PDMS lens and OTS-*t*-glass contact where the height of individual puddles goes down with a decrease in puddle radius, in contrast with that of the PDMS/glass contact. In this case, no continuous thin film for the apparent contact is observed suggesting barriers in the water flow path.

A

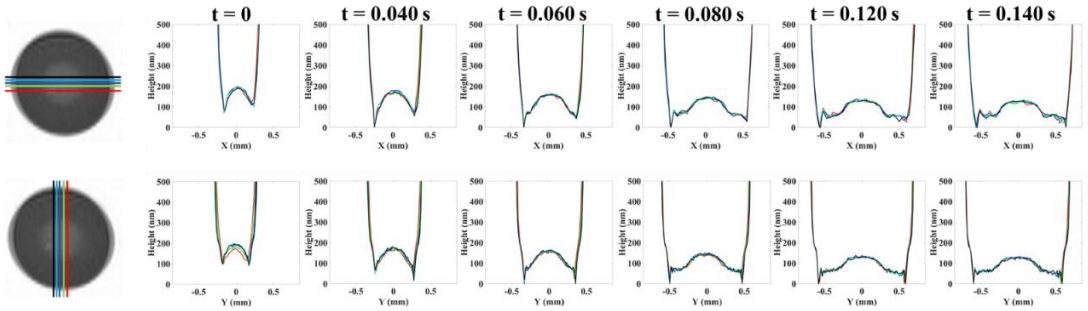

B

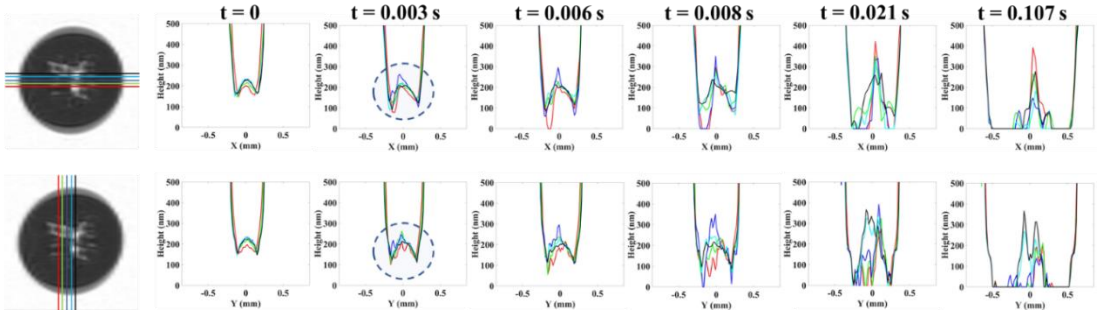

Figure 5-10: 2D line heightmaps along x and y direction for PDMS/glass (A) and PDMS/OTS-*t*-glass (B) contact. Last frame for both the cases is at the instance where the motor stopped. The dashed blue circle in part (B) highlights the instability in

elastohydrodynamic deformation. Five heightmaps along each x and y is shown for the corresponding positions marked in gray-scale images. All considered cases are around the center as the initial projected apparent area for elastohydrodynamically deformed lens is small.

Figure 5-9B shows the initial contact formation (left-hand panel) and the water evacuation (right-hand panel) from the PDMS lens/*i*-glass interface. The initial behavior of the system is similar to the PDMS/glass interface where first we observe water entrapment (t = 0) in a bell-shape due to elastohydrodynamic deformation followed by a decrease in puddle height and an increase in puddle radius (t = 0.095 s). With the reduction in puddle height, we start to observe an instability and waviness in the water film thickness with water entrapped in a combination of puddles and thin film at the center region (t = 0.410 s). We then observe that the entrapped water in combined (puddle-film) state (t = 0.410 s) further coalescing with existing puddles growing and nearby film disappearing (t = 1.458 s). Similar behavior of increment in the height of puddles is also observed in the PDMS lens/OTS-*t*-glass interface case but the process there is much faster and completed even before the motor stops. The evacuation from the smaller puddles at the PDMS lens/*i*-glass interface optically followed the mechanism of that for PDMS lens/OTS-*t*-glass interface where the heights of the puddles are found to decrease with time without the presence of a continuous thin film. Despite the similarity in the evacuation mechanism, the dynamics of evacuation from PDMS lens/*i*-glass interface is much faster than that of PDMS lens/OTS-*t*-glass interface, which further emphasizes the role of adhesion in evacuation mechanism.

5.6 HUMAN THUMB CONTACTS

To explore the generality of the observations to realistic contacts, we study the dynamics of biological underwater contacts of a human digit (thumb outermost layer: stratum corneum) with hard hydrophilic (bare glass) and hydrophobic substrates (OTS-*t*-glass) in Figure 5-12 (larger area with corresponding gray-scale images in Figure 5-11). For both the contacts, it is observed (Figure 5-11) that the protruding ridges of the thumb tend to come in contact (t = 0) with the hard substrate in an unconnected fashion. Further, the contact region evolves underwater in a two-step coalescence process (from t = 0 to t = 0.04 s and t = 0.04 onwards) similar to that reported earlier for the dry human figure-tip/glass contact [50]. The number of junction points increases (first step, t = 0 to t = 0.04 s) followed by the growth in their areas (second step, t = 0.04 onwards) resulting in the connection of those junction points into continuous ridges (result of second step). The growth is usually fast (within few seconds) and ascribed to the plasticization (reducing the elastic modulus to few MPa from ~ 1 GPa) of stratum corneum due to hydration [86,87]. The right thumb of two subjects (first authors, both male, right-handed Asian) were brought into contact at an angle of 0° with the glass prism. The glass was loaded to a constant force of 10 ± 0.5 N and was held in position for 1 minute. Three repeats were done for both the subjects. For every repeat, 15 non-overlapping areas (~ 4 mm^2) were averaged for volume and one of the repeats for one of the subjects is shown as a function of time in Figure 5-11B for clarity. The data for second subject is presented in Figure 5-12. For both the cases, t = 0 sec is defined as the time when FTIR technique starts to sense the thumb ridges. The apparent area of thumb stops changing at t = 0.1 sec. Before the experiment, the thumb of the subject was first washed with commercial soap, then

wiped with ethanol using a nonwoven paper and finally rinsed with ultrapure water (Millipore filtration system, volume resistivity of 18.2 MW.cm) for 10 seconds. This study was deemed exempt from the IRB and approved by The University of Akron.

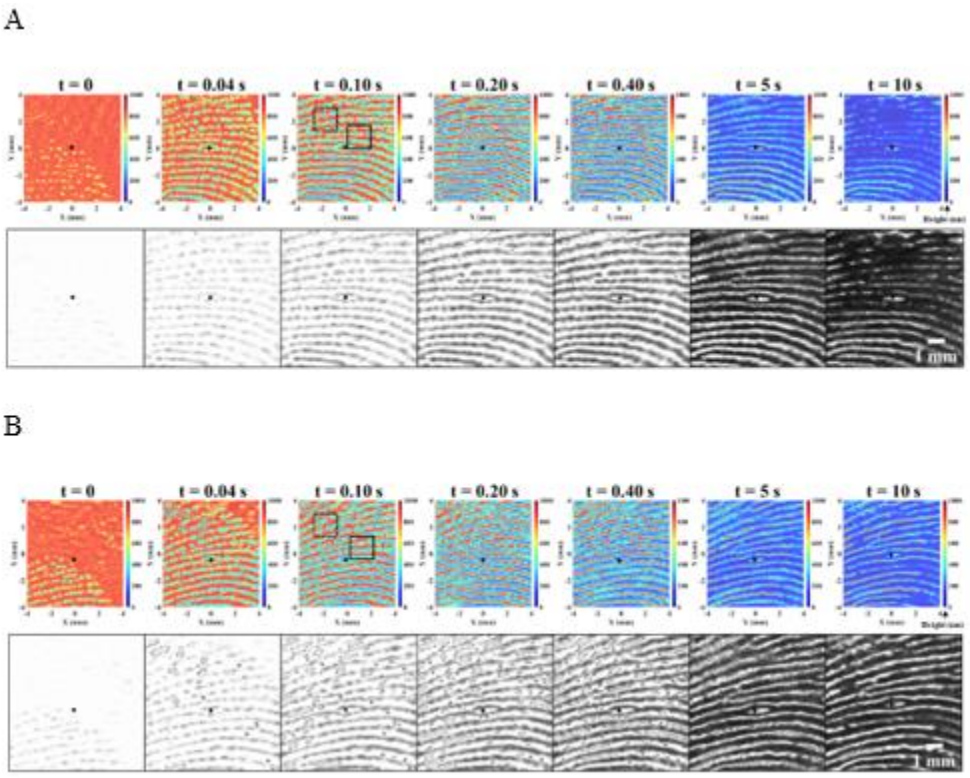

Figure 5-11: Spatiotemporal height maps and corresponding gray-scale images for a human thumb in contact with glass (A) and OTS-*t*-glass (B) capturing various events during contact formation and water evacuation. The black solid dot in all the images act as a reference point. Both the contacts are loaded with a normal force of 10 N. Some of the pixels (white region) in these height maps are saturated due to the upper limit of the FTIR technique. The black solid and dashed box at t = 0.10 s represent the region 1 and 2 used for evaluating volume versus time in Figure 5-12.

Figure 5-12 shows the evolution of water heights in a randomly selected region (for evolution of complete region see Figure 5-11) of thumb/glass and thumb/OTS-t-glass contact. It is clear from these spatiotemporal heightmaps that the thumb valleys act as channels for collection of water from the ridges (t = 0.10 s), facilitating the growth in contact area. After ridges connect (t = 0.40 s), for the case of thumb/glass interface (Figure 5-12A, top panel), we observe that the water valleys are continuous and gradually narrowed with time, enhancing the width of ridges and, hence, the contact area. Eventually some of the ridges joined due to the diminishing valleys for some regions of the thumb (t = 10 s), suggesting evacuation of water through valleys to a large extent. In the case of thumb/OTS-t-glass interface (Figure 5-12B, bottom panel), we observe an instability (t = 5 s) in the valley region following the ridges connection (t = 0.40 s) and subsequent water evacuation. There is a sudden breakdown in the continuity of flow path of the valleys resulting into unconnected entrapments of water in valleys (t = 5 s), causing evacuation of water to lesser extent. The long-time dynamics shows that the evacuation from these entrapments happen as discreet puddle-wise events. To quantify the dynamics of water evacuation, we plot the average volume versus time curves for the thumb/glass and thumb/OTS-t-glass contact in Figure 5-12B. Initially the water evacuation for both the cases follows similar dynamics with deviations starting at ~ 7 sec. Interestingly, the asymptotic volume, after the evacuation process, is much higher for the case of thumb/OTS-t-glass contact. To check for the test subject variability, we have reported the spatiotemporal heightmaps for another subject in Fig. 5.9 which shows similar features as reported above for Figure 5-12B.

A

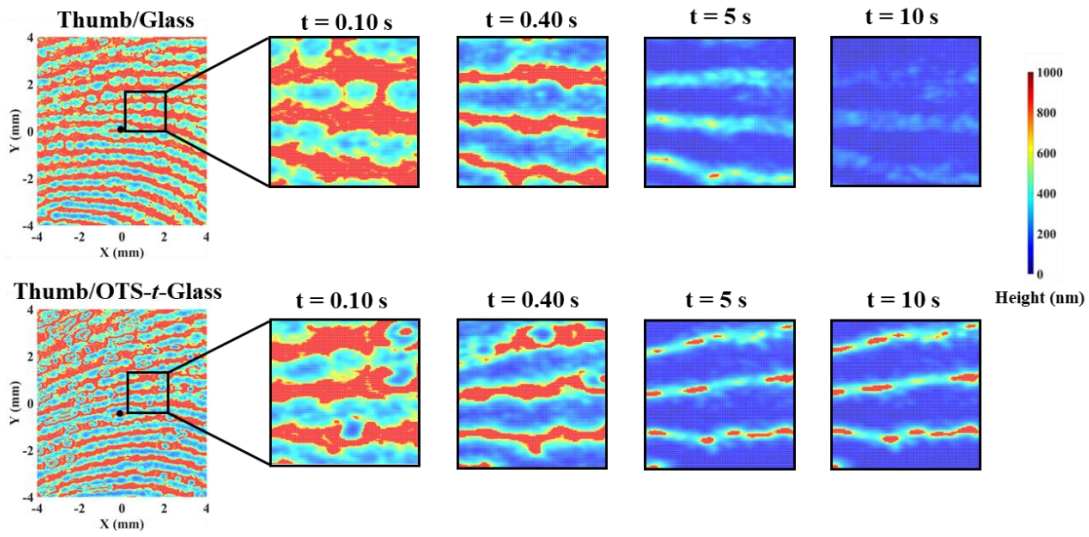

B

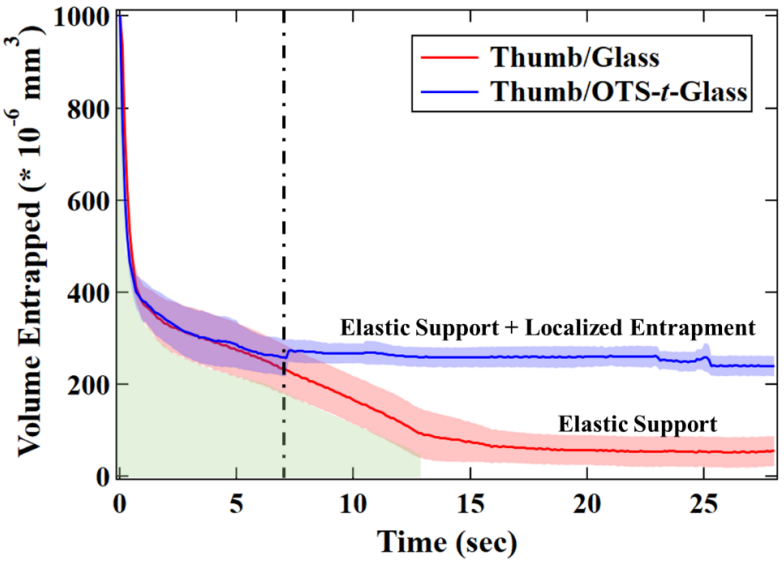

Figure 5-12: Spatiotemporal height maps for water in a localized region (marked by black solid box) for a human thumb in contact with glass (top panel) and OTS-*t*-glass (bottom panel) (A). Average (15 non-overlapping regions) volume evolution for thumb/glass (solid red line) and thumb/OTS-*t*-glass (solid blue line) contact with corresponding standard deviations (light red and blue shaded area) (B) highlighting

similarity in evacuation dynamics till ~ 7 sec (marked by vertical dashed-dotted black line) and differences in asymptotic volume for the two cases. The light green shaded region represents the water evacuation through valleys for glass case till ~ 13 sec and for OTS-*t*-glass case till ~ 7 sec. The evacuation limit for glass is reached due to elastic support of stratum corneum whereas that for OTS-*t*-glass is reached due to elastic support along with localized entrapment of water puddles shown in part A (bottom panel).

Now, we seek to understand the trends in dynamics of water evacuation and provide deeper insights into the process of contact formation, subsequent evacuation and their links with the observed rate constants (K). Figure 5-6 demarcates the role of PDMS modulus and surface wettability in the observed evacuation dynamics. The faster dynamics for higher G could be due to a lower apparent contact area at the same normal force, hence, a smaller water evacuation path. Another possibility is that the lenses with higher G cannot conform to the surface roughness which can result in wider channels for water evacuation. The significant effect of surface wettability on evacuation dynamics and the change in slope in log(K) versus water contact angle (q) around ~42° has been rationalized using a thermodynamic argument below.

5.7 TRANSITION IN EVACUATION DYNAMICS

The crossover in slopes (Figure 5-6B) of rate constants is intriguing as it points towards a transition in the evacuation mechanism. The significance of the transition point with respect to substrate wettability can be related to the corresponding adhesion energies

for the system using the Young [88] and Dupré [89] equations and available experimental values.

The Dupré equation for two continuum media (*Sub1* and *Sub2*) interacting in a third medium (say underwater) can be written as Eq. 4.1.

$$(W_{Sub1-Sub2})_{Water} = \gamma_{Sub1-Water} + \gamma_{Sub2-Water} - \gamma_{Sub1-Sub2} \quad (4.1)$$

where $(W_{Sub1-Sub2})_{Water}$ is the thermodynamic work of adhesion under water and γ's are interfacial energies between *Sub1*, *Sub2* and *water*. Subtracting from Eq.4.1 the Dupré expression for *Sub1-Sub2* in air (third medium), and substituting the difference in interfacial energies under water and in the dry case for *Sub1* and *Sub2* in terms of water contact angles ($(\theta_{Sub1-water})_{air}$ and $(\theta_{Sub2-water})_{air}$) and water interfacial energy (γ_{Water}) using the Young's equation we get, Eq.4.2.

$$(W_{Sub1-Sub2})_{Water} = (W_{Sub1-Sub2})_{air} - \gamma_{Water}[cos(\theta_{Sub1-water})_{air} + cos(\theta_{Sub2-water})_{air}] \quad (4.2)$$

For this study, *Sub1* is the hard substrate (*Sub*) and *Sub2* is PDMS. Plugging in the interfacial energy for the water-air interface (72.8 mJ/m^2) and the contact angle (110°) of water on PDMS in Eq. 4.2, we get Eq. 4.3.

$$(W_{Sub-PDMS})_{Water} = (W_{Sub-PDMS})_{Air} - \gamma_{Water} * Cos\theta_{Sub-Water} + 25 \quad (4.3)$$

If the observed transition point (~42°) represents the point where $(W_{Sub-PDMS})_{Water}$ is equal to zero, we estimate the $(W_{Sub-PDMS})_{Air}$ to be equal to 29 mJ/m^2. The estimated dry work of adhesion for ~42° water contact angle is in agreement with the experimental value (30 ± 3 mJ/m^2) measured during the loading cycle using the JKR method. The change in slope where the underwater thermodynamic work of

adhesion is zero suggests that formation of dry contacts or barriers in water flow path is responsible for slowing down the evacuation rates, as seen in Figure 5-3D and Fig. 4-6. Connected barriers in the flow path presents the argument of sealing mechanism or water entrapment in smaller puddles.

We highlight that the observed point (~42°) of transition in dynamics should not be considered as special number. The transition point depends upon the thermodynamics of the three phases. Any change in the surface energy of the elastomer or selected liquid will shift the transition point to either the lower or the higher side. The open question is to synthesize the elastomers with varying surface energies and hence design a universal evacuation curve. Further, modelling the dynamics about the transition point requires a broad consideration of parameter space which is yet to be discovered, especially, the influence of roughness seeks our attention and will thrive the field of underwater contact mechanics.

5.8 CONTACT FORMATION AND SUBSEQUENT EVACUATION

Uniting our observed trend with the established knowledge of thermodynamics and material deformation allows us to explain the contact formation in terms of two sequential processes. First, for all the cases presented in Figure 5-9, the PDMS lenses undergo elastohydrodynamic deformation due to liquid viscous forces which results in entrapment of water (confirmed from the height maps before contact, Figure 5-10). The contact region has water trapped in the center as a bell shape cavity with contact initiating at the periphery. The shape of this initial cavity is generic (also observed for much stiffer, glassy solids and more viscous fluids), though its scale depends simply on competition

between respective factors of solid and liquid response: lens curvature and modulus vs. collision speed and liquid viscosity [84]. The second process differs depending on the surface energy of the substrate. For the case of PDMS/glass contact, the water evacuates rapidly and smoothly through a thin film of water reducing its height with time. In the case of PDMS/OTS-*t*-glass contact, the puddle quickly and asymmetrically breaks into smaller puddles, which drain over a much longer period, limited by a tighter seal of the adhesive contact at the periphery. The possibility that absorption of a portion of the entrapped water into the PDMS lenses plays a parallel role with lateral drainage is not apparent in the data and would not explain the transition in the rates with surface chemistry, as the same lenses are used in all experiments and the only variable is the surface chemistry of the glass.

Now, we discuss the similarities in the water evacuation dynamics for a model system (PDMS lens/hard contact) with a complex reality (human thumb/hard contact). The water evacuation dynamics for both thumb/glass and thumb/OTS-*t*-glass contact is identical till ~ 7 sec (Figure 5-12B) and can be ascribed to the presence of valleys which facilitate the drainage (Figure 5-12A). We observe striking differences between the dynamics of thumb/glass and thumb/OTS-*t*-glass contact after ~ 7 sec that can be explained with our knowledge of the evacuation process for the model systems. The cleaned surface of stratum corneum is known to be highly hydrophobic (contact angle of $125^{\circ} - 130^{\circ}$) [90] due to which the thumb/OTS-*t*-glass interface should behave in a similar fashion as the PDMS lens/OTS-*t*-glass interface at microscopic scale. For initial region (till ~ 7 sec) the elastic modulus is high enough such that the adhesive forces have no effect on the dynamics. Subsequently, we observe sudden asymmetric break down of

the valleys (Figure 5-12B, bottom panel) for the case of thumb/OTS-*t*-glass interface which results in localized water entrapments. The instabilities in the valleys for thumb/OTS-*t*-glass contact seem similar to the breakdown of a large puddle into multiple smaller puddles for the case of PDMS lens/OTS-*t*-glass contact. Additionally, we observe asymptotic volumes for both thumb/glass and thumb/OTS-*t*-glass contact. This volume represents static condition in the observation timescale wherein the elastic stiffness of the ridges in the fingerprint support cavities of water in the valleys between. The previously reported drop in stiffness of the stratum corneum of a human finger with hydration/moisturization is likely changing this elastically supported volume as the contact evolves. The larger value of static volume of trapped water associated with thumb/OTS-*t*-glass contact is consistent with the notion that sealed puddles of incompressible water are contributing to the resistance of the fingerprint ridges to further collapse.

Here, we would like to point out that for the hydrophobic-hydrophobic (PDMS lens/OTS-*t*-glass) contact formation under water, we have made new observations which are discussed below.

5.9 WATER PUDDLE BREAKS DOWN BEFORE CONTACT

The instability in the deformation of a single puddle for the case of the PDMS lens approaching OTS-*t*-glass before any direct contact (Figure 5-9C and Figure 5-10B) points toward the presence of long-range hydrophobic forces, popularly known as solvation forces. When two hydrophobic surfaces approach each other underwater, a water-vapor cavity formation takes place that applies negative Laplace pressure on both

the surfaces resulting in the observed attraction between them [91]. The cavity formed is a transient state which is lower in energy than the two hydrophobic surfaces separated by some water layer but is still higher in energy when compared to the final thermodynamic equilibrium state of direct solid contact [91]. These hydrophobic solvation forces cannot be accounted for by the Derjaguin-Landau-Verwey-Overbeek (DLVO) or Lifshitz theory and have now been proven to exist, experimentally as well as through simulations and theory. Using surface force apparatus, it has been shown that these forces start to show up at separations of 20-100 nm (depending upon the hydrophobicity) for two rigid hydrophobic surfaces underwater [91].

We also observe that during instability only a part of periphery touches the substrate (Figure 5-10B). We speculate that as the water evacuation rates are high initially due to the high stored elastic energy, hence hydrostatic pressure, the peripheral edge opposite to the edge in contact is found to stay out of contact for some time to facilitate water evacuation. After a certain time, the entire peripheral area is found to seal with the smaller water puddles trapped in between. The evacuation mechanism for these smaller puddles following the sealing is unobservable and has been hypothesized below.

5.10 HOW IS WATER ESCAPING FROM SEALED ADHESIVE ENTRAPMENT

The water evacuation from the smaller puddles entrapped between the PDMS lens and OTS-*t*-glass (Figure 5-9C) can happen in multiple ways. PDMS elastomer, despite its negligible absorption of water (~40 mol/m^3), is known to allow some diffusion through its bulk in response to concentration gradients inside and across its surfaces [92]. In our case, presoaking the PDMS lens for ~6 hr prior to data collection and conducting

measurements underwater were found to eliminate its effect, as no differences in the decay constant (K) were observed upon increasing the presoaking time or across successive collisions in subsequent hours of the experiment. Further, the difference in the rate constants for evacuation (K values reported in Figure 5-6) for the glass substrate with 88° and 108° contact angle does not support the diffusion argument as both the substrates make adhesive contact with PDMS underwater and the K values should be similar if the mode of evacuation is diffusion through the PDMS material. Lastly, it is possible that the water is evacuating out along the interface through gaps smaller than the measurable length scale. It is well known that even though all the glass surfaces used are optically smooth, these surfaces are rough at nm length scale. The roughness at smaller length scales can remain as an interconnected channel facilitating the water evacuation along the interface. Further, the final equilibrium state can have majorly dry regions with water sealed at small scale roughness. The effect of surface roughness on water evacuation is difficult to investigate using the FTIR technique as the rougher surfaces will contribute to the light scattering and make the data analysis impractical. On the other hand, making rough or patterned PDMS structures is feasible and will be the scope of our future studies.

5.11 CONCLUSION

Competition between adhesive forces and fluid drainage can play a crucial role in collisions between deformable objects. While adhesion energetically favors contact between hydrophobic contacting pairs, that very affinity dynamically leads to entrapment of isolated puddles, thus delaying their ultimate contact. The paradoxical relationship

between kinetics and thermodynamics may explain why underwater adhesive designs which rely on surface hydrophobicity alone do not produce the best performance. Patterned or special morphology is necessary to increase evacuation rates.

We have demonstrated that increasing adhesive interaction between soft bodies leads to as many as 3 orders of magnitude in dynamics inhibition of their contact formation due to tighter sealing of trapped water, in a controlled system with simple geometry. In the complex practically important system – human thumb contact underwater – we found that competition between the same physical drivers plus surface texture led to a logically consistent, non-trivial result: the surface texture facilitates the initial drainage till the point where the adhesive forces overcome the elastic response of the thumb, that prevents longer-term approach to more fully intimate contact due to better sealing of puddles trapped between the adhesive contact.

Achieving conformality in wet/underwater environment is an inevitable requirement for most of the tissue adhesives and hemostatic sealants. The rapid yet robust performance of any bio-adhesive confronts the challenge of water removal [93,94]. Further, evolution of underwater contact area is important as it determines the creation of friction which is essential in everyday life. It would have been impossible to even hold a wet glass of water without any intimate contact. Though the increase in real contact area at microscopic level to high tangential frictional force in dry haptics has been well studied, the augmentation of human tactile sensing underwater is challenging as the primary factors include the length scale and time scale of contact [95]. Quantifying the area growth laws and exploring the wet haptics will be the scope of our future studies. Additionally, the

fundamental insights stemming from this study will act as critical design parameters and further development of the field of tissue adhesives.

CHAPTER VI

CONCLUSION AND FUTURE WORK

In this thesis, we have demonstrated the basic theory of frustrated total internal reflection and showed couple of examples of how other people use this technique to study contact dynamics between two surfaces such as pressure distribution underneath gecko foot, real contact area between footwear and glass floor, and why pens have rubbery grips. Furthermore, some researchers tried to use this technique to quantitatively study the contact dynamics between two surfaces by using simple exponential decay function of evanescent wave, but in recent years other people have approved that simple exponential decay function assumes all energy transmitted into third medium is gone that neglects multiple reflection and refraction is underestimating the real distance between two surfaces (Chapter 3) and having huge impact on understanding friction and adhesion behaviors. Significant efforts have been made by us to follow Fresnel equation (Eq.4.7) to correctly quantify frustrated total internal reflection apparatus. In Chapter 3, step by step procedure of building right angle prism based FTIR setup, incident angle calculations, data acquisition and image processing of converting reflectance to nanoscale gap thickness have been shown. Moreover, gap thicknesses between glass convex lens placed on flat prism have been measured and compared with Hertzian contact theory of elastic sphere contacting with half space to verify our assumption. Excellent agreement

with Hertzian contact theory was obtained, we then explored the capability of this technique to measure the thickness and surface topography of thin polymer films and compared it with ellipsometry.

In chapter 5, we utilized FTIR technique to study underwater contact formation between soft PDMS lens and hard smooth prism surface. Interestingly, we found a counterintuitive result. Thermodynamics tells us to expect underwater contact between two hydrophobic surfaces to result in stronger adhesion compared to two hydrophilic surfaces. However, presence of water changes not only energetics, but also the dynamic process of reaching a final state, which couples solid deformation and liquid evacuation. These dynamics can create challenges for achieving strong underwater adhesion/friction. Closer investigation, requiring sufficiently precise resolution of film evacuation while simultaneously controlling surface wettability has been lacking. I perform high resolution in-situ frustrated total internal reflection imaging to track underwater contact evolution between soft-elastic hemispheres of varying stiffness and smooth-hard surfaces of varying wettability. Surprisingly, I find exponential rate of water evacuation from hydrophobic-hydrophobic (adhesive) contacts is three orders of magnitude lower than that from hydrophobic-hydrophilic (non-adhesive) contacts. The trend of decreasing rate with decreasing wettability of glass sharply changes about a point where thermodynamic adhesion crosses zero, suggesting a transition in mode of evacuation, which is illuminated by 3-dimensional spatiotemporal heightmaps. Adhesive contact is characterized by the early localization of sealed puddles, whereas non-adhesive contact remains smooth, with film-wise evacuation from one central puddle. Measurements with a human thumb and alternatively hydrophobic/hydrophilic glass surface demonstrate practical consequences of

the same dynamics: adhesive interactions cause instability in valleys and lead to a state of more trapped water and less intimate solid-solid contact. These findings offer a new interpretation of patterned textures seen in underwater biolocomotive adaptations and insight toward technological implementation.

Most importantly, couple of research have reported that when they are using FTIR to measure the gap thicknesses between convex lens and prism surface, they detected 25nm offset in gap thickness measurement. Which means measured thickness is around 25nm greater than theoretical thickness. But this can be solved by simply shift experimental data down, and it will match theoretical data very well. We did encounter the same issue too.

The first experiment we did is changing the material of the second medium, for example change air to water, then gradually added glycerol into water solution to increase the refractive index of it (refractive indices shown in Table 6.1). With changing of the second medium the change of look-up table is shown in Figure 6-1. We found that offset increases with increasing of refractive index of the second medium, further investigation showed that RGB values of area that in actual contact don't change. However, as shown in Figure 6-1, at real contact area, the intensity value or in other word the RGB value should be 0 while right now it's not 0 but a constant value that across all cases. This means there is source of intensity that contribute to the offset. Suggestions from other research indicated that could be caused by scattering from surface roughness, surface contamination, background light, dusts on the surface, change of polarization of light due to interactions with materials and non-linear sensitivity of camera sensor. We are going to discuss these possibilities one by one.

6.1 ISSUES WITH CAMERA SENSOR

One possibility is that the camera sensor may not recognize complete dark (zero intensity) correctly. In other words, when there is no intensity, the sensor still reflects non-zero RGB value. To verify that, we did experiment by closing the shutter of camera. At this circumstance, no light can go into sensor and the RGB value is zero. This means our camera can recognize complete dark correctly, and it's not cause of offset.

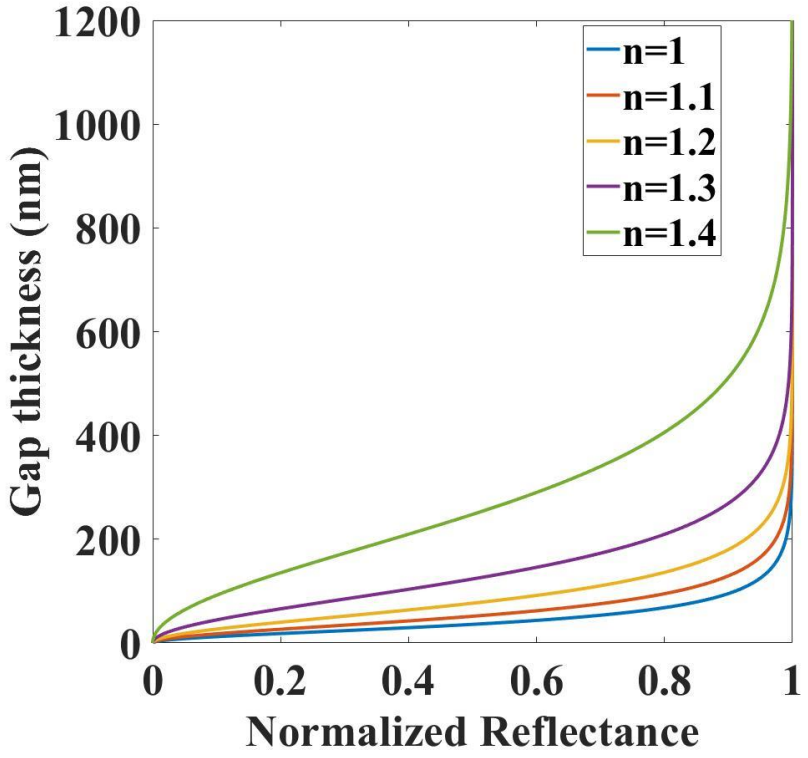

Figure 6-1: Look up table changes with changing of second medium.

6.2 EFFECT OF BACKGROUND LIGHT

As we already know that there is no issue with camera sensor and the offset seems comes from constant extra source of light, one may think it could come from background

light. To verify that two experiments were performed, the first one is turning off our light source, such that only background light can go into sensor, however, we didn't detect any intensity at this point, the intensity value showed is zero. The second experiment was performing Hertz contact experiment in dark room, no changes were detected, the offset is still there.

6.3 EFFECT OF POLARIZATION CHANGE

It is well known that when light interacts with materials the polarization of light could be changed. In our setup light must go through couple of mirrors and one prism before it goes into sensor, thus there is chance that polarization of light could be changed during light path. To make sure polarization of light goes into sensor remains same as it comes out from LED, an additional polarizer is placed right in front of the camera lens. By performing the Hertz contact experiment, the offset is still there. This didn't solve the problem at all.

6.4 EFFECT OF SURFACE CONTAMINATION AND ROUGHNESS

It is very hard to quantitatively study the effects of surface contamination and surface roughness. But any roughness or tiny particles on the surface could trigger scattering of light that could be received by camera and counted as extra source of light. Note that this effect is not limited to surface of prism but on all surfaces during the light path, for example, surface of mirror and surface of camera lens. Overall, the extra source of light or so-called offset in this thesis is likely caused by scattering of surfaces in the light path.

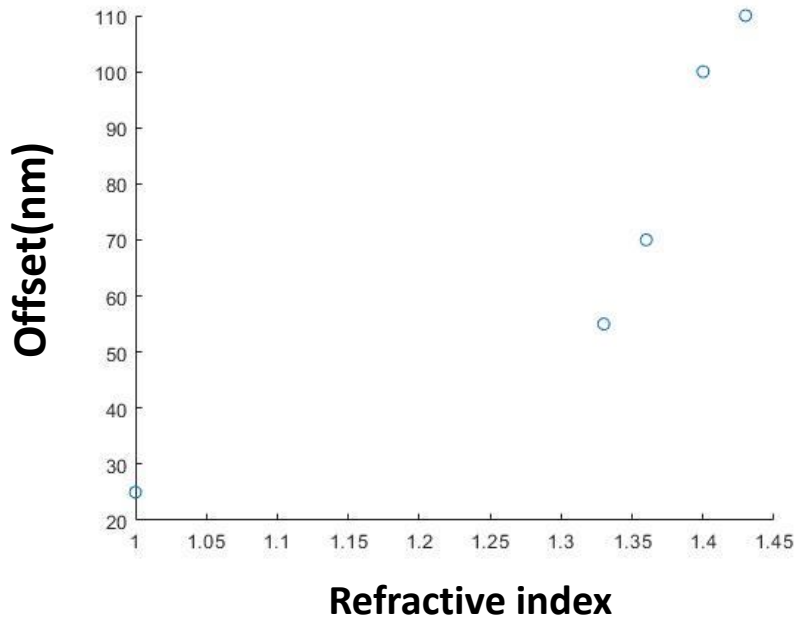

Figure 6-2: Offset change verse refractive indices. Offset increases increase with increasing of refractive index.

6.5 CONCLUSION

After above discussion, we think this offset is caused by scattering of light. Same as other techniques, FTIR needs to be calibrated every time before use to find this offset.

People who want to utilize this technique should aware this issue and avoid it. Or even identify the root cause of this problem.

REFERENCES

1. Narinder Kumar (2008). Comprehensive Physics XII. Laxmi Publications. p. 1416. ISBN 978-81-7008-592-8.
2. Shipman, James; Wilson, Jerry D.; Higgins, Charles A. (2015). An Introduction to Physical Science, 14th Ed. Cengage Learning. p. 187.
3. Muncaster, Roger (1993). A-level Physics. Nelson Thornes. pp. 465–467. ISBN 0-7487-1584-3.
4. Singh, Devraj (2015). Fundamentals of Optics, 2nd Ed. PHI Learning Pvt. Ltd. p. 453. ISBN 978-8120351462.
5. Avadhanulu, M. N. (1992). A Textbook of Engineering Physics. S. Chand Publishing. pp. 198–199. ISBN 8121908175.
6. Desmarais, Louis (1997). Applied Electro Optics. Pearson Education. pp. 162–163. ISBN 0-13-244182-9.
7. Wolf, Mark J. P. (2008). The Video Game Explosion: A History from PONG to Playstation and Beyond. ABC-CLIO. p. 315.
8. Johnsen, Sönke (2012). The Optics of Life: A Biologist's Guide to Light in Nature. Princeton Univ. Press. pp. 207–208. ISBN 978-0691139913.
9. Basu, Dipak (2000). Dictionary of Pure and Applied Physics. CRC Press. pp. 142–143. ISBN 1420050222
10. Gåsvik, Kjell J. (2003). Optical Metrology (3rd ed.). John Wiley and Sons. pp. 219–221. ISBN 0470846704.
11. Negara, Christian. (2015). Thickness Measurement of Thin Films on Curved Surfaces with Ellipsometry.
12. Hecht, Eugene (2017). Optics (5th Global ed.). Pearson. pp. 135–137. ISBN 978-1-292-09693-3.
13. Taitt, Chris Rowe, George P. Anderson, and Frances S. Ligler. "Evanescent wave fluorescence biosensors." Biosensors and Bioelectronics 20.12 (2005): 2470-2487.
14. Povinelli, Michelle L., et al. "Evanescent-wave bonding between optical waveguides." Optics letters 30.22 (2005): 3042-3044.

15. Milosevic, Milan. "On the nature of the evanescent wave." Applied spectroscopy 67.2 (2013): 126-131.

16. Fish, Kenneth N. "Total internal reflection fluorescence (TIRF)microscopy." Current protocols in cytometry 50.1 (2009): 12-18.

17. Holden, Seamus J., et al. "Defining the limits of single-molecule FRET resolution in TIRF microscopy." Biophysical journal 99.9 (2010): 3102-3111.

18. Poulter, Natalie S., et al. "The physical basis of total internal reflection fluorescence (TIRF) microscopy and its cellular applications." Advanced Fluorescence Microscopy (2015): 1-23.

19. Reichert, W. M., and G. A. Truskey. "Total internal reflection fluorescence (TIRF) microscopy. I. Modelling cell contact region fluorescence." Journal of cell science 96.2 (1990): 219-230.

20. Sun, Mengyue, et al. "Attractive forces slow contact formation between deformable bodies underwater." Proceedings of the National Academy of Sciences 118.41 (2021): e2104975118.

21. A. Rahman, I. Ali, S. M. Al Zahrani, R. H. Eleithy, A review of the applications of nanocarbon polymer composites. Nano. 6, 185-203 (2011)

22. Ling, Zichen, Cheng Zhang, and Qixin Zhou. "Synthesis and characterization of 1 K waterborne non-isocyanate polyurethane epoxy hybrid coating." Progress in Organic Coatings 169 (2022): 106915.1

23. Zhou, Ying, et al. "Graphene Oxide-Hybridized Waterborne Epoxy Coating for Simultaneous Anticorrosive and Antibiofilm Functions." Frontiers in Materials (2022): 428.1

24. Zhang, Jibiao, et al. "Degradation Behaviors of Two Epoxy Coatings After Dry/Wet-Accelerated Fog Exposure of Different Solutions." Frontiers in Materials (2021): 554.1

25. Zhang, Cheng, et al. "Anti-corrosion non-isocyanate polyurethane polysiloxane organic/inorganic hybrid coatings." Progress in Organic Coatings 148 (2020): 105855.1

26. Wang, Haoran, et al. "Improvement of corrosion resistance and solid content of zinc phosphate pigmented alkyd coating by methacrylated cardanol." Materials Today Communications 24 (2020): 101139.1

27. Zhang, Cheng, Haoran Wang, and Qixin Zhou. "Waterborne isocyanate-free polyurethane epoxy hybrid coatings synthesized from sustainable fatty acid diamine." Green Chemistry 22.4 (2020): 1329-1337.

28. Wang, H., Zhang, C., Zeng, W., & Zhou, Q. (2019). Making alkyd greener: Modified cardanol as bio-based reactive diluents for alkyd coating. Progress in Organic Coatings, 135, 281-290.

29. Zhang, C., Wang, H., Zeng, W., & Zhou, Q. (2019). High biobased carbon content polyurethane dispersions synthesized from fatty acid-based isocyanate. Industrial & Engineering Chemistry Research, 58(13), 5195-5201.

30. Zhang, C., Wang, H., & Zhou, Q. (2018). Preparation and characterization of microcapsules based self-healing coatings containing epoxy ester as healing agent. Progress in organic coatings, 125, 403-410.

31. King, Hunter, et al. "Elastic sheet on a liquid drop reveals wrinkling and crumpling as distinct symmetry-breaking instabilities." Proceedings of the National Academy of Sciences 109.25 (2012): 9716-9720.

32. Zhang, Chao, et al. "Thickness Limit for Alignment of Block Copolymer Films Using Solvent Vapor Annealing with Shear." Macromolecules 51.11 (2018): 4213-4219.

33. P. Sanjiv Kasbe, N. Kumar, G. Manik, A molecular simulation analysis of influence of lignosulphonate addition on properties of modified 2-ethyl hexyl acrylate/methyl methacrylate/acrylic acid based pressure sensitive adhesive. International Journal of Adhesion and Adhesives. 78, 45-54 (2017).

34. Liu, Jessica A-C., et al. "Photothermally and magnetically controlled reconfiguration of polymer composites for soft robotics." Science advances 5.8 (2019): eaaw2897.

35. M. E. Schrader, Young-dupre revisited. Langmuir. 11, 3585-3589 (1995).

36. K. L. Johnson, K. Kendall, a. Roberts, Surface energy and the contact of elastic solids. Proceedings of the royal society of London. A. mathematical and physical sciences. 324, 301-313 (1971).

37. K. Kendall, Adhesion: molecules and mechanics. Science. 263, 1720-1725 (1994).

38. A. Narayanan, S. Kaur, N. Kumar, M. Tsige, A. Joy, A. Dhinojwala, Cooperative Multivalent Weak and Strong Interfacial Interactions Enhance the Adhesion of Mussel-Inspired Adhesives. Macromolecules. 54, 5417-5428 (2021).

39. N. Maeda, N. Chen, M. Tirrell, J. N. Israelachvili, Adhesion and friction mechanisms of polymer-on-polymer surfaces. Science. 297, 379-382 (2002).

40. J. N. Israelachvili Intermolecular and surface forces (Academic press) (2011).

41. Shi, Z.; et al. (2018). "Dynamic contact angle hysteresis in liquid bridges". Colloids and Surfaces A: Physicochemical and Engineering Aspects. **555**: 365–371. arXiv:1712.04703.

42. W. A. Zisman, Relation of the Equilibrium Contact Angle to Liquid and Solid Constitution. In: Advances in Chemistry 43 (1964), P. 1-51.

43. Ebnesajjad, Sina, and Arthur H. Landrock. Adhesives technology handbook. William Andrew, 2014.

44. Y. Kitazaki, and T. Hate, J. Adhesion 4, 123 (1972).

45. Wenzel, R. N. Ind. Eng. Chem. 1936, 28, 988–994.

46. Cassie, A. B. D.; Baxter, S. Trans. Faraday Soc. 1944, 40, 546.

47. Murakami, Daiki, Hiroshi Jinnai, and Atsushi Takahara. "Wetting transition from the Cassie–Baxter state to the Wenzel state on textured polymer surfaces." Langmuir 30.8 (2014): 2061-2067.

48. B. N. J. Persson, Contact mechanics for randomly rough surfaces. Surface science reports. 61, 201-227 (2006).

49. Tabor, D., 1977, Surface forces and surface interactions, Journal of Colloid and Interface Science, 58(1), pp. 2-13.

50. Dzidek, Brygida, et al. "Why

51. pens have rubbery grips." Proceedings of the National Academy of Sciences 114.41 (2017): 10864-10869.

52. Needham, J. A., and James S. Sharp. "Watch your step! A frustrated total internal reflection approach to forensic footwear imaging." Scientific reports 6.1 (2016): 1-7.

53. Kolinski, John M., et al. "Skating on a film of air: drops impacting on a surface." Physical review letters 108.7 (2012): 074503.

54. Shirota, Minori, et al. "Measuring thin films using quantitative frustrated total internal reflection (FTIR)." The European Physical Journal E 40.5 (2017): 1-9.

55. A. P. Defante, A. Nyarko, S. Kaur, T. N. Burai, A. Dhinojwala, Interstitial Water Enhances Sliding Friction. Langmuir. 34, 4084-4094 (2018).

56. B. N. Persson, U. Tartaglino, O. Albohr, E. Tosatti, Rubber friction on wet and dry road surfaces: The sealing effect. PhRvB. 71, 035428 (2005).

57. P. Karnal, P. Roberts, S. Gryska, C. King, C. Barrios, J. Frechette, Importance of substrate functionality on the adhesion and debonding of a pressure-sensitive adhesive under water. ACS applied materials & interfaces. 9, 42344-42353 (2017).

58. G. P. Maier, M. V. Rapp, J. H. Waite, J. N. Israelachvili, A. Butler, Adaptive synergy between catechol and lysine promotes wet adhesion by surface salt displacement. Science. 349, 628-632 (2015).

59. S. Kaur, A. Narayanan, S. Dalvi, Q. Liu, A. Joy, A. Dhinojwala, Direct Observation of the Interplay of Catechol Binding and Polymer Hydrophobicity in a Mussel-Inspired Elastomeric Adhesive. ACS Central Science. 4, 1420-1429 (2018).

60. Z. A. Levine, M. V. Rapp, W. Wei, R. G. Mullen, C. Wu, G. H. Zerze, J. Mittal, J. H. Waite, J. N. Israelachvili, J.-E. Shea, Surface force measurements and

simulations of mussel-derived peptide adhesives on wet organic surfaces. Proceedings of the National Academy of Sciences. 113, 4332-4337 (2016).

61. S. Singla, G. Amarpuri, N. Dhopatkar, T. A. Blackledge, A. Dhinojwala, Hygroscopic compounds in spider aggregate glue remove interfacial water to maintain adhesion in humid conditions. Nature Communications. 9, 1890 (2018).

62. D. M. Drotlef, L. Stepien, M. Kappl, W. J. P. Barnes, H. J. Butt, A. del Campo, Insights into the adhesive mechanisms of tree frogs using artificial mimics. Advanced Functional Materials. 23, 1137-1146 (2013).

63. A. Y. Stark, T. W. Sullivan, P. H. Niewiarowski, The effect of surface water and wetting on gecko adhesion. The Journal of Experimental Biology. 215, 3080-3086 (2012).

64. P. Y. Hsu, L. Ge, X. Li, A. Y. Stark, C. Wesdemiotis, P. H. Niewiarowski, A. Dhinojwala, Direct evidence of phospholipids in gecko footprints and spatula–substrate contact interface detected using surface-sensitive spectroscopy. Journal of The Royal Society Interface. 9, 657-664 (2012).

65. A. Y. Stark, N. A. Wucinich, E. L. Paoloni, P. H. Niewiarowski, A. Dhinojwala, Self-Drying: A Gecko's Innate Ability to Remove Water from Wet Toe Pads. PLoS One. 9, e101885 (2014).

66. B. Persson, Wet adhesion with application to tree frog adhesive toe pads and tires. Journal of Physics: Condensed Matter. 19, 376110 (2007).

67. A. Roberts, Squeeze films between rubber and glass. Journal of Physics D: Applied Physics. 4, 423 (1971).

68. A. Roberts, D. Tabor, The extrusion of liquids between highly elastic solids. Proceedings of the Royal Society of London. A. Mathematical and Physical Sciences. 325, 323-345 (1971).

69. Y. Wang, J. Frechette, Morphology of soft and rough contact via fluid drainage. Soft Matter. 14, 7605-7614 (2018).

70. F. Eirich, D. Tabor (1948) Collisions through liquid films. MPCPS, (Cambridge University Press), pp 566-580.

71. H. Christensen, The oil film in a closing gap. Proceedings of the Royal Society of London. Series A. Mathematical and Physical Sciences. 266, 312-328 (1962).

72. O. Reynolds, IV. On the theory of lubrication and its application to Mr. Beauchamp tower’s experiments, including an experimental determination of the viscosity of olive oil. Philosophical Transactions of the Royal Society of London. 177, 157-234 (1886).

73. R. H. Davis, J.-M. Serayssol, E. Hinch, The elastohydrodynamic collision of two spheres. J. Fluid Mech. 163, 479-497 (1986).

74. S. Leroy, E. Charlaix, Hydrodynamic interactions for the measurement of thin film elastic properties. Journal of Fluid Mechanics. 674, 389 (2011).

75. R. Villey, E. Martinot, C. Cottin-Bizonne, M. Phaner-Goutorbe, L. Léger, F. Restagno, E. Charlaix, Effect of Surface Elasticity on the Rheology of Nanometric Liquids. Physical Review Letters. 111, 215701 (2013).

76. S. Leroy, A. Steinberger, C. Cottin-Bizonne, F. Restagno, L. Léger, É. Charlaix, Hydrodynamic Interaction between a Spherical Particle and an Elastic Surface: A Gentle Probe for Soft Thin Films. Physical Review Letters. 108, 264501 (2012).

77. Y. Wang, C. Dhong, J. Frechette, Out-of-Contact Elastohydrodynamic Deformation due to Lubrication Forces. Physical Review Letters. 115, 248302 (2015).

78. Y. Wang, M. R. Tan, J. Frechette, Elastic deformation of soft coatings due to lubrication forces. Soft Matter. 13, 6718-6729 (2017).

79. J. N. Lee, C. Park, G. M. Whitesides, Solvent compatibility of poly (dimethylsiloxane)-based microfluidic devices. Analytical chemistry. 75, 6544-6554 (2003).

80. K. Vorvolakos, M. K. Chaudhury, The effects of molecular weight and temperature on the kinetic friction of silicone rubbers. Langmuir. 19, 6778-6787 (2003).

81. A. P. Defante, A. Nyarko, S. Kaur, T. N. Burai, A. Dhinojwala, Interstitial Water Enhances Sliding Friction. Langmuir. 34, 4084-4094 (2018).

82. S. Dalvi, A. Gujrati, S. R. Khanal, L. Pastewka, A. Dhinojwala, T. D. Jacobs, Linking energy loss in soft adhesion to surface roughness. Proceedings of the National Academy of Sciences. 116, 25484-25490 (2019).

83. S. Perutz, E. Kramer, J. Baney, C. Y. Hui, C. Cohen, Investigation of adhesion hysteresis in poly (dimethylsiloxane) networks using the JKR technique. J. Polym. Sci., Part B: Polym. Phys. 36, 2129-2139 (1998).

84. Y. Wang, G. A. Pilkington, C. Dhong, J. Frechette, Elastic deformation during dynamic force measurements in viscous fluids. Current opinion in colloid & interface science. 27, 43-49 (2017).

85. M. Kanduč, R. R. Netz, From hydration repulsion to dry adhesion between asymmetric hydrophilic and hydrophobic surfaces. Proceedings of the National Academy of Sciences. 112, 12338-12343 (2015).

86. B. M. Dzidek, M. J. Adams, J. W. Andrews, Z. Zhang, S. A. Johnson, Contact mechanics of the human finger pad under compressive loads. Journal of The Royal Society Interface. 14, 20160935 (2017).

87. R. H. Wildnauer, J. W. Bothwell, A. B. Douglass, Stratum corneum biomechanical properties I. Influence of relative humidity on normal and extracted human stratum corneum. J. Invest. Dermatol. 56, (1971).

88. T. Young, III. An essay on the cohesion of fluids. Philos. Trans. R. Soc. London. 95, 65-87 (1805).

89. A. Dupré, P. Dupré Théorie mécanique de la chaleur (Gauthier-Villars) (1869

90. M. Ginn, C. Noyes, E. Jungermann, The contact angle of water on viable human skin. J. Colloid Interface Sci. 26, 146-151 (1968).

91. E. E. Meyer, K. J. Rosenberg, J. Israelachvili, Recent progress in understanding hydrophobic interactions. Proceedings of the National Academy of Sciences. 103, 15739-15746 (2006).

92. G. C. Randall, P. S. Doyle, Permeation-driven flow in poly (dimethylsiloxane) microfluidic devices. Proceedings of the National Academy of Sciences. 102, 10813-10818 (2005).

93. A. Mahdavi, L. Ferreira, C. Sundback, J. W. Nichol, E. P. Chan, D. J. Carter, C. J. Bettinger, S. Patanavanich, L. Chignozha, E. Ben-Joseph, A biodegradable and biocompatible gecko-inspired tissue adhesive. Proceedings of the National Academy of Sciences. 105, 2307-2312 (2008).

94. H. Yuk, C. E. Varela, C. S. Nabzdyk, X. Mao, R. F. Padera, E. T. Roche, X. Zhao, Dry double-sided tape for adhesion of wet tissues and devices. Nature. 575, 169-174 (2019).

95. M. Ayyildiz, M. Scaraggi, O. Sirin, C. Basdogan, B. N. Persson, Contact mechanics between the human finger and a touchscreen under electroadhesion. Proceedings of the National Academy of Sciences. 115, 12668-12673 (2018).